DEVELOPMENT OF INVERSION-BASED FEEDFORWARD-FEEDBACK CONTROL TECHNIQUES FOR ADVANCED MANUFACTURING

by

ZHIHUA WANG

A dissertation submitted to the

Graduate School-New Brunswick

Rutgers, The State University of New Jersey

In partial fulfillment of the requirements

For the degree of

Doctor of Philosophy

Graduate Program in

Mechanical and Aerospace Engineering

Written under the direction of

Prof. Qingze Zou

And approved by

_____

_____

_____

_____

_____

New Brunswick, New Jersey

OCTOBER, 2015

AbSTRACT OF THE DISSERTATION

Development of Inversion-Based Feedforward-Feedback Control Techniques for Advanced Manufacturing

by ZHIHUA WANG

Dissertation Director:

Prof. Qingze Zou

Advanced manufacturing aims to make high-quality products at low cost with high efficiency and highly integrated/controlled processes, thereby, promoting the process integration and providing accommodation of customized and cost-effective miniaturized products. With the increasing demands on product precision and cost efficiency in micro- and nano-scale manufacturing, the development and implementation of control technologies have become an indispensable part of advanced manufacturing. However, challenges exist in the process control of micro- and nano-scale manufacturing. The system dynamics, in general, is complicated and can be excited when the micro- and nano- manufacturing are conducted at high speeds, and other adverse effects including the hysteresis and creep effects of the actuators further complicates the precision control of the manufacturing system. Additional challenges also arise from the variation/uncertainty and environmental disturbances. It has been demonstrated that micromanufacturing could benefit from the augment of ultrasonic vibration in achieving lower power consumptions and elongated tool life. However, the fundamental mechanism of ultrasonic vibration effect on micromanufacturing has not yet been understood. Similar challenges also exist in probe-based nanomanufacturing as the patterning throughput is ultimately limited by the patterning speed, which, in turn, is limited by the vibrational dynamics and hysteresis effect, as well as the cross-axis dynamics coupling effect of the actuation system. Further challenge

arises when patterning directly on hard materials using probe-based approach — even with stiff probe of hardest material, the pattern obtained on hard sample such as tungsten is hardly of any practical usage (feature depth < 0.5 nm). These challenges in micro- and nano-manufacturing motivate the research in this dissertation.

In this dissertation, the dynamics and hysteresis effect are studied and addressed for the magnetostrictive actuator-based ultrasonic-vibration-assisted microforming process and probe-based nanofabrication with an atomic force microscope (AFM). In particular, a magnetostrictive actuator-based mechatronic system is developed for the ultrasonic-vibration-assisted microforming process. The modeling-free inversion-based iterative learning control method (MIIC) is utilized to compensate for the dynamics and hysteresis effect on the ultrasonic vibration generation across a large range of working frequency. The Fibonacci method is utilized to rapidly identify the resonant frequency online for more pronounced ultrasonic vibration effect. To address the backlash and relatively low resolution of the DC-motor, a bulk motion actuation system is designed and fabricated with a mechanical amplification around a magnetostrictive actuator. Such a design allows the bulk motion for large output force and motion stroke with high resolution (< 1 um). The entire microforming process is divided into pre-welding and welding phases. During the pre-welding phase, the data-driven, modeling-free differential-inversion-based iterative control (MFDIIC) approach is developed to address the dynamics and the hysteresis effect of the magnetostrictive actuator for high efficiency. The inversion-based optimal output tracking-transition method is employed to realize the accuracy transition from the pre-welding to the welding phase, and thus improves the product quality. In the study of the probe-based nanofabrication, the MFDIIC method is also utilized and integrated to address the adverse dynamics effect and the hysteresis behaviour of the piezoactuators. An ultrasonic vibration is also augmented in the driving of the piezoactuator in $z-$ axis to increase the impact of the probe and enables the patterning on hard materials.

The MFDIIC technique is further analyzed and theoretically proved of its efficiency in compensating for both of the dynamics and nonlinear hysteresis effects with no needs for modeling hysteresis and/or dynamics, and achieve both precision tracking and good robustness against hysteresis/dynamics changes. The convergence of the MFDIIC algorithm is analyzed with random output disturbance/noise considered. It is shown that precision tracking can be achieved

with the tracking error close to the noise level in the statistical sense.

ACKNOWLEDGEMENTS

First and foremost, I would like to thank my advisor Prof. Qingze Zou for the continuous support of my Ph.D. study and research. I appreciate his scientific guidance, encouragement, and insightful discussions and suggestions during the past six years. He is not only my mentor, but also a tremendously helpful friend. His patience, genuine caring and concern during my Ph.D. pursuit enabled me to attend to life while earning my degree. I'm also thankful for his invaluable career advice and suggestions. I couldn't have imagined having a better advisor and mentor for my Ph.D study.

I would like to thank Prof. LeAnn Faidley for being my co-adviser and supporting me during my study in Iowa State University. I would also like to thank the rest of my thesis committee: Prof. Gap-Yong Kim, Prof. Jingang Yi, and Prof. Aaron Mazzeo for their insightful comments and contribution to this work.

In regards to the microforming project, I am very grateful for Dr. Adam Witthauer setting up and monitoring the experiments, and bearing the ultrasound in the lab in Iowa State University when I remotely debugged the system from Rutgers University.

I also thank my friends and fellow labmates in Prof. Zou's group: Ying Wu, Zhonghua Xu, Haiming Wang, Juan Ren, Yan Zhang and Jiangbo Liu, for those stimulating discussions and all the fun we had in the past.

Finally, I would like to thank my parents, my brother, my wife, my son and my uncle for their endless love, support and care throughout my life.

Table of Contents

List of Tables

List of Figures

Chapter 1

Introduction

Advanced manufacturing emphasizes on cost efficiency and system miniaturization. Among the advanced manufacturing technologies, micromanufacturing and nanomanufacturing, as the fundamental technologies towards miniaturized products and manufacturing platforms, have played an important role in supplying miniaturized devices and components in the fields including medical, aerospace, military/defense, optics, automotive, consumer products, and microelectronics. Micromanufacturing has emerged as a critical avenue to bridge the manufacturing between nano- and macro-scale [1]. Many fields have been increasingly demanding miniature devices and components by micromanufacturing with complex micro-scale features made from a wide selection of materials [2, 3], and nanomanufacturing is by far predominant in semiconductor industry. However, there still exist many challenges because of the scaling down of the tools, process, and machinery in micro and nano-scale manufacturing. First, the dynamics of the micro/nano-scale manufacturing system from the miniaturized motors and the secondary mechanical structures is generally complicated, and can be excited at high speeds during the manufacturing process, which complicates the process control of the micro/nano-scale manufacturing. The hysteresis effect of the currently adopted actuators imposes more challenges on the control of the actuation system, and further hinders the throughput by these technologies. In this dissertation, the dynamics and control issues in micro-scale forming and nano-scale manufacturing is studied through the development of a suite of inversion-based feedforward-feedback of advanced control techniques.

In micromanufacturing, compared to other subcategories, such as micromilling and microturing, the fundamental mechanisms of microforming process are not well understood due to the inability of the miniaturized motors to simultaneously deliver the required large force (kN

magnitude), high bandwidth (up to kHz), and precise positioning accuracy (nanometer resolution). The current bulk motion actuators in microforming systems are generally bulky and not suitable for miniaturization. In literature, different actuators/motors have been implemented to achieve mm level motion stroke for micro-scale forming in industrial applications, such as DC/voice coil motors [4], piezoelectric actuators [5], and magnetostrictive actuators [6]. Though a large motion stroke (> 1 mm) could be easily achieved by DC/voice coil motors, the backlash/friction (DC motors) or the limited resolutions (voice coil motors, $\sim 1\ \mu$m) hampers its performance in ultraprecision machining applications. While the piezoelectric actuators and magnetostrictive actuators find applications in the fine/second stage design in dual-stage designs with high resolutions [7, 8], the small output displacement makes it unsuitable to directly generate bulk motions. We note that compound actuation systems configured in a coarse/fine dual stage served as methods to overcome the limitations of the actuators [4, 9]. However, the dynamics of the coarse stage actuator is slow and hinders its efficiency, and the coupled dynamics, especially when with large load, in such dual stage designs poses complexity in the motion control. On the other hand, it's noted that ultrasonic vibration applied in conventional large scale forming operation has shown to improve the part productivity and quality due to its softening effect on the workpiece [10]. The ultrasonic-induced enhancement results in significant reduction of the force applied and thus a substantial elongation of the tool life [11]. Furthermore, it has been proposed that the ultrasonic effect might become more pronounced if the vibration occurs at the resonant frequency of the workpiece [12]. However, the application of ultrasonic vibration for micro-scale forming operation has not been studied, and the fundamental mechanism is still not clear. There is a need for the development of a new type of actuating system optimized for the microforming system and appropriate control strategies.

In nanomanufacturing, the probe-based nanolithography (PBN) has drawn much attention recently. Among the PBN techniques, the nanopatterning through mechanical plowing not only costs less in both equipment and operation, but also has less complexity in the process control. Challenges, however, need to be addressed to achieve high-speed patterning on hard material using mechanical plowing. One of the main challenges is to maintain precision positioning of the cantilever probe with respect to the sample surface during the patterning process at high

speeds, particularly when the fabrication size becomes relatively large. Like in other PBN processes, the dynamics of the actuation system, from the piezoelectric actuators to the mechanical fixture (of the cantilever) and then to the cantilever, can be excited when the plowing is at high speeds, resulting in pattern distortions [13]. More pattern distortions can be induced when the fabrication size is increased towards the full displacement range of the piezoactuators, as the hysteresis effect of the piezo actuators becomes more pronounced [14, 15]. Moreover, cross-axis coupling exists in positioning between different axes during 3-D PBN process, due to the misalignment (albeit small) of the piezo actuators and/or positioning sensors [16, 15]. Further challenge in mechanical plowing arises when fabricating on hard material. As the hardness of material increases, however, it becomes increasingly difficult to pattern (indent) on those materials, even with the hardest probe available (diamond probe). This difficulty might be alleviated by repeatedly plowing the same pattern [16]. The pattern quality (line width and uniformity of line depth), however, can be degraded as it is very challenging to reposition the probe exactly along the same path (with nanometer to sub-nanometer precision), particularly when plowing at high-speed and/or large range. Moreover, such an approach becomes ineffective for ultra hard materials such as tungsten or chromium. Therefore, techniques need to be designed to maintain precision probe-sample positioning during the high-speed PBN process, and enable mechanical plowing for high-speed, large-range patterning on hard materials.

In this work, we propose to utilize a Terfenol-D centered mechanical design to achieve the mm level motion range with high resolution and sufficient load capability for microforming process. The high energy density of magnetostrictive materials makes it highly possible to trade off the blocked force against larger output displacement by utilizing appropriate mechanical design, which makes full use of the high resolution and output force of the magnetostrictive actuators. It is challenging, however, to achieve the high-speed and precision positioning for the micro-scale forming operations. The dynamics of the actuation system, from the magnetostrictive transducer to the mechanical flexures, can be exited during the high-speed motions. The dynamics also changes when the system is loaded. Moreover, the intrinsic nonlinear hysteresis effect of the magnetostrictive actuator is prominent since it is designed to exploit the full range of its displacement capacity. During the microforming process, the ultrasonic vibration was

augmented to bulk motion and leads to the workpiece welding. The phase change of the workpiece induces the drop of the interaction force between the actuator and the workpiece. Without regulation of the actuation force, the welded workpiece could be easily deformed, which, in turn, could also damage the tools. In this dissertation, a feedforward-feedback control framework is developed by combining the recently-devloped iterative control technique [17] and the Kalman filtering. Such a design not only compensates for the dynamics and hysteresis effect of the actuator, but also realizes the accurate phase transition of the workpiece, and thereby achieves the high-speed and quality microforming.

The nanolithography using an atomic force microscope (AFM) is also investigated in this dissertation. An approach integrating advanced control with ultrasonic-vibration of the probe is presented to enable the mechanical plowing for high-speed patterning on hard materials. The normal ultrasonic-vibration of the probe substantially increases the impact (from the probe) on the sample surface, thereby enabling indentation (plowing) on hard material. A data-driven, differential-inversion iterative control (MFDIIC) algorithm is proposed to account for both the hysteresis and the vibrational dynamics effects during the high-speed, large range PBN process. The MFDIIC is also utilized to compensate for the cross-axis dynamics coupling in multi-axis fabrication process. Both the patterning speed and feature quality are significantly improved by this combination of advanced control technique and ultrasonic vibration augmented to the AFM probe motion.

The rest of this dissertation is organized as follows.

In chapter 2, a mechatronic system based on a magnetostrictive actuator is developed for microforming process. Magnetostrictive actuators are very promising to address existing challenges in microforming technology. Compared to other actuators such as miniaturized motors and piezoactuators, magnetostrictive actuators have advantages including large actuation frequency range, low input voltage, and high force density [18]-[21]. Although these advantages of magnetostrictive actuators have been explored in other precision-positioning applications [22]-[24], no work has been done to utilize them for ultrasonic-vibration-assisted microforming processes. It is also challenging to rapidly and accurately identify the resonance of the system, and maintain the resonant frequency during the microforming process. Such challenges arise due to the distortion of the ultrasonic vibration amplitude by the dynamics and intrinsic

hysteresis behavior of the magnetostrictive actuation system, and the variation in the material properties of the workpiece itself. To address these above issues, the modeling-free inversion-based iterative learning approach [25] is utilized to compensate for the dynamics effect of the magnetostrictive actuation system on the ultrasonic vibration generation. Then the Fibonacci search method [26] is utilized to achieve rapid identification of the resonant frequency on-line. The developed system serves as a platform for investigating the mechanisms behind the ultrasonic-vibration-assisted microforming process.

In chapter 3, a dual-stage microforming system is constructed based on magnetostrictive actuators to achieve both precision bulk motion and ultrasonic vibration generation. The data-driven, modeling-free differential-inversion-based iterative control (MFDIIC) approach is employed to account for the adverse effects during the pre-welding phase in the microforming process, including the vibrational dynamics, the hysteresis behavior of the magnetostrictive actuator, and the dynamics variation of the bulk motion subsystem. In order to handle the phase transition of the workpieces during the microforming, the optimal output tracking-transition method [27] is utilized to attain the smooth and efficient phase transition during the microforming process. This method is advantageous in eliminating the post-transition oscillation by finding the control input that matches the boundary state values at the beginning and the end of the transition period, based on the previewed stable-inversion approach [28]. Compared to the minimization of the input energy in the optimal output transition technique [29], the minimization of the output energy is more desirable as it tends to provide more smooth and smaller displacement output during the transition. Thus, better microforming quality could be achieved by the smaller displacement output during the switching from the pre-welding to the welding phase. The proposed control framework is illustrated by implementing it in the welding of two ABS plastic workpieces. The efficacy of the proposed approach is demonstrated through the experimental control results and the welded workpieces, in which the optimal high-speed microforming and substantial welding quality are achieved.

In chapter 4, we present an approach that integrates advanced control with ultrasonic-vibration of the probe to enable mechanical plowing for high-speed patterning on hard materials. The MFDIIC algorithm is utilized to account for both the hysteresis and the vibrational

dynamics effects during the high-speed, large range PBN process. The MFDIIC is also utilized to compensate for the cross-axis dynamics coupling in multi-axis fabrication process. Moreover, ultrasonic vibration of the probe in the normal (vertical) direction is augmented to the motion of the probe during the plowing process [30]. The normal ultrasonic-vibration of the probe substantially increases the impact (from the probe) on the sample surface, thereby enabling indentation (plowing) on hard material. The proposed approach is implemented to fabricate patterns of large size (60 um) on a tungsten coated mask (with quartz as the substrate). The experimental results showed that a plowing speed as high as ~5 mm/sec can be achieved with the patterned line width and line depth at 95 nm and 2 nm, respectively.

In chapter 5, the data-driven, modeling-free differential-inversion-based iterative control (MFDIIC) approach is developed to achieve simultaneous hysteresis and vibrational dynamics compensation without modeling the hysteresis and/or the vibrational dynamics. Furthermore, the convergence of the MFDIIC in compensating for the hysteresis effect is analyzed by considering the system a hammerstein system in the frequency domain. The output tracking error can be quantified in a statistical sense by the properties of the random output disturbance/noise considered in the analysis. The theoretical analysis shows the output tracking error by the MFDIIC methodis also validated through experimental results with the magnetostrictive actuator and piezoactuator to demonstrate the competence of the proposed MFDIIC method in compensating for both the system dynamics and hysteresis effect simultaneously.

In Chapter 6, this dissertation is concluded.

Chapter 2

Dynamics Compensation and Rapid Resonance Identification In Ultrasonic-Vibration-Assisted Microforming System Using Magnetostrictive Actuator

Abstract

In this chapter, a mechatronic system is developed to compensate for the hardware dynamics effect and to achieve rapid resonance identification for an ultrasonic-vibration-assisted microforming system. Microforming has recently attracted great interests due to the need for miniaturized manufacturing systems in emerging applications. It has been demonstrated that significant benefits such as, reduction of input energy and prolongation of tool life, can be gained by introducing ultrasonic vibration into the microforming process, particularly when the vibration is maintained at the resonant frequency of the vibrating workpiece. However, the fundamental mechanism of ultrasonic vibration effect on the microforming process has not yet been understood; the electrical actuators currently used to generate the ultrasonic vibration are bulky and not suitable for miniaturization of the microforming system; and control of ultrasonic vibration is primitive and far from being optimal. To tackle these challenges, a microforming platform based on a magnetostrictive actuator has been developed. The main contributions of this chapter are two fold: (1) the use of a novel iterative learning control technique along with a vibration oscillation regulation circuit to compensate for the effect of the magnetostrictive actuator dynamics on the ultrasonic vibration generation, and thereby, maintain the same vibration amplitude across a large excitation frequency range, and (2) the use of the Fibonacci search algorithm to achieve rapid online identification of the resonant frequency. Experimental results obtained on the developed magnetostrictive-actuator-based microforming system are presented and discussed to demonstrate the efficacy of the proposed approach.

2.1 Introduction

A mechatronic system is developed to control the magnetostrictive actuation system for the ultrasonic-vibration-assisted microfroming process. Micromanufacturing technology, including microforming [2], microjoining [31], and micropunching [32], has emerged as a critical avenue to bridge the manufacturing between nano- and macro-scale [1]. Work is needed to address issues related to the fundamental manufacturing mechanisms involved and the development of the manufacturing system itself. Specifically, to investigate the impact of ultrasonic vibration on metal forming in micro/meso-scale, an ultrasonic-vibration-assisted microforming system based on magnetostrictive actuation has been developed [33]. This chapter addresses the compensation for the actuation hardware dynamics effect on the ultrasonic vibration generation, and the rapid identification of the resonant frequency of the ultrasonic vibration during the microforming process.

Micromanufacturing refers to fabrication of miniature parts with dimensions ranging from a few micrometers to tens of millimeters. Many fields, including medical, aerospace, military/defense, optics, automotive, consumer products, and communications, have been increasingly demanding miniature devices and components with complex micro-scale features made from a wide selection of materials [2, 3]. In contrast to MEMS approach which is limited to silicon based material and planar shapes, various efforts have been made to miniaturize existing traditional manufacturing processes such as machining, forming and molding. Among these, microforming has been the least investigated. Ultrasonic vibration applied in conventional large scale forming operation has shown to improve the part productivity and quality. Such an enhancement is attributed to effects including localized heating [34], reduction of friction [35], and softening effect of ultrasonic vibration on the workpiece [10]. The ultrasonic-induced enhancement results in significant reduction of the force applied and thus a substantial elongation of the tool life [11]. Furthermore, it has been proposed that the ultrasonic effect might become more pronounced if the vibration occurs at the resonant frequency of the workpiece [12]. However, application of ultrasonic vibration for micro/meso-scale forming operation has not been studied, and the fundamental mechanism is still not clear. To achieve the system miniaturization, the bulky hydraulic actuators typically used in conventional size forming operation need

to be replaced. There is a need for the development of a new type of actuating system optimized for the microforming system and appropriate control strategies.

In this study, we have developed a microforming system based on a magnetostrictive actuator [33]. Magnetostrictive actuators are very promising to address existing challenges in microforming technology. Compared to other actuators such as miniaturized motors and piezoactuators, magnetostrictive actuators have advantages including large actuation frequency range, low input voltage, and high force density [18]-[21]. We note that although these advantages of magnetostrictive actuators have been explored in other precision-positioning applications [22]-[24], no work has been done to utilize them for ultrasonic-vibration-assisted microforming processes. The developed microforming system provides a prototype platform to investigate ultrasonic vibration effect on the load reduction behavior. It is challenging, however, to rapidly and accurately identify the resonance of the system, and maintain the resonant frequency during the microforming process. Such challenges arise because the ultrasonic vibration could be substantially distorted by adverse effects related to the dynamics and nonlinear hysteresis behavior of the magnetostrictive actuation system, and variation in the material properties of the workpiece itself. Therefore, techniques need to be developed to achieve rapid identification and tracking of the vibration resonance during the microforming process.

The main contribution of this chapter is the development of a mechatronic system to achieve rapid identification and tracking of the resonant frequency during the magnetostrictive-actuator-based microforming process. A recently-developed iterative learning control approach [25] is utilized to compensate for the dynamics effect of the magnetostrictive actuation system on the ultrasonic vibration generation. Moreover, to generate the desired vibration waveform for the dynamics compensation, an oscillation regulation circuit is developed, based on the voltage-to-frequency conversion along with the amplitude modulation. Then the Fibonacci search method [26] is utilized to achieve rapid identification of the resonant frequency online. The proposed approach is implemented on the developed magnetostrictive-actuator-based microforming system. The experimental results show that the distortion of the ultrasonic vibration amplitude was significantly reduced by over 95 times across a large excitation frequency range (1 kHz). Moreover, the time needed to identify the resonant frequency was also substantially reduced by over 9 times compared to the conventional swept sine method.

This chapter is organized as follows. In Section II, challenges involved in maintaining the ultrasonic vibration at the resonant frequency of the workpiece are described, followed by the discussion of the dynamics effect of the magnetostrictive actuator on the ultrasonic vibration generation in Section III. The proposed approach and the hardware development to compensate for the dynamics convolution and other adverse effects are described in Section IV, where the experimental results are also presented and discussed. Our concluding remarks are given in Section V.

2.2 ULTRASONIC-VIBRATION-ASSISTED MICROFORMING SYSTEM USING A MAGNETOSTRICTIVE ACTUATOR

The developed magnetostrictive-actuator-based microforming system is pictured in Fig. 2.1. A bidirectional DC motor is utilized to drive a titanium horn via a mechanical guiding rail to deform the workpiece with a relatively large-range, low-frequency motion (i.e., the bulk motion, where the displacement range is around 5~10mm and the frequency is below 1Hz). Then a magnetostrictive actuator (CU18 S/N003, Etrema Products, Inc.) based on Terfenol-D is utilized to drive the horn with high-frequency, low-amplitude vibrations (where the displacement range is below 10 μm, and the vibration frequency ranges from a few kHz to tens of kHz). During the microforming process, the force exerted on the workpiece is measured by a force sensor (KISTLER 9133B21) mounted behind the workpiece, and the displacement of the driving stage is measured by a laser displacement sensor (opto NCDT 1401). By using the experimental platform in Fig. 2.1, we can study the fundamental mechanisms of the ultrasonic vibration effects on the microforming process and the related process control issues.

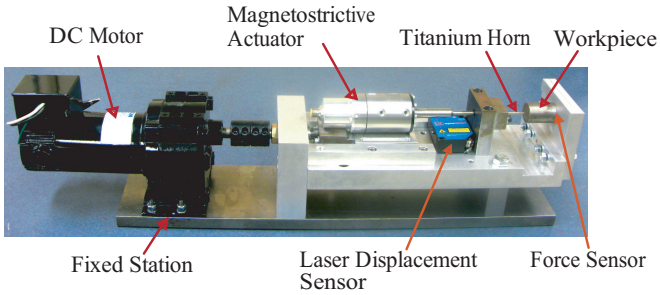

Figure 2.1: The experimental setup of the developed ultrasonic-vibration-assisted microforming system.

This chapter is focused primarily on controlling the behavior of the ultrasonic Terfenol-D transducer in the above system. This transducer is a commercial product (CU18 S/N003) provided by Etrema Products (Edge Technologies, Inc). The manufacturer indicates that its internal structure consists of a Terfenol-D/magnet stack with SmCo magnets and low-hysteresis Terfenol-D alloy (Tb0.28 material). Though not identical, this transducer is similar to the one described in the US patent #6624539 [36]. The dynamic behavior of this transducer is described in the data sheet [37] and has been verified by the characterization tests performed as part of this work. The transducer itself has a resonance at 18 kHz which shifts lower as the device is loaded. When a horn is attached, the dynamics of the transducer output is dominated by the horn dynamics. In our case the horn is designed for an unloaded resonance at 7.5 kHz. The transducer has the capability of being air cooled to control temperature effects. However, since our tests were run at room temperature and under 100V, this was not necessary for the experiments shown in this chapter [37].

Throughout the microforming process, it is challenging to maintain the ultrasonic vibration excitation at the resonant frequency of the workpiece (i.e., the frequency at which the amplitude of the ultrasonic force is maximum) when the ultrasonic frequency is sweeping over the working frequency range. First, the resonant frequency of the workpiece, being dependent on the material property and the geometry of the workpiece, is unknown in general. Thus, to fully exploit the ultrasonic vibration effect, the resonant frequency needs to be quickly identified during the initial stage of the microforming process (Note that the entire microforming process only lasts a few minutes). Secondly, the generated ultrasonic vibration can be distorted by the adverse effects of the magnetostrictive actuation system (as discussed in Section 2.3), as well as by other adverse effects caused by the fluctuation of the environmental temperature, the variation of the geometry of the workpiece, and variation in the material properties of the workpiece. Therefore, a mechatronic system is developed to account for these adverse effects in order to achieve accurate ultrasonic vibration generation during the ultrasonic-vibration-assisted microforming process.

2.3 TERFENOL-D ACTUATOR EFFECT ON ULTRASONIC VIBRATION GENERATION

Hardware dynamics of the magnetostrictive actuator must be accounted of when applying ultrasonic vibration to the microforming process. The amplitude of the ultrasonic vibration applied to the workpiece needs to be maintained around the set point value when the excitation frequency is tuned over a large range. This requirement can be relatively easily satisfied when the vibration frequency is well below the bandwidth of the actuation system (measured by the 3dB drop of the gain from the DC-gain) or the vibration amplitude is relatively small. As the excitation frequency increases, however, the dynamics of the magnetostrictive actuation system along with the related mechanical fixtures can be excited, resulting in large distortions in the vibration amplitude. Moreover, additional distortions can also be generated when the vibration amplitude becomes relatively large (compared to the full displacement range of the magnetostrictive actuator), and as a result, the nonlinear hysteresis effect of the magnetostrictive actuator becomes pronounced [38, 39].

Such a distortion in the vibration amplitude caused by the hardware dynamics effect was measured for the Terfenol-D microforming system described in Section 2.3 . To investigate the hardware dynamics coupling effect on the ultrasonic vibration generation, and develop an effective approach to compensate for such an adverse effect, a computer-based sensing and actuation system was developed, as schematically depicted in Fig. 2.2. The high-frequency vibration displacement of the horn tip was measured by using an inductive displacement sensor (SMU-9000, resolution 0.1μm, Kaman), which replaced the workpiece and force sensor in Fig. 2.1. The amplitude of the vibration at the excitation frequency was then captured by using a lock-in amplifier (SI 410, Boston Electronics) when a sinusoidal input signal was applied to drive the Terfenol-D actuator. The excitation input to the Terfenol-D actuator was generated by using the Matlab-xPC-target package, and then amplified by using a high-current amplifier (Pa-138, Labworks Inc.). During the measurement, the excitation frequency was increased from 7 kHz to 8 kHz with a 10 Hz increment every 1.5 sec. The obtained ultrasonic vibration amplitude vs. frequency is plotted in Fig. 2.3.

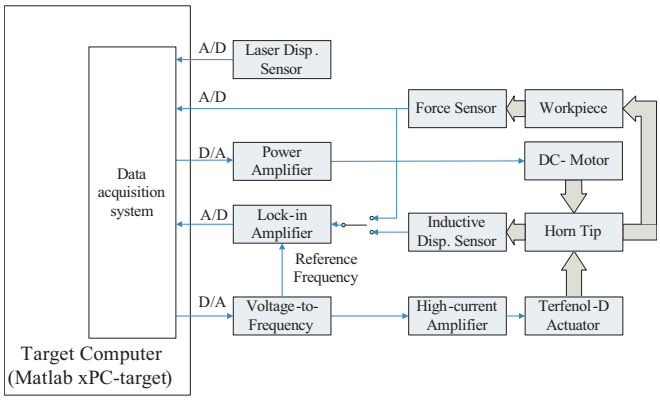

Figure 2.2: The schematic block diagram of the sensing and actuation of the microforming system.

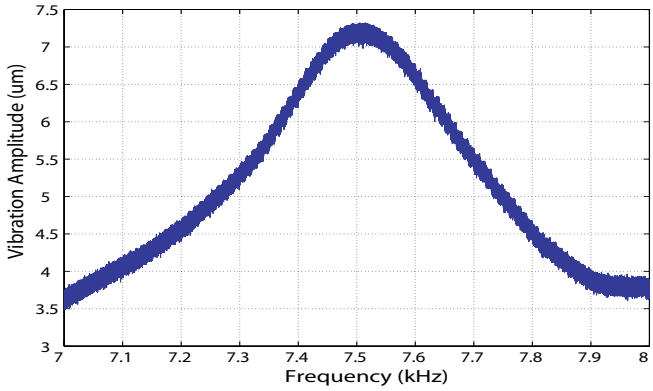

Figure 2.3: The vibration amplitude generated by using the Terfenol-D actuator vs. the excitation frequency when the instrument dynamics effect was not compensated for.

When the dynamics effect of the actuation system was not compensated for, large variation in the ultrasonic vibration amplitude occured. As shown in Fig. 2.3, the ultrasonic vibration amplitude varied over 95% (from 3.7μm to 7.2μm). Such a large variation can adversely effect the microforming process, as the ultrasonic vibration amplitude needs to be maintained at the desired level during the microforming process. More importantly, when actuation dynamics causes variation in the excitation vibration, the resonant frequency of the microforming process cannot be accurately identified. As a result, extraneous barriers are introduced in understanding the mechanism of the ultrasonic vibration effect on microforming process.

The experimental results also demonstrated that the large variation (distortion) of the ultrasonic vibration amplitude shown in Fig. 2.3 was, indeed, caused by the dynamics effect of the

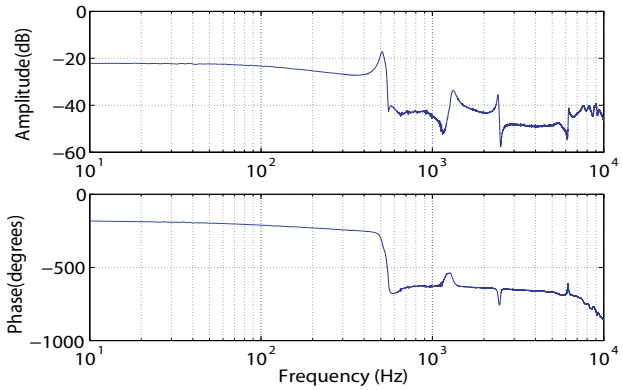

Figure 2.4: The frequency response of the magnetostrictive actuator (Terfenol-D) measured in experiments.

Terfenol-D actuator. The frequency response of the Terfenol-D actuator system (with the displacement of the horn tip as the output) is shown in Fig. 2.4. It is evident that both the gain and the phase variations were pronounced, particularly in the excitation frequency range applied in the experiments (7 kHz to 8 kHz). Such large gain-phase variations in the dynamics response of the Terfenol-D actuator, in turn, led to large amplitude variation in the vibration applied to the workpiece. For example, the gain of the Terfenol-D vibration dynamics increased by 48% as frequency increased from 7 kHz to 7.6 kHz. Correspondingly, the ultrasonic vibration amplitude increased by 86% in the same excitation frequency range. Therefore, it is important to eliminate the Terfenol-D dynamics effect during the microforming process.

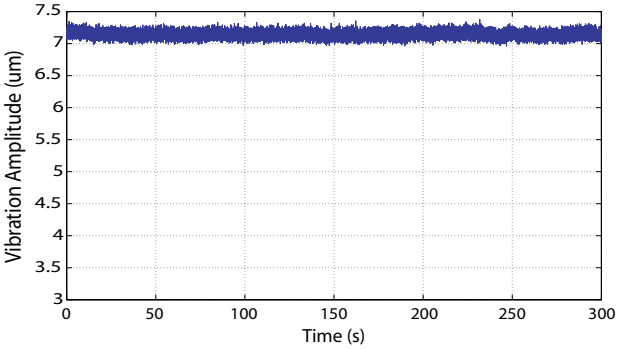

Figure 2.5: The amplitude of the ultrasonic vibration vs. time with the vibration frequency fixed at 7.5 kHz (with no dynamics compensation).

We note that heating was not influential for the voltage levels and test duration time employed in the experiment. This was confirmed by our experimental results. As shown in

Fig. 2.5, the vibration amplitude with the fixed excitation frequency (7.5 kHz) remained almost the same for a duration of five minutes (the variation of the vibration amplitude was less than 0.5%). Note that the five minutes duration was longer than the entire microforming process studied in this chapter. Thus, the heating effect on the Terfenol-D actuator dynamics was negligible in the following experiments.

2.4 COMPENSATION FOR THE MAGNETOSTRICTIVE ACTUATOR DYNAMICS EFFECT ON ULTRASONIC VIBRATION

We propose two inversion-based approaches to compensate for the hardware effect of the magnetostrictive actuator on the ultrasonic vibration generation.

2.4.1 Optimal-Inversion-Based Compensation Method

First, the optimal-inversion technique [40, 41] is utilized to compensate for the hardware dynamics effect on ultrasonic vibration during the microforming process. For a desired vibration amplitude $Y_d(j\omega)$ at a given frequency ω, the feedforward control input to the Terfenol-D actuator, $V_{ff}(j\omega)$, can be obtained by using the optimal inverse of the dynamics model of the Terfenol-D actuation system, $G_t(j\omega)$, as a pre-filter, i.e.,

$$V_{ff}(j\omega) = \hat{G}_t(j\omega)Y(j\omega) \tag{2.1}$$

where $\hat{G}_t(j\omega)$ is the optimal inverse of $G_t(j\omega)$, obtained by minimizing the following cost function [40]

$$\begin{aligned} J(u(\cdot)) = \int_{-\infty}^{+\infty} \{u^*(j\omega)R(j\omega)u(j\omega) + [y_d(j\omega) \\ -y(j\omega)]^* Q(j\omega)[y_d(j\omega) - y(j\omega)]\}\, d\omega \end{aligned} \tag{2.2}$$

In the above cost function, '$*$' denotes the conjugate transpose operation, and $Q(j\omega)$ and $R(j\omega)$ are frequency-dependent, real-valued weights on the tracking error and the input energy, respectively. The obtained optimal inverse $\hat{G}_t(j\omega)$ is given as

$$\hat{G}_t(j\omega) = G_t^*(j\omega)Q(j\omega)[R(j\omega) + G_t^*(j\omega)Q(j\omega)G_t(j\omega)]^{-1}. \tag{2.3}$$

As shown in Eq. (2.2), the optimal inversion approach takes adverse effects including the input

saturation, the modeling error and the disturbances into account when finding the inversion-based feedforward control input $V_{ff}(j\omega)$—through the selection of different values of weight $Q(j\omega)$ relative to $R(j\omega)$ in different frequency ranges. For example, the value of $Q(j\omega)$ should be much smaller than that of $R(j\omega)$ at frequencies where the modeling error, the dynamics uncertainty, and/or the disturbances (such as noise) are large. Thus, the optimal inversion approach provids a systematic approach to designing the feedforward controller for dynamics compensation in ultrasonic vibration generation.

As implied by Eqs. (2.1, 2.2, & 2.3), the efficacy of the optimal inversion technique relies on the model accuracy of the Tefonal-D actuator dynamics, i.e., the tracking error becomes large when the modeling error increases. Such modeling errors arise in implementations due to noise/disturbance effects in the relatively high frequency range, and small dynamics variation and nonlinear hysteresis effect in the relatively low frequency range (both with respect to the system bandwidth). Moreover, the tracking precision can be further limited by the nonlinear hysteresis effects of Terfenol-D actuator. Thus, we propose the use of a recently developed modeling-free inversion-based iterative control (MIIC) approach to further improve the tracking precision.

2.4.2 Iterative-Learning-Control-Based Compensation Method

The MIIC law is depicted in Fig. 2.6. For a desired vibration amplitude at frequency ω, $y_{des}(j\omega)$, the input to the Terfenol-D actuator, $u(j\omega)$, can be obtained by [25],

$$\begin{aligned} u_0(j\omega) &= \alpha y_{des}(j\omega), && k = 0, \\ u_k(j\omega) &= \begin{cases} \frac{u_{k-1}(j\omega)}{y_{k-1}(j\omega)} y_{des}(j\omega), & \text{when } y_k(j\omega) \neq 0, \\ & \text{and } k \geq 1, \\ 0, & \text{otherwise} \end{cases} \end{aligned} \tag{2.4}$$

where α is a prechosen constant (e.g., the DC-gain of the Terfenol-D actuation system), '$f(j\omega)$' denotes the Fourier-transform of the signal '$f(t)$', and $y_k(\cdot)$ is the system output for the input $u_k(\cdot)$ during the k^{th} iteration.

Notice that in the above MIIC law, the inverse of the system dynamics, $u_k(j\omega)/y_k(j\omega)$, is utilized to update the next iterative control input. Particularly, the inverse dynamics are corrected

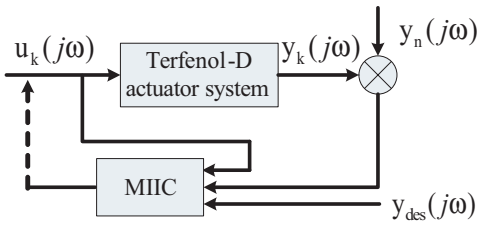

Figure 2.6: The iterative-control scheme to compensate for the Terfenol-D actuator dynamics effect on ultrasonic vibration generation.

in each iteration by using the measured input and output at frequencies where the output tracking is needed, i.e., at frequencies where the component of the desired output is relatively large (in practice, the frequencies that can be tracked by the MIIC technique is limited by the noise level of the system—the frequency component of the desired trajectory can be tracked when the noise level at that frequency is small compared to the component magnitude of the desired output at that frequency, see [25] for details). Therefore, not only is the modeling process—as needed in other model-based ILC approaches—avoided (i.e., modeling–free), but also the variations of the system dynamics are automatically compensated for through the iteration process. These two benefits of the MIIC approach are appealing in practice as the modeling process can be time consuming and prone to errors. Furthermore, the convergence rate of many ILC approaches tends to be limited by the the size of the system dynamics uncertainty, (as the value of the iterative control gain used in these ILC approaches is determined by the size of dynamics uncertainty), i.e., a small iterative control gain has to be chosen to ensure convergence when the dynamics uncertainty is large, resulting in a slow convergence process. Whereas such a limit is eliminated and rapid convergence can be achieved when using the MIIC technique [25]. Moreover, experimental results in [25] also demonstrated that the hysteresis effect of piezotube actuators can be compensated for with the use of the MIIC approach. Thus, it is advantageous to use the MIIC approach to compensate for the instrument dynamics effect on ultrasonic vibration during microforming process.

Hardware challenges, however, exist when implementing the above inversion-based approaches to compensate for the dynamics effect on ultrasonic-vibration-assisted microforming. Note that although the optimal-inverse input (2.1) and the MIIC input (2.4) can be computed offline, data acquisition of ultrahigh-speed sampling rate is needed when implementing these

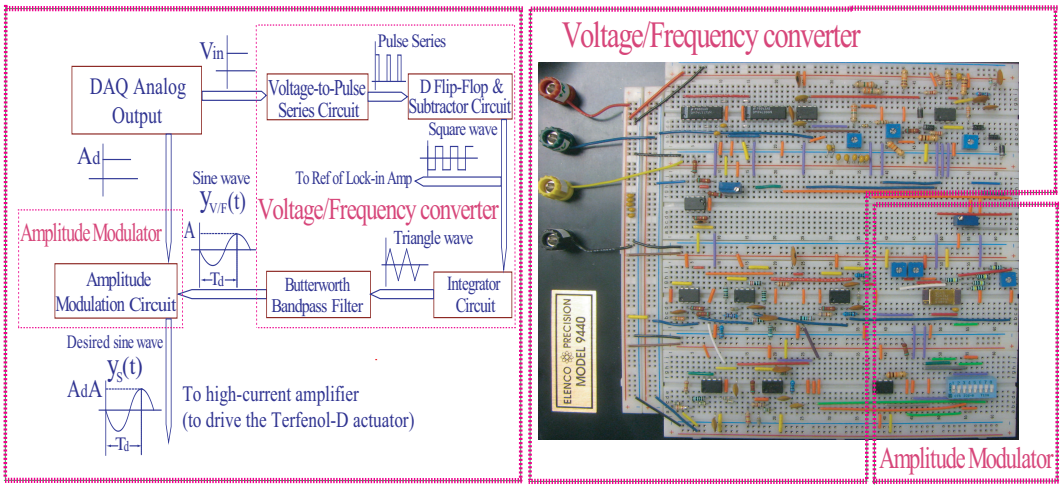

Figure 2.7: (left) The scheme of the oscillation frequency-amplitude regulation circuit, and (right) the diagram of the real circuit construction.

two control techniques directly. For example, for the ultrasonic vibration frequency around 7~8 kHz used in this project, a closed-loop sampling rate over 1 MHz would be needed (This means that within 1 microsecond the system needs to accomplish both an A/D & D/A conversion and the related computations of the control algorithm). Hence, we developed an oscillation regulation circuit based on the voltage-to-frequency conversion, to accurately regulate the ultrasonic oscillations (both the frequency and the amplitude) without resorting to ultrahigh-speed closed-loop data acquisition.

2.4.3 Development of a Vibration Regulation Circuit for Oscillation Waveform Generation

The developed circuit consisted of two primary parts (shown in Fig. 2.7 schematically): a voltage-to-frequency (V/F) converter and an amplitude modulator.

The V/F converter generated a sinusoidal waveform with fixed amplitudes, and a waveform frequency proportional to the input voltage level, i.e.,

$$y_{V/F}(t) = A\sin(kV_{in}t) = A\sin(\omega_d t) \tag{2.5}$$

where the amplitude A was a constant (e.g., $A = 5$), V_{in} is the input voltage to the V/F converter generated by the DAQ analog output, and k is the gain constant that can be tuned by adjusting the time constant of the voltage-to-pulse converter, see Fig. 2.7. The amplitude modulator took

the sinusoidal output of the V/F converter, $y_{V/F}(t)$, as one input, and an analog output of the data acquisition card, A_d, as the other to generate the desired sinusoidal waveform with desired frequency and amplitude (see Fig. 2.7), i.e.,

$$y_s(t) = A_d y_{V/F}(t) = A_d A \sin(\omega_d t) = A_d A \sin(kV_d t) \tag{2.6}$$

The V/F converter was implemented using a V/F converter chip (LM331). The output of the V/F converter consisted of a series of square waves whose duty cycles, D_p, and waveform frequency, f_p, were both proportional to the input voltage level V_{in}, i.e.,

$$D_p = k_p V_{in}, \qquad f_p = \frac{k}{2\pi} V_{in}. \tag{2.7}$$

As the final output needed to be sinusoidal, a conversion circuit based on a flip-flop chip (DM74LS174) was designed to transform the square waveform with varying duty cycle to that with fixed duty cycle of 50%. Then, the sinusoidal waveform with the desired waveform frequency ω_d was obtained by passing the fixed-duty-cycle square waveform through an integrator circuit, followed by an Op-Amp based (LF411A) Butterworth bandpass filter (designed based on a multiplier chip, AD534). Additionally, the square waveform with duty cycle fixed was also sent out as the reference input to the lock-in amplifier.

By using this oscillation regulation circuit, the frequency and the amplitude of the sinusoidal waveform can be regulated between 0 to 10 kHz, and 0 to 10 volts, respectively. For this frequency range, a frequency resolution of 10 Hz and an amplitude resolution of 0.001 volt were achieved. The amplitude resolution was limited by the resolution of the DAQ system, and the frequency resolution can be linearly scaled with respect to the frequency range, which can be adjusted between 0 to 100 kHz through the design of the V/F converter (i.e., by choosing different combinations of resistances and capacitances).

2.4.4 Experimental Implementation: Results & Discussion

The developed oscillation regulation circuit was utilized in experiments to implement both the optimal-inversion approach and the MIIC approach to compensate for the Terfenol-D actuator effect on the ultrasonic vibration generation. The ultrasonic vibration amplitude obtained by using the optimal-inversion approach and that by using the MIIC technique are shown in Fig. 2.8

and Fig. 2.9, respectively. The vibration frequency was between 7 and 8 kHz in both tests, and the result shown in Fig. 2.9 was obtained after 4 iterations. The evolution of the vibration amplitude during the four iterations is also shown in Fig. 2.10. To further evaluate the stability of the MIIC approach in compensating for the Terfenol-D actuator effect on ultrasonic vibration generation, the iterations were conducted for a total of 20 iterations. The obtained relative RMS error of the vibration amplitude, $E_V\%$, vs. iteration numbers is shown in Fig. 2.11, where the relative RMS error, $E_V\%$, is defined as

$$E_V\% = \frac{\|y_{des}(\cdot) - y(\cdot)\|_2}{\|y(\cdot)\|_2} \tag{2.8}$$

and $\|y(\cdot)\|_2$ denotes the standard 2-norm of the amplitude of $y(\cdot)$ over the given frequency range (7 to 8 kHz in this experiment).

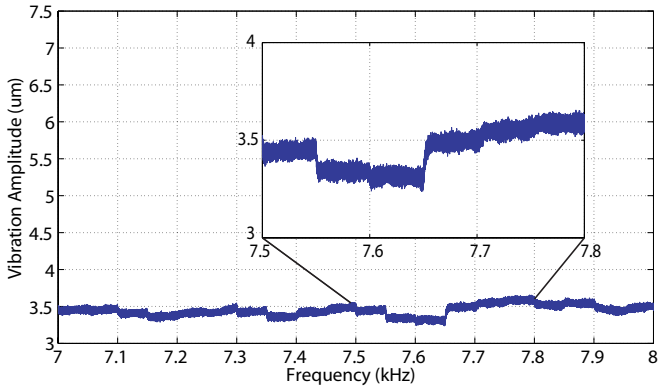

Figure 2.8: The amplitude of the vibration oscillation generated by the Terfenol-D actuator vs. frequency after compensation by using the dynamics inversion method along with the developed oscillation amplitude regulation circuit.

The experimental results clearly demonstrate the efficacy of the proposed two approaches (and particularly, the MIIC technique) in compensating for the effects of the Terfenol-D actuator dynamics on the ultrasonic vibration generation. Comparing Fig. 2.8 with Fig. 2.3, we can see the vibration amplitude variation was reduced by over 13 times (from 95% to 7%) by using the optimal inversion method. However, it becomes very challenging to further reduce the vibration variation (or by using other model-based control approaches using a *fixed* dynamics model). One important limit factor is that the dynamics of the Terfenol-D actuator can vary slightly during daily operations. Such a small albeit critical variation of the Terfenol-D actuator dynamics (to compensation precision) is very difficult to capture by using a fixed dynamics

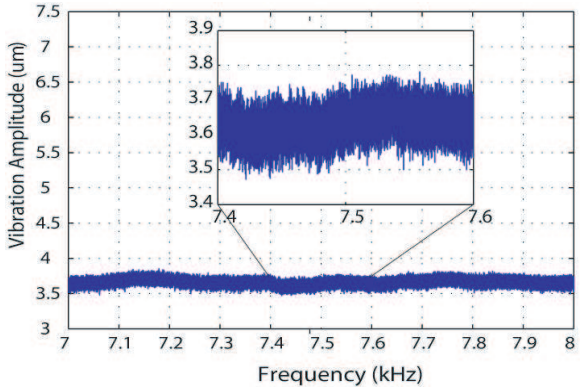

Figure 2.9: The amplitude of the ultrasonic vibration generated by the Terfenol-D actuator vs. frequency after compensation by using the proposed approach (the MIIC technique along with the oscillation amplitude regulation circuit), where the inset is the zoomed-in view over the frequency range of 7.4 to 7.6 kHz.

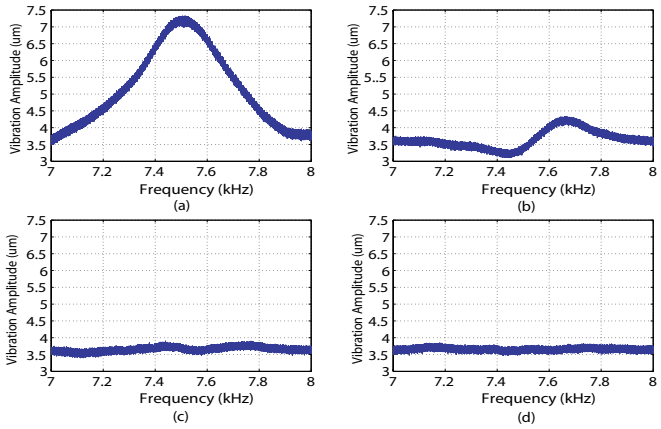

Figure 2.10: The amplitude of the ultrasonic vibration vs. frequency obtained in: (a) the first iteration, (b) the second iteration, (c) the third iteration, and (d) the fourth iteration when using the MIIC technique.

model—it is not convenient in practices to re-model the Terfenol-D dynamics on a daily basis. Additional variation can also be generated by the nonlinear hysteresis effect of the Terfenol-D actuator when the vibration amplitude becomes relatively large with respect to the full range of the Terfenol-D actuator. These challenging issues were successfully addressed by using the MIIC approach, as shown by the experimental results. Compared to the resutls obtained by using the optimal-inversion approach (compare Fig. 2.9 with Fig. 2.8), the variation of the ultrasonic vibration amplitude was further reduced by over 7 times (from 7% to less than 1%), which is over 95 times reduction of the original vibration amplitude variation (compare Fig. 2.9 with Fig. 2.3). Particularly, such a dramatic reduction was achieved with only merely four

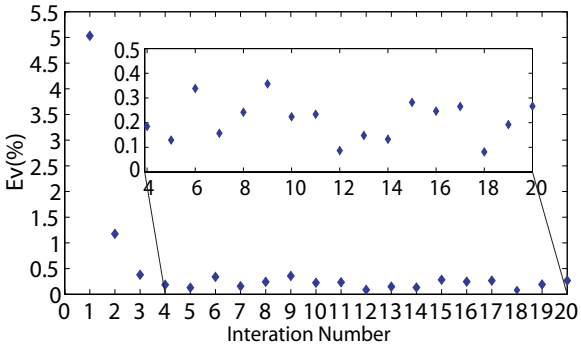

Figure 2.11: RMS relative variation of the vibration amplitude E_V% vs. the number of iterations.

iterations (see Fig. 2.10). Moreover, the reduction was maintained at almost the same level as the number of iterations increased (see Fig. 2.11)—the proposed MIIC-based approach was stable in experimental implementations. Thus, the experimental results clearly demonstrate the efficacy of the proposed approach in cancelling the dynamics convolution effect on the ultrasonic vibration generation.

2.4.5 Rapid Resonant Frequency Identification

It is important to rapidly identify the resonant frequency of the workpiece during the microforming process. As the duration of the entire microforming process is rather short (generally a few minutes), fast identification of the resonant frequency directly leads to an enhancement of the ultrasonic vibration effect on the microforming process. Although tracking of the resonance of the ultrasonic vibration during the microforming process has been considered previously [42, 43], the swept sine method used in that work is time consuming and thereby, cannot be utilized to rapidly identify the resonant frequency. As shown in Fig. 2.12, it took over 150 seconds when the swept sine method was used to identify the resonant frequency on the developed microforming system. Such a long identification time is unacceptable, and moreover, cannot be further reduced as the identification time was dictated by the number of periods needed to measure the oscillation amplitude at each waveform frequency (around 10 periods), the frequency increment during the sweep (10 Hz, the resolution of the V/F converter), and the total frequency range (1 kHz). Evidently, techniques need to be developed to rapidly identify the resonant frequency.

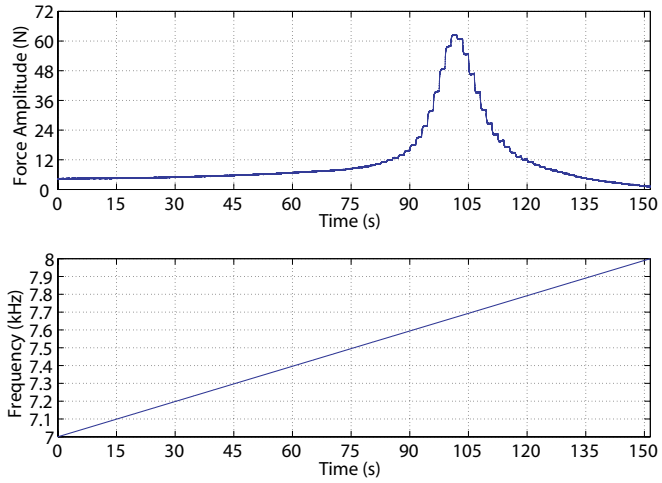

Figure 2.12: (top) The amplitude of the ultrasonic force applied at the workpiece during the resonance identification process by using the swept sine method, and (bottom) the corresponding sweep of the excitation frequency.

In this chapter, we propose to utilize the Fibonacci search method [26] to shorten the time needed to identify the resonant frequency of the workpiece. As the amplitude of the ultrasonic force has only one maximum in the excitation frequency range, the resonant frequency ω^* can be identified as the one at which the gradient of the ultrasonic force (with respect to frequency) is zero, i.e., $dF(j\omega)/d\omega|_{\omega=\omega^*} = 0$. Methods such as the bisection method, the regula falsi method, and the Newton's method (e.g., [44]) are not preferred for rapid resonant frequency identification as gradient (derivative) of the ultrasonic force needs to be obtained in these methods. Thus, the Fibonacci search method is utilized as no derivative of the ultrasonic force is required.

Next we present the implementation of the Fibonacci search algorithm for the rapid resonant frequency identification. First, the Fibonacci fraction sequence $\{R_k \mid k = 1, 2, \cdots\}$ was utilized to determine the frequency values to be searched, where

$$R_k = \frac{F_{N-k}}{F_N}, \quad \text{for } k = 1, 2, \cdots, N \tag{2.9}$$

with F_ks (the Fibonacci numbers) given by

$$\begin{aligned} &F_0 = F_1 = 1, \\ &F_k = F_{k-1} + F_{k-2}, \qquad\qquad k = 2, 3, ... \end{aligned} \tag{2.10}$$

and the length of the Fibonacci fraction sequence N was determined by the desired searching

accuracy, i.e., N was chosen such that

$$R_N = \frac{F_0}{F_N} \leq \frac{\delta}{W}, \tag{2.11}$$

where δ and W were the required searching accuracy and the length of the frequency interval to be searched. Then, the values of the vibration amplitude at the searched frequencies were used to abridge the searched frequency interval for the next search. Particularly, let $\omega_{i,k}$ and $\omega_{f,k}$ be the lower and upper boundary frequencies of the searched frequency interval in the k^{th} search, respectively; ω_r be the resonant frequency to be identified; and $A_{l,k}$ and $A_{h,k}$ be the ultrasonic force amplitudes at the two added search frequencies $\omega_{l,k}$ and $\omega_{r,k}$ that were determined by (see Fig. 2.13)

$$\begin{aligned} \omega_{l,k} &= \omega_{i,k} + W * R_k \\ \omega_{h,k} &= \omega_{f,k} - W * R_k \end{aligned} \tag{2.12}$$

Then the resonant frequency, ω_r, can be identified with the desired accuracy after N number of searches [26].

In this project, a Fibonacci sequence of length $N = 11$ was used. The length was determined by Eq. (2.11), with the identification accuracy at 10 Hz, and the ratio of the identification accuracy to the uncertainty interval at 0.01 (the range of the searched frequency interval was 1 kHz). Moreover, the desired identification accuracy can also be guaranteed after 11 searches, or equivalently, 11 measurements of the force amplitude. For the developed microforming system studied in the experiment, these 11 measurements of force amplitude are translated to 16.5 seconds identification time.

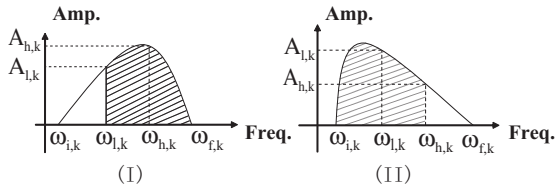

Figure 2.13: The two scenarios of force amplitude comparison occurring in the Fibonacci search method, where the shaded area denotes the abridged interval for the next search.

The experimental implementation results agreed with our predictions. The Fibonacci search method was implemented by using a S-function in Matlab-Simulink. The measured ultrasonic

vibration force amplitude during the searching process is shown in Fig. 2.14. The resonant frequency (i.e., the frequency with the maximum force amplitude) was identified in 16.5 seconds with identification error less than 10 Hz after a mere of 11 force amplitude measurements—as we predicted by the Fibonacci search algorithm. Compared to the traditional frequency swept sine method, the Fibonacci search method dramatically reduced the number of measurements and the total identification time by over 9 times (from 101 measurements to 11 measurements, and from 151.5 seconds to 16.5 seconds, respectively). Such a substantial reduction of the searching time can enhance the ultrasonic vibration effect on microforming process by significantly extending the ultrasonic vibration effect time, which facilitates the understanding of the mechanism of the ultrasonic vibration effect on microforming process. Therefore, the experimental results demonstrate the efficacy of the proposed Fibonacci search approach in rapidly identifying the resonant frequency.

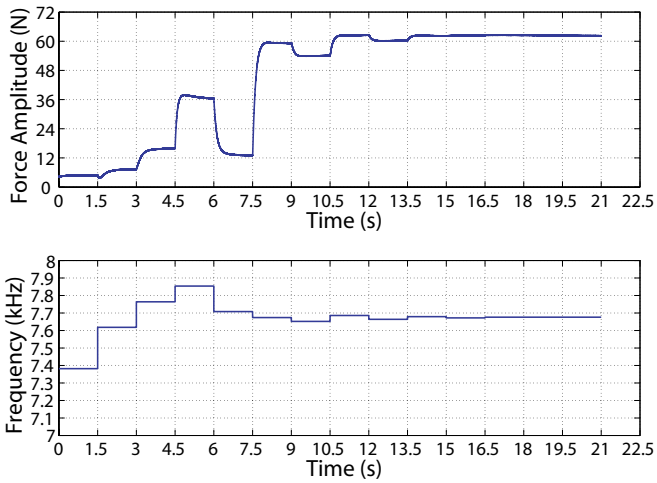

Figure 2.14: (top) The amplitude of the ultrasonic force applied at the workpiece during the resonance identification process by Fibonacci search method, and (bottom) the corresponding change of the excitation frequency.

2.5 Conclusion

In this chapter, a mechatronic system was developed to compensate for the actuator hardware dynamics effect on an ultrasonic-vibration-assisted microforming system and to achieve rapid resonance identification during the microforming process. A modeling-free inversion-based iterative control (MIIC) algorithm was proposed to compensate for the dynamics effect of the

magnetostrictive actuator on the ultrasonic vibration, and an oscillation frequency and amplitude regulation circuit was developed to implement the proposed MIIC approach. The Fibonacci search method was utilized to achieve rapid identification of the resonant frequency during the ultrasonic-vibration-assisted microforming process. The proposed mechatronic system was demonstrated on an ultrasonic-vibration-assisted microforming system based on a magnetostrictive actuator. The experimental results were presented with the dynamics effect of the magnetostrictive actuator significantly reduced by over 95 times and the time for resonant frequency identification reduced by over 9 times. The compensation for the hardware dynamics effect and the rapid identification of the resonant frequency will facilitate the research in understanding the fundamental mechanisms of ultrasonic vibration effect on microforming process, as well as the development of process control for microforming system.

Chapter 3

Control of a Magnetostrictive-Actuator-based Micromachining System for Optimal High-speed Microforming Process

abstract

In this chapter, the process control of a magnetostrictive-actuator-based microforming system is studied. Microforming has recently become an emerging advanced manufacturing technique for fabricating miniaturized products in applications including medical devices and microelectronics. Particularly, miniaturized desktop microforming systems based on unconventional actuators possess great potential in both high productivity and low cost. Process control of these miniaturized microforming systems, however, is challenging and still at its early stage. The challenge arises from the complicated behaviors of the actuators employed, the switching and the transition involved in the actuation/motion, and the uncertainty of the system dynamics during the entire microforming process. The dynamics and the hysteresis effects of magnetostrictive actuator can be excited, resulting in positioning errors of the workpiece during both the trajectory tracking and the output transition phases. The rapid tracking-transition switching is also accompanied with substantial variation of the system dynamics. Moreover, the process control is further complicated by the use of multi-stage actuators and the augmentation of ultrasonic vibrations to the microforming process. In this chapter, a control framework integrating iterative learning control and an optimal transition trajectory design along with feedforward-feedback control is proposed to achieve high-speed and high-quality microforming. The efficacy of the proposed control approach is demonstrated through experiments.

3.1 Introduction

Micromachining has recently emerged as an important advanced manufacturing technology for fabricating miniaturized products. Particularly, micromachining technology has been employed for manufacturing products in a broad range of areas including MEMS [45], electronics [46], medical devices [47], and bioengineering [48]. Compared to conventional manufacturing techniques, micromachining possesses advantages in being able to process a wider variety of materials, have a higher product accuracy, and machine parts of complex geometry shapes [49, 50]. To fully exploit these advantages, advanced control techniques are required to compensate for the adverse effects existing in the manufacturing process, and take into account the motion and positioning needs of different phases of the microforming process. Current work on micromachining process control, however, is still largely limited to conventional proportional-integral-derivative (PID) types of methods [51, 52]. In this chapter, the control of a desktop mciromachining system based on a dual-stage magnetostrictive actuator is studied, and a framework of advanced control techniques is developed to achieve both high quality and high efficiency in the microforming process.

Advanced control technologies have become an indispensable part of micromachining system. With the replacement of conventional electrical motors by smart actuators (such as the magnetostrictive actuators) in the micromachining systems [53, 54], the need for advanced control in micromachining becomes exigent. Compared to electrical motors, smart actuators offer larger force output and higher bandwidth of motion with relatively smaller physical size, thereby, becoming a better choice for attaining miniaturized footprint in desktop micromachining systems [55, 56]. However, due to the nonlinear hysteresis behavior coupled with the vibrational dynamics of these actuators, additional control challenges arise [57]-[61]. These smart-actuator-related adverse effects become more pronounced and can vary substantially during high-speed, large-range motion — to achieve high-efficiency micromachining under a broad range of operation conditions (e.g., machining both small size and relatively large size workpieces). Therefore, to fully exploit the advantages of micromachining systems, advanced control techniques need to be developed.

In particular, high-speed, high-quality microforming processes demand the development of

advanced control technologies. Although modeling of the hysteresis of smart actuators such as magnetostrictive actuators has been addressed recently [60, 61], little work has been reported to account for the positioning/motion needs of the entire microforming process [62]. In addition to the hysteresis and dynamics effects of the magnetostrictive actuators employed, the system dynamics and the operating conditions (i.e., the boundary conditions of the system dynamics) can vary and shift substantially during different phases of the entire micromachining process (e.g., from the pre-welding phase to the welding phase) [63, 64], particularly when operating on soft materials such as plastic. With these dramatic dynamics and hysteresis variations, it becomes challenging to achieve precision positioning and motion control. For example, large change of system dynamics occurs when engaging the workpieces to initiate the forming during the pre-welding phase, or when the workpices are softened and then hardened during the welding phase. As a result, it becomes difficult to achieve rapid transition of the workpieces without induced post-transition vibrations. Moreover, the need to quickly identify the pre-welding to welding transition is further complicated by the noisy measurement during the microforming. These challenges motivated this work.

The main contribution of the chapter is the development of a control framework for the entire microforming process to achieve optimal high-speed microforming. First, a recently-developed iterative control technique [17] is combined with the design of the transition trajectory to achieve rapid engagement of the workpieces without inducing post-engagement oscillations. Then Kalman filtering is employed to rapidly detect and identify the pre-welding to welding phase transition by accurately estimating the interaction force from the measured noisy data. The identified condition of the pre-welding to welding transition is then utilized in the design of the optimal transition trajectory based on the optimal output tracking of non-periodic tracking-transition switching [27]. The obtained optimal transition trajectory is then tracked through a feedforward-feedback controller without post-transition oscillations. The proposed control framework is illustrated by implementing it in the welding of two ABS plastic workpieces. The experimental control results and welded parts demonstrate the efficacy of the proposed approach in achieving optimal high-speed microforming and a substantial improvement of the welding quality.

The chapter is organized as follows. In Section 3.2, the control objectives of the microforming process are formulated, based on an analysis of the challenges involved in achieving high-efficiency and high-quality microforming. In Section 3.3, the proposed control framework is presented, and followed by the experimental implementation and results discussion in Section 3.4. Our conclusion is given in Section 3.5.

3.2 Control Issues in the Dual-stage Microforming System

The dual-stage microforming system, as pictured in Fig. 3.1 (a), utilizes two magnetostricitive actuators in a dual-stage configuration to achieve precision motion control in both large-range displacement (~1 mm) and ultrasonic vibration (vibration amplitude: 1~10 um). A six-bar lever mechanism is designed and fabricated around the large-range magnetostrictive actuator to generate the large-range motion (see Fig. 3.1 (b)), while a high bandwidth magnetostrictive actuator (called the small-range magnetostrictive actuator below) was employed to generate the ultrasonic vibration. The large-range magnetostrictive actuator was designed and home-made using a Terfenol-D transducer, and the strain response of the Terfenol-D was amplified by using friction and backlash-free joints [65]. During the microforming process, the force exerted on the workpieces, the displacement of the large-range motion, and the temperature of the Terfenol-D transducer (for large-range motion) are measured using, respectively, a force sensor (KISTLER 9133B2), a capacitive sensor (CPL-190, LION Precision), and a thermometer (Fluke 50D K/J). As the temperature varies significantly during high-speed, large-range microforming — due to the large current passing through the coils of the Terfenol-D actuator, compressed air is injected to cool down the large-range magnetostrictive actuator.

Precision control of the dual-stage micromachining system is crucial to ensure both high quality and high efficiency in microforming. As illustrated in Fig. 3.2, the microforming process consists of the pre-welding phase and the welding phase. During the pre-welding phase, the large-range actuation system needs to drive the workpiece holder to quickly engage the workpieces to the horn tip without inducing post-engagement oscillations (workpiece holder moves upward by h_0 from Fig. 3.2 (a) to (b)). Once the two workpieces are engaged to the titanium horn with the required force level (the required force level is workpiece dependent and

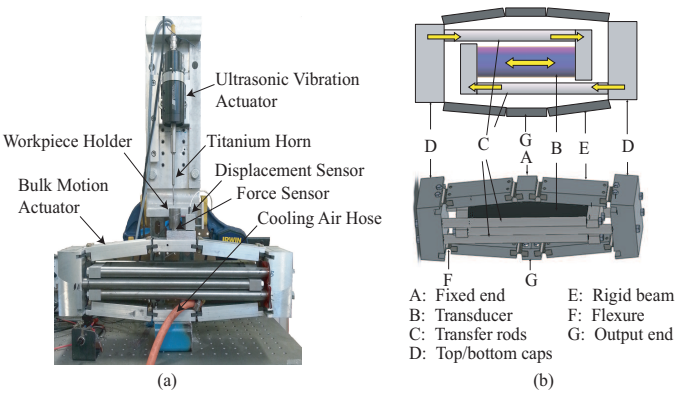

Figure 3.1: (a) Experimental setup; (b) the structure of the large-range actuator.

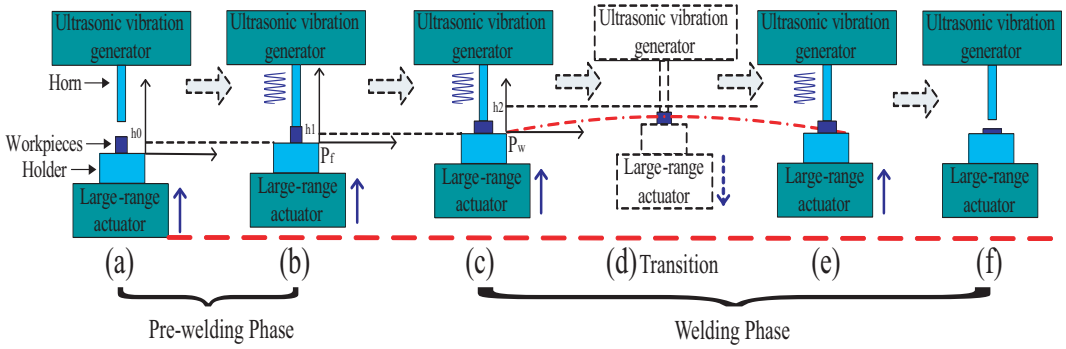

Figure 3.2: The scheme of the microforming phases.

can be pre-determined via experiments), an ultrasonic vibration is applied to the workpiece at its resonant frequency. Preliminary results showed that with the ultrasonic vibration in place, welding is induced when the compression depth of the workpieces is maintained at a certain displacement level (i.e. the holder moves to position P_f in Fig. 3.2 (b)). Due to the softening effect of the ultrasonic vibration [66], the workpieces are further compressed (i.e. the holder at position P_w in Fig. 3.2 (c)) and then start to join together. Once the welding starts, the horn-workpiece interaction force drops rapidly, signifying the transition from the pre-welding phase to the welding one. Thus, to ensure the welding quality, the pre-welding to welding transition needs to be quickly identified, which, in turn, requires that the interaction force and its gradient must be accurately quantified during the pre-welding phase. As the horn could indent and penetrate the welding workpieces, resulting in damage of the workpieces and the horn, it is crucial to avoid post-transition oscillation right after the pre-welding to the welding phase transition (as depicted in Fig. 3.2 (c)–(e)). During the welding process, to achieve the desired penetration depth in the finished workpieces, the holder must be maintained at the position where

the welding initially occurs (i.e. P_w in Fig. 3.2 (c)). However, the interaction force between horn and workpiece continuously decreases as the welding continues, and the workpieces join together and gradually detach from the horn. Finally, The welding phase and thereby the entire microforming are terminated when the interaction force drops to zero in Fig. 3.2 (e). During the entire welding process, the ultrasonic vibration also needs to be maintained at the resonant frequency of the workpieces, in spite of significant variation of the resonant frequency due to the softening of the workpieces during the microforming process.

Thus, in summary, the control objectives of the microforming process can be formulated as:

$O1$ During the pre-welding phase, rapidly engage the workpieces to the titanium horn and reach the forming position P_f without inducing post-engagement vibration of the workpiece holder;

$O2$ During the pre-welding phase, quickly identify the pre-welding to welding phase transition by using the measured horn-workpiece interaction force;

$O3$ During the welding phase, rapidly transit the holder position back to the welding-start position P_w, without inducing post-transition vibrations; then maintain the holder position at P_w in spite of continuous drop of the horn-workpiece interaction force that leads to the loss of horn-workpiece contact;

$O4$ During the entire microforming process, rapidly identify the resonant frequency of the workpieces, then maintain the ultrasonic vibration closely around the resonant frequency.

We focus, in the following, on the first three objectives above — the fourth objective of identifying and tracking the resonant frequency in ultrasonic vibration excitation has been addressed in our previous work [67].

3.3 Optimal High-Speed Motion Control Of Microforming Process

In this chapter, we propose a control framework that integrates a recently-developed iterative control technique [17] with Kalman filtering and the optimal trajectory design for non-periodic tracking-transition switching [27]. As depicted in Fig. 3.3, the iterative control technique is

utilized to achieve rapid engagement of the workpieces without inducing post-engagment vibrations ($O1$), and the Kalman filter is employed to quickly detect the pre-welding to welding transition ($O2$). Then an optimal transition trajectory design for nonperiodic tracking-transition switching [27] is combined with feedforward-feedback to achieve rapid point-to-point output transition during the welding process ($O3$).

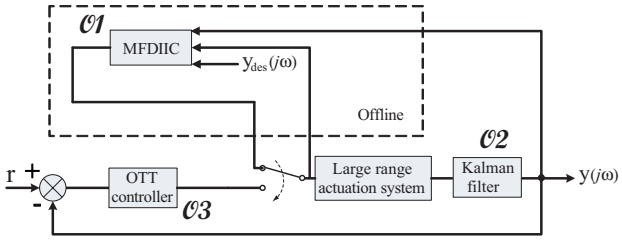

Figure 3.3: The block diagram of the proposed control system for the microforming process.

3.3.1 Iterative learning control for rapid engagement in pre-welding

We propose to accurately track a pre-specified desired trajectory via *a priori* iterative learning, i.e., the ILC algorithm is applied in off-line iteration to achieve precision tracking of a given desired trajectory with the workpieces loaded, and the converged iterative input is applied in the microforming process with the workpieces replaced by a new pair. As the variation of the workpieces is small, the effect of the workpiece variation is negligible as confirmed by our preliminary results, i.e., the converged iterative input can be applied to batch-process the same type of workpieces. Specifically, the following exponentially increasing/decreasing trajectory, shown in Fig. 3.4, is chosen as the desired trajectory of the workpiece holder during the pre-welding process,

$$d(t) = \begin{cases} d_0 \times u(t - T_1)\left(1 - \mathrm{e}^{-k(t-T_1)}\right), t \in [0,\ T/2], \\ d_0 \times u(T - T_2 - t)\left(1 - \mathrm{e}^{-k(T-t-T_2)}\right), t \in [T/2,\ T], \end{cases} \tag{3.1}$$

where d_0 is the desired output displacement of the large-range actuation system at the forming position, $u(t)$ is the unit step function, and T denotes the time period pre-chosen to be large enough for the whole pre-welding phase, i.e., an half of the period, T/2, shall be larger than the duration of the pre-welding phase as only the first half of the trajectory will be applied during the microforming process (the second half of the trajectory with a long and smooth transition

to zero avoids unwanted oscillations caused by sudden change of the output). The exponential coefficient k can be used along with the iterative control algorithm below to achieve high-speed engagement, i.e., the coefficient k can be adjusted by using, for example, the bi-section algorithm in the iterative learning algorithm until the coefficient k cannot be further increased, i.e., until the tracking error reaches the threshold value and cannot be further reduced.

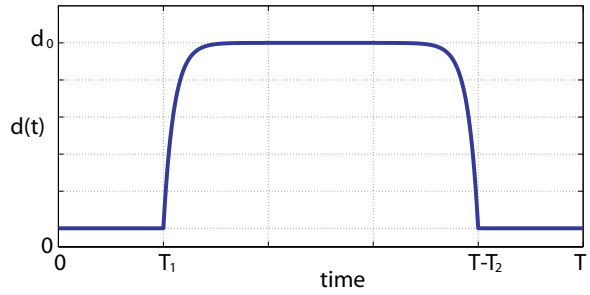

Figure 3.4: The exponentially increasing/decreasing trajectory designed for the pre-welding phase.

The recently-developed modeling-free differential-inversion iterative control (MFDIIC) approach [68] is utilized to track the above desired trajectory,

$$
\begin{aligned}
u_0(j\omega) &= \alpha \times y_d(j\omega), && k=0,\\
u_1(j\omega) &= \tfrac{u_0(j\omega)}{y_0(j\omega)} \times y_d(j\omega), && k=1,\\
u_k(j\omega) &= u_{k-1}(j\omega) + \tfrac{\rho}{\mathbf{S}_\beta} \sum_{i=1}^{N} \left(\beta_i \tfrac{I_{u,k-i}(j\omega)}{I_{y,k-i}(j\omega)}\right) \times e_{k-1}(j\omega),\\
&\qquad \text{with} \quad N = 1, 2, \cdots, k-1, && k \geq 2,\\
e_k(j\omega) &= y_d(j\omega) - y_k(j\omega),\\
I_{u,k}(j\omega) &= u_k(j\omega) - u_{k-1}(j\omega),\\
I_{y,k}(j\omega) &= y_k(j\omega) - y_{k-1}(j\omega),\\
\mathbf{S}_\beta &= \sum_{k=1}^{N} \beta_k
\end{aligned}
\tag{3.2}
$$

where '$f(j\omega)$' denotes the Fourier-transform of the signal '$f(t)$', $y_k(\cdot)$ is the output for the input $u_k(\cdot)$ during the k^{th} iteration, $y_d(j\omega)$ is the desired output, α is a pre-chosen constant (e.g., the DC-gain of the system), $\beta_i \in (0,\ 1)$ is the weighting factor, and $\rho \in (0,\ 1)$ is the coefficient selected to ensure the convergence of the iteration. This data-driven algorithm explores all the input-output responses of the system in the past N iterations to update the control input in current iteration, and the modeling error due to the use of a *fixed* model in the ILC law–as commonly employed in ILCs [69, 70]–is avoided. The iterative update of the system model

not only obviates the pre-modeling process that can be time-consuming and prone to errors, but also is robust in accounting for quasi-static system variations without tracking performance tradeoff. This feature is particularly attractive for microforming as the dynamics of the large-range actuation system changes substantially when the workpieces are engaged, whereas it is practically infeasible to account for that change through re-modeling each time — in order to maintain the tracking precision. Moreover, it has been demonstrated [17] that the MFDIIC algorithm above can compensate for both the hysteresis and the dynamics effects of hysteresis-dynamics systems including magnetostrictive actuator systems.

We realize that techniques such as the optimal state-transition technique [71], the optimal output transition technique [29], or the input-shaping technique [72], might be employed for the output transition during the pre-welding process. However, the dynamics of the large-range actuation system can change significantly during the pre-welding phase due to the load change, and thereby, severely limits the performance of these model-based approaches in practice. The proposed MFDIIC method not only addresses this issue via iterations, but also achieves fast and smooth engagement by adjusting the transition coefficient. The superior tracking performance of the MFDIIC algorithm over feedback control has been clearly demonstrated in experiments [17].

3.3.2 Kalman filtering approach to rapid detection of the pre-welding to welding transition

Central to rapid identification of the pre-welding to the welding phase transition is to accurately quantify the horn-workpiece interaction force online during the entire pre-welding process. We propose to employ the Kalman filtering to optimally estimate the force [73],

$$\hat{x}[k] \quad = (A - G[k]CA)\hat{x}[k-1] + G[k]m[k], \tag{3.3}$$

where

$$A = \begin{bmatrix} 0 & 1 \\ 0 & 0 \end{bmatrix}, C = \begin{bmatrix} 1 & 0 \end{bmatrix}, \tag{3.4}$$

$m[k]$ is the measured force, and the Kalman gain $G[k]$ is given by

$$G[k] = P^f[k]C^T\left(CP^f[k]C^T + R\right)^{-1}, \tag{3.5}$$

with the estimation error covariance $P^f[k]$ given by the following Algebraic Riccati equation

$$P^f[k] = AP^f[k-1]A^T + Q$$
$$-AP^f[k-1]C^T\left(CP^f[k-1]C^T + R\right)^{-1}CP^f[k-1]A^T[k-1], \tag{3.6}$$

where Q and R are the process noise covariance and the covariance of the force/displacement measurement noise, respectively, both of which can be experimentally quantified.

To identify the phase transition, the gradient of the interaction force w.r.t. time, i.e., the force drop, is estimated in discrete-time domain by using the above estimated force values over successive time periods of chosen duration via, e.g., the Euler method. Then the pre-welding to welding transition instant is identified as the first time instant at which the detected force drop is larger than the threshold value. For given materials to be welded, the threshold value can be determined *a priori* through experiments (see Sec. 3.4.1 below).

Similarly, the Kalman filter is also designed to optimally estimate the displacement and velocity of the large-range motion from the measured sensor data. Particularly, the estimated displacement and velocity values at the pre-welding to welding transition instant specify the boundary conditions for the optimal output transition trajectory design below.

3.3.3 Optimal transition trajectory design and tracking in welding process

Once the pre-welding to welding transition instant is identified, rapid pre-welding to welding phase transition is achieved by combining the feedforward-feedback control with the recently-developed optimal transition trajectory design for non-periodic tracking-transition switching [27]. As the total transition time (from the identified starting instant of the transition to the instant when the workpiece holder moves back to the welding-start position P_w) is rather short, and the output transition range is small, the hysteresis effect, the creep effect and the system variation are small. Therefore, the large-range actuation system during the transition period can be adequately modeled as a linear time invariant (LTI) system,

$$\dot{x} = Ax + Bu, \qquad y = Cx, \tag{3.7}$$

with the input and output, $u(\cdot), y(\cdot) \in \mathfrak{R}$, the state $x(\cdot) \in \mathfrak{R}^n$, and a relative degree of r [74]. For mechanical systems such as the large-range actuation system here, the relative degree r = 2. The

optimal transition trajectory is obtained by transforming the system via the state transformation $\mathcal{T}$

$$\begin{bmatrix} \xi(t) \\ \eta_s(t) \end{bmatrix} = \mathcal{T}x(t) = \begin{bmatrix} \mathcal{T}_\xi \\ \mathcal{T}_\eta \end{bmatrix} x(t) \tag{3.8}$$

into the output tracking form,

$$\begin{aligned} \dot{\xi}(t) &= I_{up}\xi(t) + B_\xi y^{(r)}(t) \\ \dot{\eta}(t) &= A_\eta \eta_s(t) + B_\eta \mathbb{Y}(t) \end{aligned} \tag{3.9}$$

$$I_{up} = \begin{bmatrix} \mathbf{0} & \mathbf{E} \\ 0 & \mathbf{0} \end{bmatrix}_{r\times r}, B_\xi = \begin{bmatrix} \mathbf{0} \\ 1 \end{bmatrix}_{r\times 1},$$

where E denotes a $(r-1)\times(r-1)$ identity matrix, $\xi = \mathcal{T}_\xi x(t)$ is the vector of the output and its derivatives,

$$\xi(t) = [y(t), \dot{y}(t), \cdots, \frac{d^{r-1}y_k}{dt^{r-1}}]^T,$$

and $\eta(t)$ are the internal dynamics states.

Then the optimal transition output is obtained by first, stabilizing the output subdynamics (3.9) with the following static state-feedback controller H_ξ

$$y^{(r)}(t) \quad = \quad H_\xi \xi(t) + \gamma(t)$$

to arrive at

$$\begin{aligned} \dot{\xi}(t) \quad &= \quad (I_{up} + B_\xi H_\xi)\xi(t) + B_\xi \gamma(t) \\ &\triangleq \quad \hat{A}_\xi \xi(t) + B_\xi \gamma(t) \end{aligned} \tag{3.10}$$

and secondly, minimizing the following cost function to obtain the optimal input gain γ^*,

$$\begin{aligned} \min_{\gamma(\cdot)}(T,\gamma) \quad &= \min_{\gamma(\cdot)} \int_{t_i}^{t_f} \gamma(\tau)^T R_\gamma \gamma(\tau) d\tau \\ &= \min_{\gamma(\cdot)} \int_{t_i}^{t_f} (\mathbb{Y}^T \mathbb{H}_\mathbb{Y}^T) R_\gamma (\mathbb{H}_\mathbb{Y} \mathbb{Y}) d\tau \\ &= \min_{\gamma(\cdot)} \int_{t_i}^{t_f} Y^T(\tau) R_\gamma Y(\tau) d\tau \\ \text{where} \qquad & \mathbb{H}_\mathbb{Y} = [-H_\xi \quad 1], \quad \mathbb{Y} = [\xi_d(t) \quad \tfrac{d^r y_d}{dt^r}(t)]^T. \end{aligned} \tag{3.11}$$

With the given boundary conditions, i.e., the desired output and its derivatives right before and after the transition, $\xi_d(t_i)$ and $\xi_d(t_f)$, respectively, the optimal input $\gamma^*(\cdot)$ can be readily obtained as [71]

$$\gamma^*(t) = R_\gamma^{-1} B_\xi^T e^{\hat{A}_\xi^T (t_f - t)} g^{-1}(T) \left[\xi_d(t_f) - e^{\hat{A}_\xi (T_1 - t_i)} \xi_d(t_i) \right], \quad \text{for } t \in [t_i, t_f], \tag{3.12}$$

where $g(T)$ is the controllability Grammian,

$$g(T) = \int_0^T e^{\hat{A}_\xi (T-\tau)} B_\xi R_\gamma^{-1} B_\xi^T e^{\hat{A}_\xi^T (T-\tau)} d\tau, \tag{3.13}$$

and the optimal output transition trajectory is obtained by flowing the stabilized output subdynamics Eq. (3.10) forward with the above γ^* as the input. Note that the initial boundary condition, $\xi_d(t_i)$, i.e., the displacement and the velocity of the large-range motion at the identified pre-welding to welding transition instant, are estimated by using the measured displacement via the Kalman filter; and the final boundary conditions, $\xi_d(t_f)$, are obtained by setting the displacement, $y_d(t_f)$ the same as $y_d(t_i)$ of the initial boundary condition, and the derivative, $\dot{y}_d(t_f)$, at zero as required in $O2$.

The above optimal transition trajectory design achieves smooth output transition without inducing post-transition oscillations. Compared to other approaches to output transition such as the optimal output transition technique that minimizes the input energy [29], the method above directly minimizes the output energy (see Eq. 3.11), thereby avoiding oscillations in the trajectory designed, particularly for systems of dynamics with lightly-damped resonant peaks. The corresponding control input that tracks the desired transition trajectory without inducing post-transition oscillations can be obtained by using the previewed stable-inversion approach (see [28] for details). Finding such an input, however, requires an accurate dynamics model of the large-range actuation system. Contrarily the above optimal transition trajectory design, only requires the relative degree of the system to be known, and hence, the transition trajectory can be easily redesigned even when the relative degree changes due to, for example, the reconfiguration of the system. Rather than finding the model of the large-range actuation system (prone to uncertainties and measurement noise), we propose to utilize feedforward-feedback control to track the designed transition trajectory.

3.3.4 Desired output transition trajectory tracking

A feedforward-feedback two-degree-of-freedom controller (see Fig. 3.5) is employed to track the optimal transition trajectory designed above to achieve a smooth pre-welding to welding phase transition. For simplicity and robustness, the 2DOF controller combines PI feedback control with DC-Gain feedforward control, i.e., the feedforward input is obtained by scaling the desired output trajectory by the DC gain of the large-range actuation system. As the boundary conditions of the transition are measured online and unknown a priori, the optimal transition trajectory needs to be designed online. Thus, such a 2DOF control structure not only eases the implementation of the online design of the optimal transition trajectory, but also accounts for the uncertainty of the large-range actuation system dynamics via feedback while exploiting feedforward for trajectory tracking.

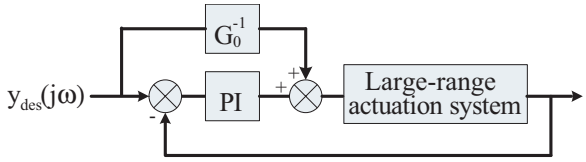

Figure 3.5: The feedforward-feedback controller employed to track the optimal transition trajectory during the pre-welding to welding phase transition.

3.4 EXPERIMENTAL IMPLEMENTATION

In this section, the proposed control framework is applied to the dual-stage microforming system in Fig. 3.1. The experimental results are presented and discussed below to illustrate the proposed control framework in achieving the three identified control objectives (see Sec. 3.2) in the entire microforming process.

High-speed tracking in pre-welding phase

We started by specifying the desired transition trajectory for the pre-welding phase first (see Eq. (3.1)). Based on the preliminary work, the following exponential trajectory was chosen as the desired trajectory,

$$d(t) = \begin{cases} 78 \times u(t-0.05)\left(1-\mathrm{e}^{-k(t-0.05)}\right), t \in [0,\ \ 2.05], \\ 78 \times u(4.05-t)\left(1-\mathrm{e}^{k(t-4.05)}\right), t \in [2.05,\ \ 4.1], \end{cases} \tag{3.14}$$

where the desired forming position at 78 μm was chosen based on the preliminary results, so were the total transition period of 4.1 seconds, and the preactuation and postactuation time of 0.05 second respectively, as the preliminary work indicated that the welding occured within 2 seconds after the microforming process started, and 0.05 second was long enough for the MFDIIC algorithm to achieve accurate tracking without the finite pre- and post- actuation time effect [27, 75]. Such a desired trajectory was tracked by using the MFDIIC algorithm iteratively offline with the horn-workpiece contact, and the tracking of the above transition trajectory with exponential coefficient $k = 15$ obtained by using the MFDIIC technique (after 10 iterations) is shown in Fig. 3.6, which clearly demonstrated that the MFDIIC technique was capable of compensating for both the dynamics and hysteresis effects of the large-range actuation system, and arriving at precision trajectory tracking — the relative RMS tracking error was at 2.94% (see Fig. 3.6 (b)). As a result, the workpieces were rapidly engaged to the horn at the forming position without post-engagement vibrations. The engagement of the workpieces achieved by applying the above converged input in the microforming process is compared to that obtained by tracking a ramp transition signal in Fig. 3.7. When using the proposed approach, the overshoot was reduced by 4 times (from 6.7% to 1.6%), the settling time was reduced by over 100% (from 0.6 sec. to 0.28 sec.) with the tracking error reduced by over 3 times (from 9.43% to 2.94%), and the RMS error was reduced by 3 times (from 9.43% to 3.99%). Thus, the experimental results validated the proposed approach for achieving high-speed pre-welding engagement without inducing post-engagement vibrations.

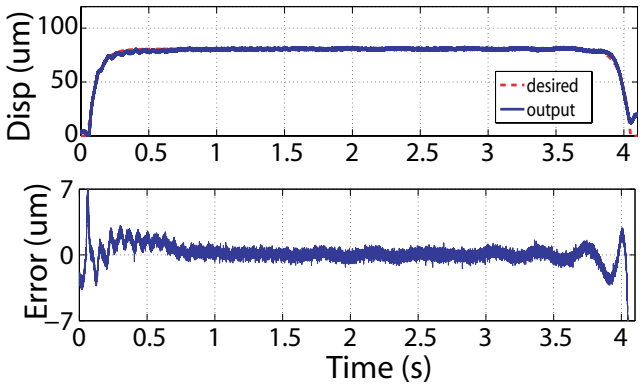

Figure 3.6: The tracking results of the desired trajectory during the pre-welding phase.

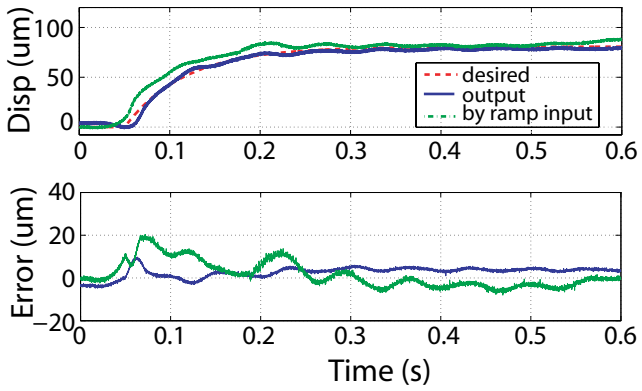

Figure 3.7: The comparison between the output displacements obtained by the desired input and by the ramp signal input during the pre-welding phase.

3.4.1 Kalman-filtering of force and displacement estimation

To design the Kalman filter to optimally estimate the horn-workpiece interaction force and the workpiece holder displacement/velocity, the following noise covariances of the force and displacement measurements were estimated based on the measured values,

$$Q_{force} = \begin{bmatrix} 0 & 0 \\ 0 & 0.75 \end{bmatrix}, \quad R_{force} = 1$$
$$Q_{disp} = \begin{bmatrix} 0 & 0 \\ 0 & 0.5 \end{bmatrix}, \quad R_{disp} = 1 \tag{3.15}$$

The measured force, displacement, and velocity signals of the large-range motion ('Measured') are compared with the estimated values by the Kalman filter ('Kalman Filter Output') in Fig. 3.8 (a), (b), and (c), respectively. Clearly, the accuracy of the estimated force, displacement and velocity of the large-range motion were substantially improved from their measured values, respectively.

Next, to identify the pre-welding to welding phase transition, the estimated force values were employed to quantify the force gradient based on the averaged value of the measured force data in every 200 ms. The estimated force drop was compared to the threshold value of 1 N (both the time period of 200 ms and the threshold of 1 N were estimated based on the preliminary work). The first time instant of over 1 N force drop was identified as the pre-welding to welding phase transition instant. Furthermore, the values of the estimated workpiece holder displacement and velocity at that time instant were registered as the boundary conditions

in the design of the optimal output transition trajectory for the pre-welding to welding phase transition below.

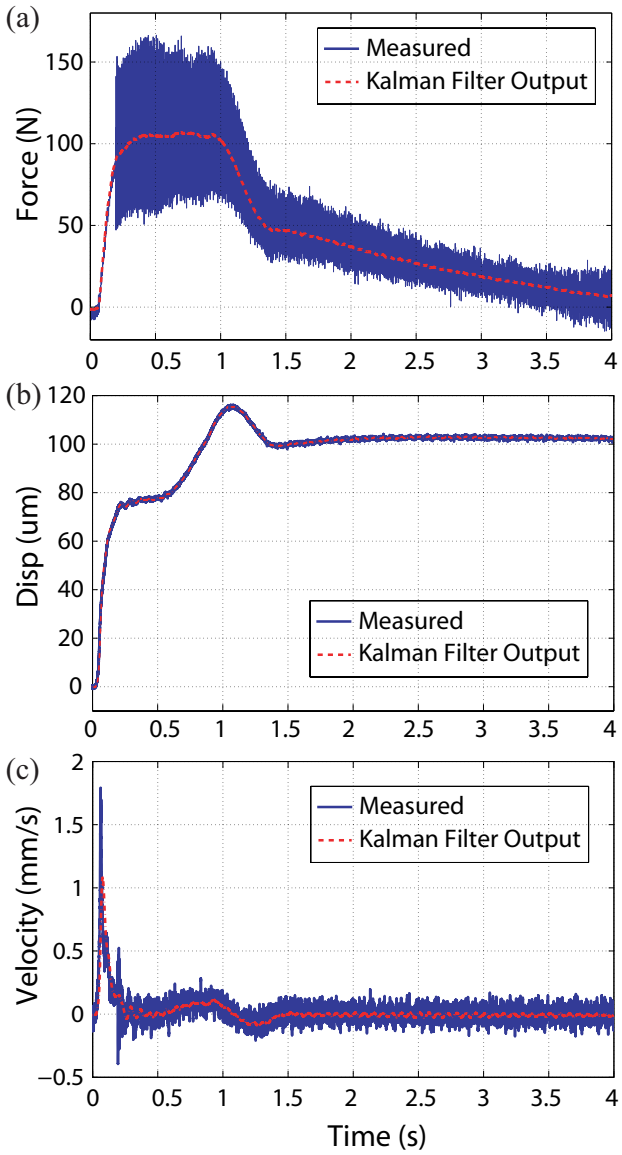

Figure 3.8: Comparison of (a) force applied to the workpieces; (b)large-range motion displacement, and (c) velocity before ('Measured') and after ('Kalman Filter Output') being passed the through Kalman filter.

3.4.2 Optimal pre-welding to welding transition

First, the desired trajectory for the pre-welding to welding phase transition was designed by using the optimal transition trajectory design for non-periodic tracking-transition switching [27].

To identify the relative degree of the system for the optimal transition trajectory design and better evaluate the performance of the entire actuation control system, the Bode plot of the closed-loop large-range motion actuation system with a PI controller was measured and fitted by using MATLAB, as shown in Fig. 3.9. The system dynamics was well approximated by a dynamics model of a relative degree of two with poles and zeros listed in Table 3.1. The DC Gain of the system was measured at 0.32.

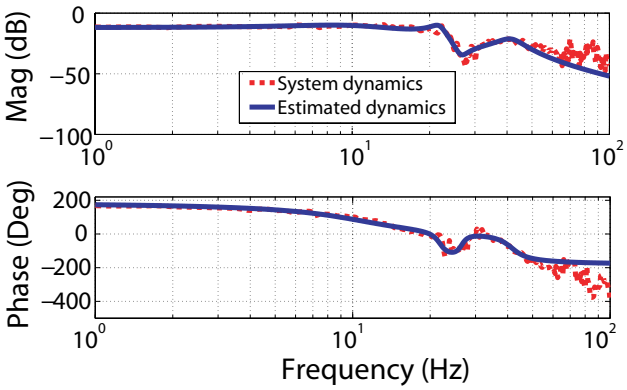

Figure 3.9: The frequency response of the closed-loop large-range actuation system.

Table 3.1: Zeros and Poles of the closed-loop unloaded large-range actuation system

Zeros	-308.79,233.68,-8.17±166.25i
Poles	-28.02±259.24i, -8.54±137i, -34.56±56.27i

Based on the measured frequency response of the closed-loop large-range actuation system, three transition times (T = 1, 0.5, 0.25 sec) were selected for simulation based on the boundary conditions obtained in experiments with $y_d(t_i) = 100.1\ um, \dot{y}_d(t_i) = 2.13\ um/sec$. The simulation results of the optimal transition trajectory during the pre-welding to welding phase transition are plotted in Fig. 3.10. It was noted that the output displacement magnitude increased as the transition time decreased. To accommodate the entire microforming duration (2 seconds) (as around 1 second was also required for the engagement of the workpieces) with moderate displacement magnitude, 0.5 seconds was selected as the transition time in the optimal output transition trajectory design in experiments.

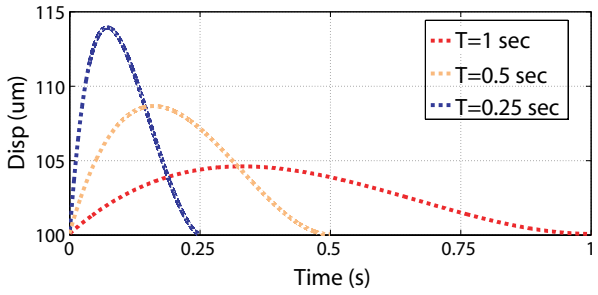

Figure 3.10: The simulated optimal transition trajectories with transition times of 1 sec, 0.5 sec, and 0.25 sec.

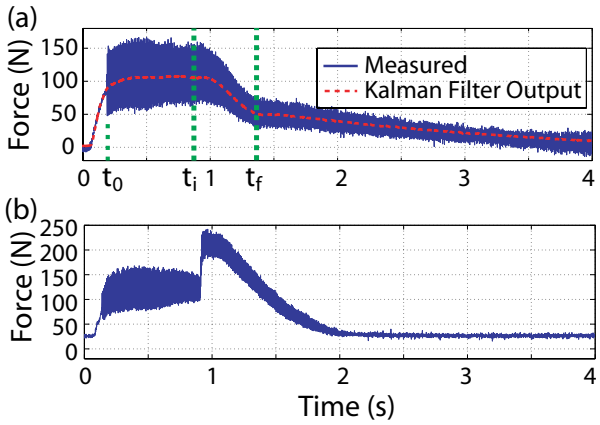

Figure 3.11: Comparison of the force obtained by implementing (a) the proposed control techniques, and (b) PI feedback control only throughout the microforming process.

3.4.3 Implementation in microforming process and welding results comparison

The proposed control framework was implemented in the microforming process to weld together two square pieces of ABS plastics each of 0.5 mm thickness. The objective was to achieve penetration depth below 150 um with a smooth and well-defined round finish surface. For comparison, a pair of the same type of workpieces were also welded by using the PI feedback control only without using the designed optimal transition trajectory during the pre-welding to the welding phase transition. The interaction force applied during the entire microforming process when using these two control methods are compared in Fig. 3.11, and the corresponding output displacement of the large-range actuation system are compared in Fig. 3.12. The image of the welded workpieces obtained by using the proposed method is also compared to those obtained by using the PI feedback control only in Fig. 3.13, respectively.

The experimental results demonstrated that the control objectives in Section 3.2 were achieved

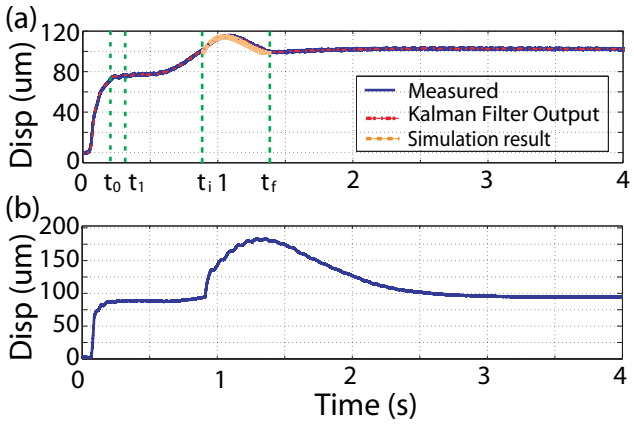

Figure 3.12: Comparison of the displacement obtained by implementing (a) the proposed control techniques, and (b) PI feedback control only throughout the microforming process.

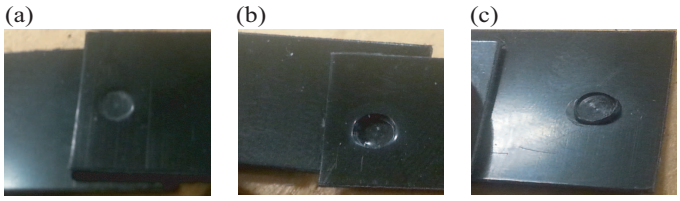

Figure 3.13: Images of the welded workpieces (a) obtained by using the proposed control framework with the desired welded quality; compared to by using PI feedback control only that resulted in (b) excessively deep penetration or (c) burrs (shown by breaking the two welded pieces apart afterwards).

by the proposed control techniques. As shown by the interaction force in Fig. 3.11 (a), the force was accurately estimated from the measured data in spite of the presence of the measurement noise and the ultrasonic vibration. The time instant of the force drop t_i was accurately identified (around 0.87 sec), and a gradual interaction force decrease was observed until the final time instant of the transition t_f (around 1.37 sec). From the output displacement of the large-range actuation system shown in Fig. 3.12 (a), it was noted that the workpieces were quickly engaged to the horn tip and settled down within the engagement time t_1 (around 0.29 sec). After the welding started at the identified transition instant t_i, the output displacement of the large-range actuation system, and thus the workpiece holder were pulled back to the welding-start position (around 100.1 um) from the time instant t_i to t_f by tracking the optimal output transition trajectory during the pre-welding to the welding phase transition. The output displacement of the large-range actuation system also well matched the optimal transition trajectory obtained by simulation, as shown in Fig. 3.12 (a). The effectiveness of the achieved control objectives

was also reflected from the image of the welded workpieces illustrated in Fig. 3.13 (a), where the desired penetration depth around 120 um was achieved. On the contrary, when only the PI feedback control was used during the pre-welding to the welding phase transition, a sharp jump was observed in the measured force during the pre-welding to welding transition (see Fig. 3.11 (b)), and correspondingly the output displacement of the large-range actuation system increased dramatically (see Fig. 3.12 (b)). Such a performance improvement of the proposed control framework was also clearly reflected by the welded workpieces obtained: As shown in Fig. 3.13 (b) and (c), the excessively large displacement output and sudden jump of the force applied resulted in an overly deep penetration and irregular burrs at the edge of the welding areas of the workpieces when using the PI feedback control alone (In Fig. 3.12 (c), the two welded pieces could easily be broken apart to show the burrs). We have been investigating in a separate study to understand the relationship between the penetration of the weld and the bond strength — a complex phenomenon of melting and bonding of polymeric chains. It was found that there exists a minimum critical penetration required for reasonable strength, as well as a peak penetration beyond which no additional strength or in some cases a weaker strength is obtained [76]. For the 0.5 mm thick ABS plastic, when the engagement force is below 90 N, the peak penetration must be constrained to be below 150 um. However, a penetration over 175 um was generated by the PI feedback control alone as in Fig. 3.12 (b). Whereas by using the proposed control technique, the penetration depth below 120 um was achieved as in Fig. 3.12 (a). The obtained welded pieces had smooth and well-defined round welding edge, and the welding depth was close to the desired value. Therefore, the experimental results clearly illustrated the proposed control framework in achieving high-speed, high-quality microforming.

3.5 CONCLUSION

Optimal high-speed microforming was achieved through the development of a control framework for the entire microforming process. By combining desired trajectory design with a recently developed iterative control technique, the workpieces were rapidly engaged without inducing post-engagment vibrations. The pre-welding to welding phase transition was quickly identified through an optimal estimation of the force drop using Kalman filtering technique. An

optimal output trajectory was designed based on the optimal output tracking-transition switching method for the pre-welding to welding phase transition. The optimal output transition trajectory was computed online and tracked by a 2DOF feedforward-feedback controller. The experimental results demonstrated the efficacy of the proposed control techniques through the comparisons of both output tracking results and with the welded workpieces obtained.

Chapter 4

Mechanical-plowing-based high-speed patterning on hard material via advanced-control and ultrasonic probe vibration

abstract

In this chapter, we present a high-speed direct pattern fabrication on hard material (e.g., a tungsten-coated quartz substrate) via mechanical plowing. Compared to other probe-based nanolithography techniques based on chemical- and/or physical- reactions (e.g., the Dip-pen technique), mechanical plowing is meritorious for its low cost, ease of process control, and wide varieties of materials beyond conductive and/or soft materials to work with. However, direct patterning on hard material faces two daunting challenges. First, the patterning throughput is ultimately hindered by the "writing" (plowing) speed, which, in turn, is limited by the adverse effects that can be excited/induced during high-speed, and/or large-range plowing, including the vibrational dynamics of the actuation system (the piezoelectric actuator, the cantilever, and the mechanical fixture connecting the cantilever to the actuator), the dynamic cross-axis coupling between different motion axes, and the hysteresis and drift effects related to the piezoelectric actuators. Secondly, it is very challenging to directly pattern in ultra-hard materials via plowing. Even with stiff probe of hardest material (diamond), the line depth of the pattern via continuous plowing on ultra-hard materials such as tungsten, is rather small (< 0.5 nm) and hardly of any practical usage, particularly when the "writing" speed becomes high. To overcome these two challenges, we propose to utilize a novel iterative learning control technique to achieve precision tracking of the desired pattern during high-speed, large-range plowing, and introduce ultrasonic vibration of the probe in the normal (vertical) direction during the plowing process to enable direct patterning in ultra hard materials. The proposed approach was implemented to directly fabricate patterns on a mask with tungsten coating and quartz substrate. The experimental results demonstrated that a large-size pattern of four grooves (20 μm in length

with 300 nm spacing between lines) can be fabricated at a high speed at ~5 mm/sec, with the line width and the line depth at ~95 nm and 2 nm, respectively. A fine pattern of the word 'NANO' is also fabricated at the speed of ~5 mm/sec. Such a high-speed direct mask patterning with nanoscale line width and depth demonstrates the potential of the proposed technique for strategic-important areas such as mask lithography in semiconductor industry.

4.1 Introduction

This chapter presents an approach to achieve high-speed direct patterning on hard materials via advanced-control and ultrasonic-vibration-assisted mechanical plowing using an atomic force microscope (AFM). As the material removing process involved in mechanical plowing is much simpler than other probe-based nanolithography (PBN) methods that rely on physical [77] and/or chemical reactions [78], mechanical plowing — compared to those PBN methods — tends to not only cost less in both equipment and operation, but also have less complexity in the process control. Moreover, those physical- and/or chemical-reaction based PBN techniques [79, 80] are mainly limited to conductive and/or soft materials, thereby cannot be employed for direct patterning on hard material. Whereas a much larger variety of materials, ranging from polymers [30] to metals [16], can be directly patterned by using mechanical plowing. Particularly, the direct patterning on hard materials finds applications in a wide range of areas including nanoelectronics [81] and nanomachining [82]. Therefore, mechanical plowing is a promising PBN technique for direct patterning on hard materials.

Challenges, however, need to be addressed to achieve high-speed patterning on hard material using mechanical plowing. One of the main challenges is to maintain precision positioning of the cantilever probe with respect to the sample surface during the patterning process at high speeds, particularly when the fabrication size becomes relatively large. Like in other PBN processes, the dynamics of the actuation system, from the piezoelectric actuators to the mechanical fixture (of the cantilever) and then to the cantilever, can be excited when the plowing is at high speeds, resulting in pattern distortions [13]. More pattern distortions can be induced when the fabrication size is increased towards the full displacement range of the piezo actuators, and the hysteresis effect of the piezo actuators becomes more pronounced [14, 15]. To address

these adverse effects in the high-speed PBN, piezo actuators with large bandwidth and/or actuators with high performance have been exploited to increase the operation speed [83, 84]. The increase of bandwidth, however, resulted in a smaller displacement (motion) range [85], and the high performance actuator is inevitably accompanied with a cost increase. Moreover, cross-axis coupling exists in positioning between different axes during 3-D PBN process, due to the misalignment (albeit small) of the piezo actuators and/or positioning sensors [16, 15]. The patterning quality (line width and/or depth) can also be adversely effected by the pattern geometry and fabrication direction, especially when the fabrication is along with or perpendicular to the longitudinal direction of the probe [86]. Therefore, it is crucial to maintain precision probe-sample positioning during the high-speed PBN process.

Further challenge in mechanical plowing arises when fabricating on hard material. Note that while physical- and/or chemical- reactions based PBN techniques [79, 80] are limited to soft materials (e.g., polymers [79]) and/or conductive materials (e.g., polyimide (PI) langmuirblodgett (LB) films [80]), and/or require significant additional instrument (e.g., laser) to be augmented to the AFM platform, mechanical plowing provides a conceptually-simple and cost-effective means to pattern a wide variety of materials, ranging from polymers [79, 30] to inorganic compounds [87] and metals like gold [16]. As the hardness of material increases, however, it becomes increasingly difficult to pattern (indent) on those materials, even with the hardest probe available (diamond probe). This difficulty might be alleviated by repeatedly plowing the same pattern [16]. The pattern quality (line width and uniformity of line depth), however, can be degraded as it is very challenging to reposition the probe exactly along the same path (with nanometer to sub-nanometer precision), particularly when plowing at high-speed and/or large range. Moreover, such an approach becomes ineffective for ultra hard materials such as tungsten or chromium. Therefore, there is a need to develop techniques to enable mechanical plowing for high-speed, large-range patterning on hard materials.

In this work, we present an approach that integrates advanced control with ultrasonic-vibration of the probe to enable mechanical plowing for high-speed patterning on hard materials. A data-driven, differential-inversion iterative control (MFDIIC) algorithm is proposed to account for both the hysteresis and the vibrational dynamics effects during the high-speed,

large range PBN process. The MFDIIC is also utilized to compensate for the cross-axis dynamics coupling in multi-axis fabrication process. Moreover, ultrasonic vibration of the probe in the normal (vertical) direction is augmented to the motion of the probe during the plowing process [30]. The normal ultrasonic-vibration of the probe substantially increases the impact (from the probe) on the sample surface, thereby enabling indentation (plowing) on hard material. The proposed approach is implemented to fabricate patterns of large size (60 um) on a tungsten coated mask (with quartz as the substrate). The experimental results showed that a plowing speed as high as ~5 mm/sec can be achieved with the patterned line width and line depth at 95 nm and 2 nm, respectively.

The proposed approach possesses unique advantages for high-speed direct patterning on hard materials. Unlike the "Dip-pen"(DPN) [78] and other reaction-based PBN techniques [88] that are limited to soft samples only (e.g., polymers), the presented technique is capable of directly fabricating patterns on hard samples (e.g., metal surface), thereby, opens the door to applications for nanopatterns and nanodevices of hard materials. For example, direct patterning on tungsten coated mask presented in this work demonstrated the feasibility of the proposed technique for mask lithography: Not only both the patterning speed and pattern quality (line width) compare well with those obtained using electronic beam (E-beam) lithography, but also the proposed technique avoids the step to generate pattern on polymer layer first as needed in the E-beam lithography [89]. Moreover, the equipment cost of AFM is only a small fraction of that of an E-beam system. We also note that ultrasonic vibration has been explored at macro- and meso- scale machining [67], and has also been recently employed in mechanical plowing PBN [30]. However, unlike the work in Ref. [5] that is limited to soft polymer and low patterning speed, the proposed approach achieves direct patterning on hard materials of Young's modulus over 130 times higher (than the polymer sample employed in Ref. [5] , 411 GPa vs 3 GPa in Ref. [5]), with "writing" speed over 200 times faster (than that reported in Ref. [5] , 5 mm/sec vs. 20 μm/sec in Ref. [5]). Therefore, the proposed technique moves the PBN technology forward towards its application in strategic important areas such as semiconductor lithography.

4.2 Ultrasonic-vibration-assisted nanolithography by mechanical plowing using AFM

4.2.1 Ultrasonic-vibration-assisted AFM-based nanolithography by mechanical plowing

In the ultrasonic-vibration-assisted nanolithography via mechanical plowing, the probe of a cantilever (with a large spring constant) is pushed against the sample surface under a static force load, while the probe is vibrating vertically under an ultrasonic vibration drive (see FIG. 4.1). The static load needs to be selected at an appropriate level so that a stable vibration of the probe on the sample surface is maintained during the plowing process.

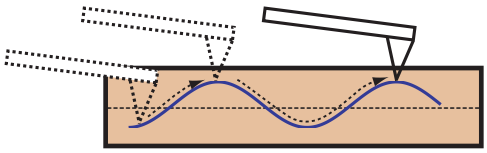

Figure 4.1: Schematic diagram of vertical ultrasonic vibration assisted lithography process.

4.2.2 Modeling-free iterative learning method for precision tracking of probe motion

Central to high-speed PBN is to achieve precision tracking in all *x*, *y*, and *z* axes simultaneously during the fabrication process. During multi-axis motion of the probe, however, the positioning accuracy of the probe relative to the sample could be distorted by the nonlinear hysteresis of the piezo actuators [13], and the vibrational dynamics of the piezo actuators and the mechanical fixture (from the cantilever to the piezo actuator) [15]. Significant dynamics variation can also be induced by effects such as the aging of the piezo actuators, and change of parts (e.g., replacement of the cantilever). Moreover, the dynamics coupling between different axes motions exists and becomes prominent when the fabrication speed increases [15]. As these adverse

effects could severely reduce the tracking precision of the piezo actuators, resulting in pattern distortion directly, they must be compensated for in high-speed, large-range probe-based nanolithography.

In this chapter, we propose a data-driven, differential-inversion iterative control (MFDIIC) approach to address the above adverse effects. The MFDIIC algorithm is given below in the frequency domain as,

$$
\begin{aligned}
&u_0(j\omega) = \alpha \times y_{des}(j\omega), && k = 0,\\
&u_1(j\omega) = \frac{u_0(j\omega)}{y_0(j\omega)} \times y_{des}(j\omega), && k = 1,\\
&u_k(j\omega) = u_{k-1}(j\omega) + \left[\frac{\rho}{\sum_{i=1}^{N} e^{-\beta i}} \sum_{i=1}^{N} e^{-\beta i} \frac{e_{u,N-i}(j\omega)}{e_{y,N-i}(j\omega)} \right] \times e_{k-1}(j\omega),\\
&\qquad\qquad \text{with} \quad N = 1, 2, \cdots, k-1, && k \geq 2,\\
&e_{k-1}(j\omega) = y_{des}(j\omega) - y_{k-1}(j\omega),\\
&e_{u,N-i}(j\omega) = u_{N-i}(j\omega) - u_{N-i-1}(j\omega),\\
&e_{y,N-i}(j\omega) = y_{k-i}(j\omega) - y_{N-i-1}(j\omega)
\end{aligned}
\tag{4.1}
$$

where '$f(j\omega)$' denotes the Fourier-transform of the signal '$f(t)$', and $y_k(\cdot)$ is the system output for the input $u_k(\cdot)$ during the k^{th} iteration. α is a pre-chosen constant (e.g., the DC-gain of the piezo-actuation system of the AFM), and $\beta \in (0,\ 1)$ and $\rho \in (0,\ 1)$ are coefficients selected to ensure the convergence of the iteration. We note that when choosing $N = 1$ and $\rho = 1$ in Eq. (5.1), the MFDIIC algorithm reduces to that proposed in Ref. [22].

The above MFDIIC improves over the modeling-free inversion-based iterative control (MFIIC) algorithm proposed in Ref. [20] by exploring the input-output (tracking) data of not only the last iteration, but the past N iterations to update/correct the control input for the current iteration (the efficacy of the MFIIC algorithm for various nanopositioning applications have been demonstrated [16, 91, 92]): Through a weighted averaging process, the non-repeated part of the input error (i.e., of random behavior) is "washed" out, while the repeated part is "integrated" and thereby, can be accounted for more efficiently. The effect of the past tracking (on the current control input) can be adjusted through the "forgetting factor" $e^{-\beta i}$, and the amplification

mechanism is further enhanced through the use of the ratio of the input and output differences. Note that the update of the control input is applied in the “tractable” frequency region, i.e., the frequency region where the frequency components of the desired output can be tracked, and the control input is set to zero at frequencies outside the “tractable” region. Although the control law can be readily applied to the tracking in *x*- and *y*-axis directions, care needs to be taken for the *z*-axis tracking as the normal ultrasonic vibration may interfere and distort the tracking (see FIG. 4.2). To avoid such an interference, the *z*-axis output (i.e., the cantilever deflection) is passed through an analog low-pass filter (LPF, see FIG. 4.3) with the cut-off frequency higher than the “tractable” frequency region but lower than those related to the ultrasonic vibration. The filtered *z*-axis output is then treated as the measured output in the MFDIIC law. Finally, a digital proportional-integral (PI) feedback controller is employed to account for the drift of cantilever probe (i.e., the deflection signal) caused by issues such as the creep of the piezo actuator (see FIG. 4.3).

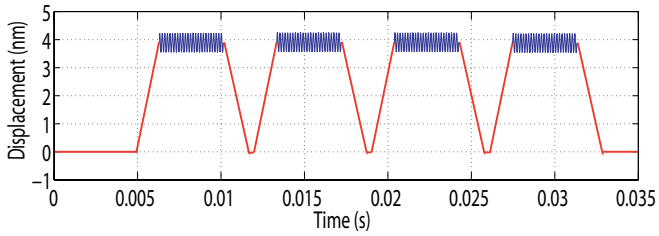

Figure 4.2: Desired deflection trajectory during mechanical plowing process.

4.2.3 Multi-axis trajectory tracking in 3D probe-based nanolithography

The dynamics coupling effect in 3D nanolithography arises from adverse effects such as the misalignment (albeit small) of the piezo actuators in different axes (see FIG. 4.4). Compensating for the cross-axis dynamics coupling is important in nanolithography [15], as the in-plane dynamics coupling (between *x*- and *y*- axes) will directly affect the precision of the pattern geometry, and the out-of-plane dynamics coupling (from *x*- and *y*- axes to *z*-axis) will affect both the line width and the line depth. Moreover, the regularity and the uniformity of the line width and depth could also be distorted by the dynamics coupling, especially when the plowing is at high speeds or high rates (relative to the resonant frequency of the piezo actuators). Therefore, the cross-axis dynamics coupling needs to be compensated for in PBN process.

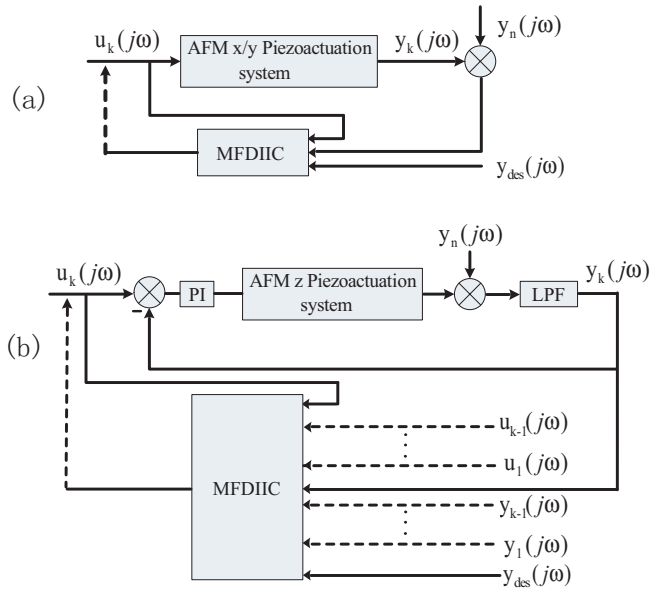

Figure 4.3: MFDIIC scheme to track the desired output trajectory in (a) *x* and *y* directions; and (b) *z* direction in the proposed nanofabrication process.

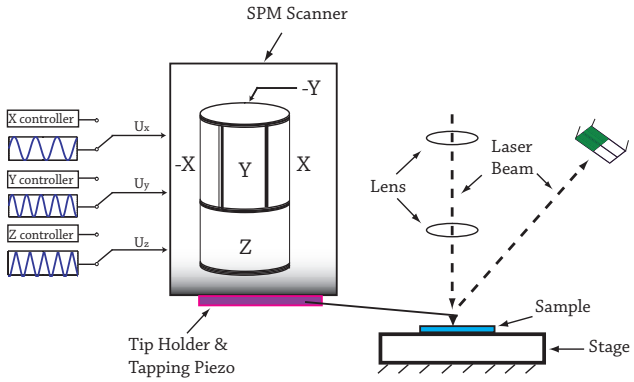

Figure 4.4: Schematic diagram of vertical ultrasonic vibration assisted lithography process.

In this chapter, the MFDIIC algorithm is utilized to compensate for the cross-axis dynamics coupling effect. The idea is to, first, identify the dynamics coupling caused output in one axis from the other two axes, e.g., output in the *i* axis caused by coupling from axes *j* and *k*, $y_{ij}(j\omega)$ and $y_{ik}(j\omega)$, and then, modify the desired trajectory of that axis, e.g., modify $y_{i,d}(j\omega)$. The coupling caused output, $y_{ij}(j\omega)$ and $y_{ik}(j\omega)$, are identified by applying the MFDIIC algorithm to axis *j* or axis *k* alone to track the desired trajectory of the respective axis separately, and the modified desired trajectory, $\hat{y}_{i,dm}$, is obtained by subtracting $y_{ij}(j\omega)$ and $y_{ik}(j\omega)$ from the original desired trajectory of axis *i*, $y_{i,d}(j\omega)$, i.e.,

$$
\begin{aligned}
y_{ij}(j\omega) &= u_{j,d}(j\omega) \times G_{ij}(j\omega) \\
y_{ik}(j\omega) &= u_{k,d}(j\omega) \times G_{ik}(j\omega) \\
\hat{y}_{i,dm}(j\omega) &= y_{i,d}(j\omega) - y_{ij}(j\omega) - y_{ik}(j\omega)
\end{aligned}
\tag{4.2}
$$

The MFDIIC algorithm is then utilized again to track the modified desired trajectory in axis i only and obtain the desired input $u_{i,d}(j\omega)$. Finally, the desired inputs of the three axes are applied simultaneously during the plowing process.

4.3 Experimental implementation: high-speed direct patterning on tungsten-coated mask

4.3.1 Experimental setup and objectives

In this work, an AFM system (Dimension Icon, Bruker) along with diamond-coated probes (DDESP-10, Bruker) was used to directly fabricate patterns on tungsten coated quartz mask (coating thickness: 5 nm). The nominal tip radius and probe height were at 35 nm and 10~15 μm, respectively, and the spring constant and the fundamental resonant frequency of the cantilever (made of antimony doped silicon) were at 42 N/m and 320 kHz. The patterns were fabricated by using the cantilever probe to directly plow on the sample under a pre-chosen static force load. Then the pattern generated was immediately imaged in contact-mode by using the same probe. All the control input signals were generated and applied by using a Matlab xPC-target package along with a data acquisition system. In addition, a 3rd-order Butterworth analog filter with cutoff frequency at 10 kHz was designed to filter the measured deflection signal. The MFDIIC algorithm was implemented for the first order case, i.e., $N = 1$ in Eq. (5.1) with $\rho = 1$ as in Ref. [22].

To evaluate and demonstrate the efficacy of the proposed approach in direct mask lithography, the patterns fabricated by using the proposed method were compared with those obtained without using control techniques and those obtained without probe ultrasonic vibration at different plowing speeds. First, a grating of four 20 μm long grooves was chosen as the desired

pattern to be fabricated on the sample, and the fabrication direction was along the *y* axis. Then, the word 'NANO' was fabricated by the same process. Three different patterning rates were tested, 2 Hz, 31 Hz and 70 Hz, where the patterning rate was defined as the reciprocal of the entire time to traverse the entire pattern once. The corresponding average speed was at ~0.15 mm/sec, ~2.5 mm/sec and ~5 mm/sec, respectively. The desired trajectories of the three axes for the groove pattern are plotted in FIG. 4.5.

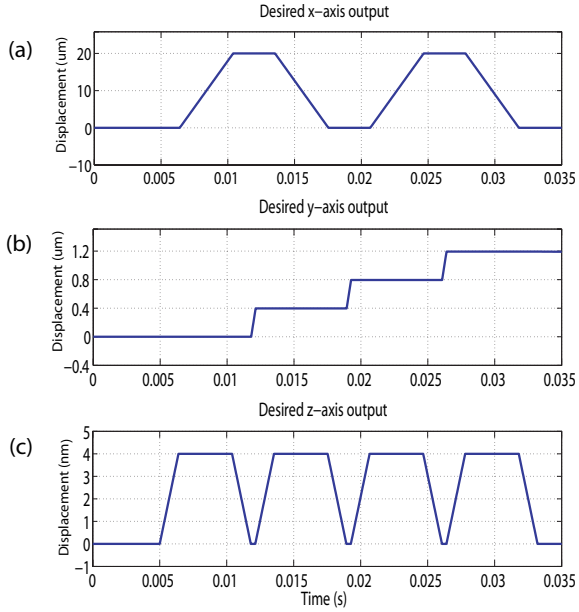

Figure 4.5: Desired motion trajectories in (a) *x* axis; (b) *y* axis; and (c) *z* axis.

4.3.2 Tracking results and discussion

To compensate for the cross-axis dynamics coupling effect, the coupling caused extraneous output displacement in the three axes were quantified by tracking the trajectory using the 1^{st}-order MFDIIC algorithm in one axis and measuring the displacements in the other two axes, shown in FIG. 4.6 for the patterning rate of 31 Hz. It was observed that among the three dynamics-couplings, the *y*-to-*x* and *y*-to-*z* dynamics-coupling were much more pronounced than that from *x* or *z* axis to the other two axes. As a result, when the trajectory in *y* axis was tracked, large coupling-caused displacement were induced in the other two axes — 25% and 33.3% of the desired *x*-axis and *z*-axis displacements, respectively. We also observed that the dynamics coupling effect from *x* axis to *z* axis was about 6% of the size of the *z*-axis

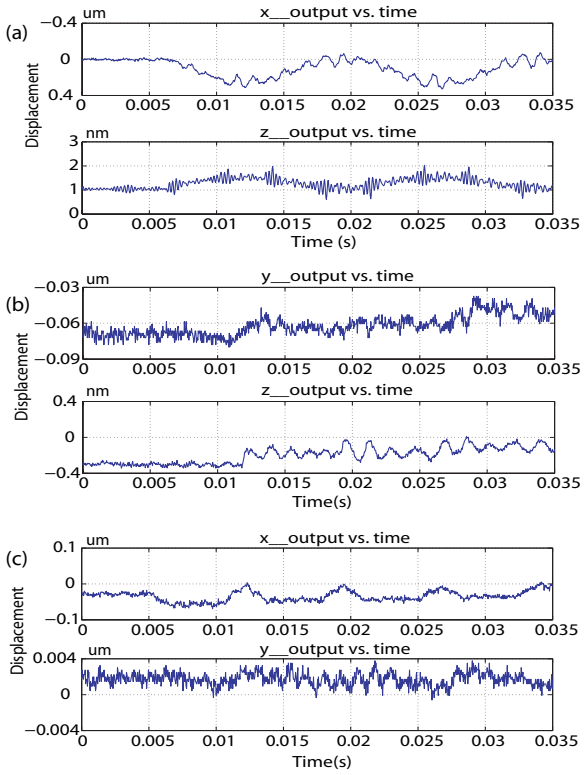

Figure 4.6: Cross-axis dynamics-coupling caused output: (a) from *y*-axis to *x* and *z* axes; (b) from *x*-axis to *y* and *z* axes; and (c) from *z*-axis to *x* and *y* axes.

desired trajectory. Hence, the *y*-to-*x*, *y*-to-*z*, and *x*-to-*z* dynamics-coupling effects needed to be compensated for in this experiment.

The *y*-to-*x* coupling effect was compensated for by measuring the coupled output in *x* and *z* axes when precision tracking in the *y*-axis was achieved (the 2-norm tracking error was below 5%) by using the 1^{st}-order MFDIIC algorithm, and tracking the modified desired trajectory in both *x* axis and *z* axis, respectively. The *x*-to-*z* and *y*-to-*z* coupling effects were accounted for similarly with the *z*-axis modified desired trajectory obtained by subtracting the measured *x*-to-*z* and *y*-to-*z* coupling outputs from the original *z*-axis desired trajectory. In order to reduce the measurement noise effect, the (modified) desired trajectory was duplicated five times and tracked during the iteration process. The output measured in each iteration was then averaged over the five periods, and the averaged output of one period was used in the MFDIIC algorithm to obtain the input for the next iteration. This duplication-averaging process substantially reduced the effect caused by the repeatable part of the disturbances like noise [91].

The tracking results shown in FIG. 4.7 demonstrate the efficacy of the proposed MFDIIC

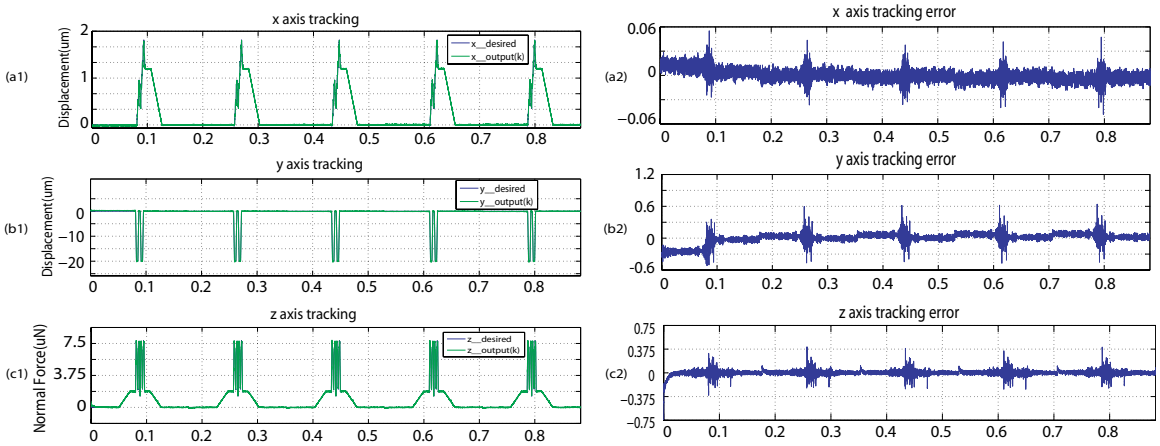

Figure 4.7: The tracking results and errors of the trajectories along (a1)(a2) *x* axis; (b1)(b2) *y* axis; and (c1)(c2) *z* axis by compensating for the cross-axis dynamics-coupling effect when the overall line speed of the plowing is 5 mm/sec.

algorithm in achieving precision positioning of the AFM probe in all three axes. The iteration was terminated when the relative RMS error could not be reduced further [91]. At the patterning rate of 70 Hz, the relative RMS error, E_{RMS}(%), was only at 1.74% in the patterning axis (*y*-axis). Such a precision tracking also demonstrated that the dynamics coupling caused output was effectively removed. As shown in FIG. 4.7(b)(c), the E_{RMS}(%) of *x* axis tracking reached 0.11%; and that in *z* axis was only 2.12% even when ultrasonic vibration was also applied. Therefore, the hysteresis effect, the vibrational dynamics effect, and the dynamics-coupling effect were all compensated for. The input signals obtained through this method were applied along with vertical ultrasonic vibration of the probe during the plowing pattern fabrication process.

4.3.3 Nanolithography results and discussion

The three sets of groove patterns fabricated by using the MFDIIC method (with no normal ultrasonic vibration applied), the DC-gain method (with normal ultrasonic vibration applied, where the control input for each axis was generated by scaling the corresponding desired trajectory with the DC-gain of that axis), and the proposed method are shown in FIG. 4.8 to FIG. 4.9, respectively. The normal ultrasonic vibration frequency was set to the 2^{nd} resonant frequency of the cantilever (1.7 MHz) with a free vibration amplitude of 30 nm. The 1^{st} resonant frequency was not chosen as the vibration amplitude (above 170 nm) of the probe at the 1^{st} resonance

was exceedingly large and can quickly lead to tip wear, while the vibration amplitudes at other higher resonant frequencies became too small and insufficient.

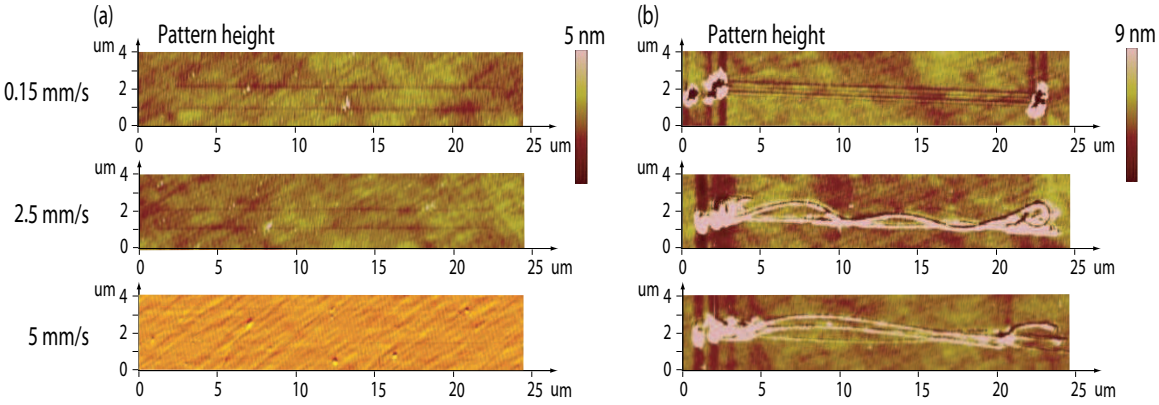

Figure 4.8: Images of the groove patterns fabricated at different speeds (a) by using the MFDIIC algorithm without applying ultrasonic vibration; (b) by using the DC-gain method with applying ultrasonic vibration.

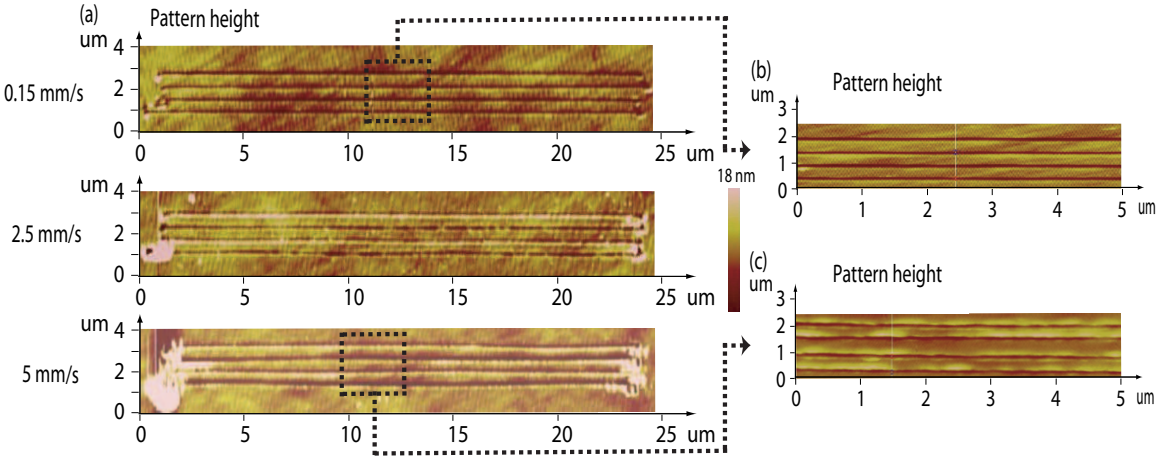

Figure 4.9: (a)Images of the groove patterns fabricated at different speeds by using the MFDIIC technique with applying ultrasonic vibration; (b) the zoomed-in image of the portion of the pattern fabricated at 5mm/sec in (a); (c) the section profile of the grooves along the white line in (b).

The comparison of the groove patterns fabricated by using the above three methods demonstrates the efficacy of the proposed approach for high-speed direct patterning on hard material via mechanical plowing. First, as shown in FIG. 4.8(a), precision tracking of the desired pattern can be achieved by using the MFDIIC algorithm during the plowing process, even when the plowing speed was as high as 5 mm/sec. The line depth and width (particularly the depth), however, reduced and became barely visible in the AFM image at patterning speed of 5 mm/sec

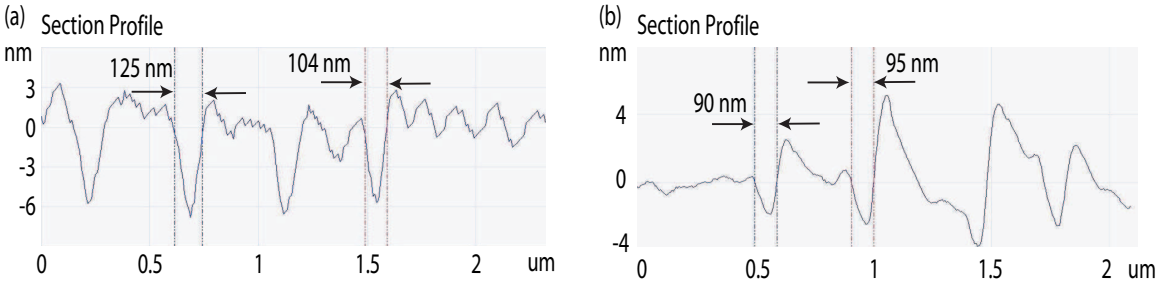

Figure 4.10: Section profile corresponding to (a) image in 4.9(b) ; (b) image in 4.9(c).

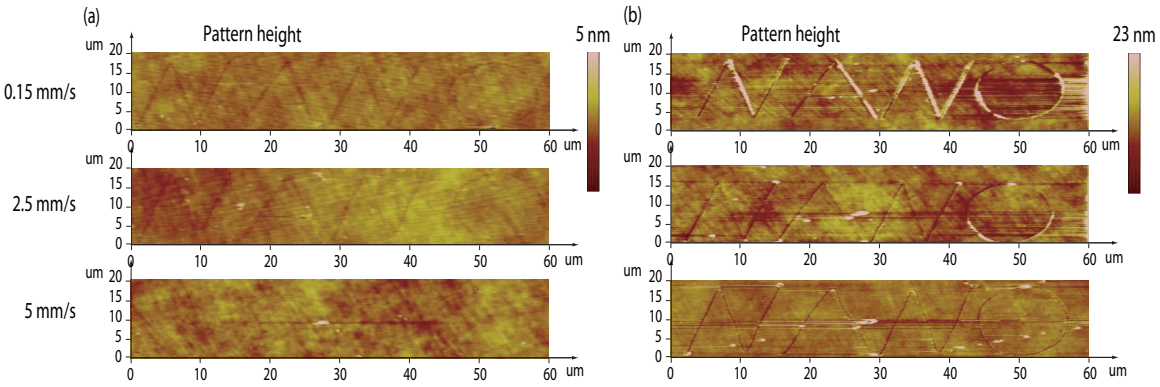

Figure 4.11: Images of the word 'NANO' fabricated at different speeds by using the MFDIIC technique (a) without applying ultrasonic vibration; (b) with applying ultrasonic vibration.

(the line depth at 5 mm/sec was only 0.5 nm). We also note that for all three plowing speeds, two of the four grooves were much deeper (i.e., more visible) in the pattern images. Such a difference might be due to the geometry difference between the contact angle/area of the probe and the bending of the cantilever [86]. As the Young's modulus of the tungsten coating at ~411 GPa was comparable to that of the diamond-coated probe (Young's modulus of diamond: 1220 GPa), the shallow-line pattern image in FIG. 4.8(a) also underscored the difficulty in direct patterning on hard material via mechanical plowing. This difficulty can be alleviated by applying ultrasonic vibration of the probe during the plowing process, as demonstrated in the patterns obtained by using the DC-gain method in FIG. 4.8(b). With the augmentation of vertical ultrasonic vibration of the probe, both the line depth and uniformity of the pattern were substantially improved (the line depth was increased from 0.5 nm to 1.5 nm at the patterning speed of 5 mm/sec). Particularly, with a large enough ultrasonic vibration amplitude (7.5 μN), all four grooves were fabricated. The line uniformity can be further improved by increasing the ultrasonic vibration amplitude. However, it was also evident that the patterns were severely

distorted when using the DC-gain method — the skewed patterns at speed of 0.15 mm/sec were caused by the drift of the piezo actuators due to the long fabrication time (0.53 sec), while the vibrational, hysteresis, and cross-axis coupling effects led to pattern distortions at higher plowing speeds. Thus, the experimental results demonstrated the needs for both control techniques and ultrasonic probe vibration in high-speed direct fabrication in hard metal through mechanical plowing.

The following experimental results demonstrated that the proposed approach, by combining advanced contorl with ultrasonic vibration of the probe, substantially improved the fabrication quality in both line depth and uniformity during high-speed direct plowing in hard metal. The cross section profile in FIG. 4.10(b) shows that the line width of about 95 nm was achieved with the spacing of 300 nm between two adjacent grooves at the patterning rate of 70 Hz (the corresponding average plowing speed: 5 mm/sec) with ultrasonic vibration amplitude increased to around 11 μN. By increasing the ultrasonic vibration force amplitude to 11 μN, not only the line depth was increased to over 2 nm, but the uniformity of the pattern fabricated was also substantially improved as the line depth difference between different grooves were substantially reduced (compare FIG. 4.9(a) to that in FIG. 4.8). Such an improvement was achieved as the ultrasonic vibration force dominated over the static force load applied to the cantilever probe during the plowing process. We also notice that a significant amount of debris was accumulated around the beginning and the end areas of the groove patterns obtained by both the DC-gain method and the proposed method (See Figs. 4.8 and 4.9). These debris were generated as the ultrasonic vibration was applied at the same amplitude throughout the entire fabrication process, even when the probe was not in contact with the sample. As a result, debris accumulated at the beginning and end areas of the grooves when the probe approached or withdrew from the sample gradually by following a ramp signal of low rate (to avoid sudden impact or detach from the sample in order to protect the probe), thereby spending more time around these two areas. Such a debris accumulation can be largely avoided by controlling the augmentation of the probe vibration, for example, by applying the probe vibration only when the probe-sample interaction force reached the given level under the preload, and gradually increasing the amplitude of the vibration (Such a scheme was not implemented in this experiment due to hardware limit).

By implementing the same technique, a set of words of ‘NANO’ were also fabricated on the same tungsten-quartz sample with or without the normal probe ultrasonic vibration being applied, as shown in FIG. 4.11. Both the pattern accuracy and the line depth were also achieved at a high plowing speed of 5 mm/sec. The patterning speed in the mm/sec range achieved in this work is among the fastest direct lithography on hard material with nanoscale resolution (feature size around 100 nm) ever reported. Therefore, the experimental results demonstrated the capability of the proposed approach to achieve high-speed direct lithography of nanoscale patterns on hard material.

4.4 Conclusions

In this chapter, an approach that combined advanced control with probe ultrasonic vibration to achieve high-speed, large-range nanolithography on hard material via mechanical plowing is proposed. The adverse hardware effects on hgih-speed, large-range nanolithography of hard materials, including the hysteresis, the vibrational dynamics and the cross-axis dynamics coupling effects, have been compensated for by the proposed MFDIIC technique. Normal ultrasonic vibration has been introduced to enable direct pattern on hard material and improve the pattern quality. The proposed approach was implemented to fabricate a grating of four grooves and the word ‘NANO’ on a tungsten-coated mask sample. High-speed lithography at 5 mm/sec with line width of 95 nm and line depth of ~2 nm has been achieved.

Chapter 5

A modeling-free differential-inversion-based iterative control approach to simultaneous hysteresis-dynamics compensation: high-speed large-range motion tracking example

abstract

In this chapter, a data-driven modeling-free differential-inversion-based iterative control (MFDIIC) method is proposed to compensate for both nonlinear hysteresis and dynamics of hysteresis-like hammerstein systems. Compensation for both hysteresis and dynamics is needed in the control of hammerstein systems such as smart actuators, where these two effects coexist and become pronounced in high-speed, large-range output tracking, resulting in large tracking errors. Simultaneous hysteresis and dynamics compensation, however, is challenging as hysteresis modeling, as needed in many existing control methods, is rather complicated and prone to errors and uncertainties. The hysteresis and dynamics not only are coupled in affecting the output tracking, but also tend to change due to the variations of the system conditions (e.g., the age of smart actuators). The proposed MFDIIC technique aims to compensate for both of these effects with no needs for modeling hysteresis and/or dynamics, and achieve both precision tracking and good robustness against hysteresis/dynamics changes. The convergence of the MFDIIC algorithm is analyzed with random output disturbance/noise considered. It is shown that precision tracking can be achieved with the tracking error close to the noise level in the statistical sense. The proposed MFDIIC method is demonstrated through implementation on high-speed large-range output tracking of two different types of smart actuators with symmetric and asymmetric hysteresis behavior, respectively.

5.1 Introduction

Compensation for both hysteresis and dynamics is important in the control of smart actuators made of, for example, ferromagnetic material, ferroelectric material, and shape memory alloy, which are widely used in applications including nanopositioning [93, 94], nanofabrication/microforming [17, 67] systems, robotic manipulators [95] and chemical reactor [96]. The presence of both dynamics and nonlinear hysteresis effect imposes control challenges when these actuators are implemented in tracking/positioning applications, particularly, during high-speed large-range motions [97, 98]. In this chapter, we present the development of a data-driven, modeling-free differential-inversion-based iterative control (MFDIIC) approach to achieve simultaneous hysteresis and vibrational dynamics compensation without modeling the hysteresis and/or the vibrational dynamics, but with precision tracking and good robustness against hysteresis/dynamics changes instead.

Control of smart actuators towards simultaneous hysteresis and dynamics compensation has attracted great efforts due to the challenges involved and the needs for precision positioning and motion control in a wide variety of applications. For example, phenomenological models, including the widely used Preisach model [99] and the Bouc-Wen model[100], have been utilized to develop adaptive control-based [101], inversion-based [102, 103], and robust-control-based [104] approaches to the control of smart actuators. However, modeling of hysteresis can be involved and prone to errors, the controller design and implementation of these approaches can be complicated and require demanding online computation, and account for system uncertainty caused by hysteresis/dynamics changes may not be ideal and result in tracking performance trade-off. The performance-robustness trade-off can be largely mitigated via the iterative learning control (ILC) based approaches, as the hysteresis/dynamics changes of smart actuators tend to be quasi-static (i.e., the behavior of the actuator remains unchanged during the operation, but can change significantly between operations due to, e.g., change of the system condition), thereby, can be effectively compensated for via iterations (e.g., a few iterations to update the input right before the operation). These ILC techniques, however, are mainly focused on hysteresis compensation in quasi-static applications–the vibrational dynamics effect (or the so-called rate-dependent hysteresis) is not adequately addressed. Compensation for both

hysteresis and vibrational dynamics can be addressed via the inversion-based iterative control (IIC) technique [13, 105], where hysteresis modeling is avoided by considering the hysteresis effect as the perturbation to the vibrational dynamics and quantifying the changes involved. Quantifying the vibrational dynamics and its changes due to hysteresis effect has been further alleviated through the recently developed modeling free inversion-based feedforward control approach [91], whereas the mechanism of the hysteresis compensation is yet to be clarified. These progress in control of smart actuators and the remaining challenges motivate the development of the proposed approach.

The data-driven control scheme developed in this work aims to achieve precision output tracking with good robustness against hysteresis/dynamics changes, while avoiding the arduous hysteresis and vibrational dynamics modeling. The contribution of this chapter is the development of the MFDIIC technique to compensate for both the dynamics effect and the rate-independent symmetric or asymmetric hysteresis. The MFDIIC improves over the modeling-free inversion-based iterative control (MFIIC) algorithm [20] by exploring the input-output (tracking) data of not only the last iteration, but also the past iterations to update/correct the control input for the current iteration. Furthermore, the convergence of the MFDIIC in compensating for the hysteresis effect is analyzed by considering the system a hammerstein system (see Fig. 5.1) in the frequency domain. The output tracking error can be quantified in a statistical sense by the properties of the random output disturbance/noise considered in the analysis. The theoretical analysis is also validated through experimental results with two different system setups to demonstrate the competence of the proposed MFDIIC method in compensating for both the system dynamics and hysteresis effect simultaneously.

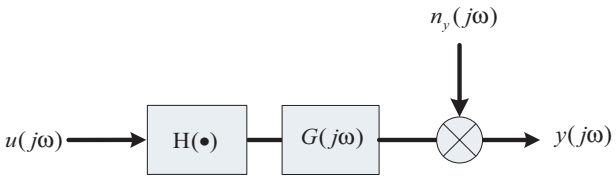

Figure 5.1: The hammerstein system.

5.2 Data-driven modeling-free difference-inversion-based iterative-control

The modeling-free differential-inversion-based iterative-control (MFDIIC) algorithm is formulated in frequency domain as,

$$\begin{aligned}
u_0(j\omega) &= \alpha \times y_d(j\omega), && k=0,\\
u_1(j\omega) &= \tfrac{u_0(j\omega)}{y_0(j\omega)} \times y_d(j\omega), && k=1,\\
u_k(j\omega) &= u_{k-1}(j\omega) + \left(\sum_{i=1}^{N} \hat{\beta}_{k,k-i} \tfrac{I_{u,k-i}(j\omega)}{I_{y,k-i}(j\omega)}\right) \times e_{k-1}(j\omega),\\
&\qquad \text{with} \quad N = 1, 2, \cdots, k-1, && k \geq 2,\\
e_k(j\omega) &= y_d(j\omega) - y_k(j\omega),\\
I_{u,k}(j\omega) &= u_k(j\omega) - u_{k-1}(j\omega),\\
I_{y,k}(j\omega) &= y_k(j\omega) - y_{k-1}(j\omega),\\
\hat{\beta}_{k,i} &= \rho \tfrac{\beta_{k,k-i}}{\mathbf{S}_\beta}, \quad \mathbf{S}_\beta = \sum_{i=1}^{N} \beta_{k,i}
\end{aligned} \tag{5.1}$$

where '$f(j\omega)$' denotes the Fourier-transform of the signal '$f(t)$', $y_k(\cdot)$ is the output for the input $u_k(\cdot)$ during the k^{th} iteration, $y_d(j\omega)$ is the desired output, α is a pre-chosen constant (e.g., the DC-gain of the system), $\hat{\beta}_{k,i}$ are the normalized weighting factors, and $\rho \in (0,\ 1)$ is the coefficient selected to ensure the convergence of the iteration, respectively.

Next we consider the proposed MFDIIC algorithm for the control of hysteresis-like hammerstein systems such as smart actuators, i.e., the input-output behavior of the system can be modeled as a static hysteresis operator followed by a linear time invariant dynamics model. For those systems the output, in the presence of random output disturbance, is given by

$$y(j\omega) = y_s(j\omega) + y_n(j\omega) = \mathbb{G}(\mathscr{H}[u(j\omega)])(j\omega) + y_n(j\omega), \tag{5.2}$$

where $\mathscr{H}[u(j\omega)]$ is the output of the nonlinear subsystem of $\mathscr{H}(\cdot)$ capturing the hysteresis characteristics. As the hysteresis effect is rate-independent but range-dependent instead, the input-output mapping (viewed in the frequency domain) becomes input dependent. Thus, the hysteresis effect can be quantified in frequency domain as the changes to the frequency response of the linear dynamics part (i.e., the ratio of the Fourier transform of the output w.r.t. the input). Specifically the ratio of the frequency responses between any two iterations, $\delta V_{i,j}(j\omega)$, is defined as

$$\delta \mathbb{V}_{i,j}(j\omega) = \frac{\mathbb{G}_i(j\omega)}{\mathbb{G}_j(j\omega)}, \text{with } \mathbb{G}_k(j\omega) \triangleq y_{s,k}(j\omega)/u_{s,k}(j\omega) \tag{5.3}$$

where $\mathbb{G}_k(j\omega)$ denotes the I/O frequency response in the k^{th} iteration, with $y_{s,k}(j\omega)$ the part of the output generated by the control input $u_{s,k}(j\omega)$ in the k^{th} iteration. We further define the difference of the I/O frequency response in two successive iterative trials, $\delta\mathbb{G}_k(j\omega)$, as

$$\delta\mathbb{G}_k(j\omega) = \mathbb{G}_k(j\omega) - \mathbb{G}_{k-1}(j\omega). \tag{5.4}$$

The next Assumption quantifies the allowed phase and amplitude variation caused by the hysteresis to the system frequency response in the proposed MFDIIC algorithm.

Assumption 1 *At any given frequency ω at which the MFDIIC law is applied, we assume*

$$\begin{aligned}
&0 < \gamma_1 \le \left|\delta\mathbb{V}_{i,j}(j\omega)\right| \le \gamma_2,\\
&0 \le \delta\theta = \angle\delta\mathbb{V}_{i,j} < \cos^{-1}\tfrac{(\gamma_1+\gamma_2-\gamma_1\gamma_2-1)(\gamma_1+\gamma_2)}{(\gamma_1+\gamma_2-1)\gamma_2^2} < \pi/2,\\
&\textit{with } \gamma_1 < 1 < \gamma_2,\ \gamma_2 - \gamma_1 < 1,\\
&|\delta\mathbb{G}_i u_{i-1}| \le \eta, \qquad\qquad \textit{for i=1, 2, 3, } \cdots, k
\end{aligned} \tag{5.5}$$

and the mapping between the system input and output satisfies the following condition,

$$\alpha_1|u_i - u_j| \le |y_i - y_j| \le \alpha_2|u_i - u_j|, \quad \alpha_2 > \alpha_1 > 0 \tag{5.6}$$

Assumption 2 *During the entire control course, the disturbance $y_{n,k}(j\omega)$ is a zero-mean Gaussian process with a standard deviation of σ_0,*

$$\mathbf{E}(y_{n,k}(j\omega)) = 0, \quad \sigma(y_{n,k}(j\omega)) = \delta_0 \tag{5.7}$$

5.2.1 Analysis of the first-order MFDIIC algorithm for hysteresis-dynamics compensation

First we consider the convergence analysis of the MFDIIC algorithm upon hysteresis-dynamics combined effects for the first order case, i.e., N = 1 in Eq. (5.1). At N=1, the MFDIIC law in Eq. (5.1) is reduced to

$$u_k(j\omega) = u_{k-1}(j\omega) + \rho\frac{I_{u,k-1}(j\omega)}{I_{y,k-1}(j\omega)} \times e_{k-1}(j\omega), k \ge 2 \tag{5.8}$$

where the initial choice of $u_0(\cdot)$ and $u_1(\cdot)$ are given in Eq. (5.1) [90].

Lemma 1 *At the k^{th} ($k \geq 2$) iteration, the tracking error of the first-order MFDIIC algorithm satisfies,*

$$e_k(j\omega) = \mathbb{C}_k(j\omega)e_{k-1}(j\omega) - \delta\mathbb{G}_k(j\omega)u_{k-1}(j\omega) - \delta n_{y,k-1}(j\omega), \tag{5.9}$$

where

$$\begin{aligned}
\mathbb{C}_k(j\omega) &= 1 - \mathbb{D}_k(j\omega) \\
\mathbb{D}_k(j\omega) &= \frac{\rho}{\delta\mathbb{V}_{k-1,k}(j\omega)+\mathbb{P}_k(j\omega)+\delta\mathbb{V}_{1,k}(j\omega)\rho^{-(k-2)}\mathbb{Q}_{k-1,k}(j\omega)} \\
\mathbb{P}_k(j\omega) &= \sum_{i=1}^{k-2}\left[\delta\mathbb{V}_{k-i-1,k}(j\omega)\rho^{-i}\mathbb{Q}_{i,k}(j\omega)\right] \\
\mathbb{Q}_{l,k}(j\omega) &= \prod_{i=1}^{l}\mathbb{R}_{k-i-1}(j\omega) \\
\mathbb{R}_k(j\omega) &= \begin{cases} \frac{\delta\mathbb{G}_1(j\omega)u_0(j\omega)+\delta n_{y,0}(j\omega)}{\mathbb{G}_1(j\omega)I_{u,1}}(j\omega), & k = 0, \\ \frac{\delta\mathbb{G}_{k+1}(j\omega)u_k(j\omega)+\delta n_{y,k}(j\omega)}{e_k}(j\omega), & k \geq 1 \end{cases} \\
\delta n_{y,k}(j\omega) &= y_{k+1,n}(j\omega) - y_{n,k}(j\omega), \qquad k \geq 0
\end{aligned} \tag{5.10}$$

and $\delta\mathbb{V}_{i,j}(j\omega)$ and $\delta\mathbb{G}_k$ are defined in Eqs. (5.3) and (5.4), respectively.

Proof 1 *We show the above recursive formula by induction. First, note that by Eq. (5.8), for N=1, we have*

$$\begin{aligned}
e_k &= y_d - \mathbb{G}_k u_k - y_{n,k} \\
&= y_d - \mathbb{G}_k\left(u_{k-1} + \rho\frac{I_{u,k-1}}{I_{y,k-1}}e_{k-1}\right) - y_{n,k} \\
&= y_d - \mathbb{G}_k u_{k-1} + \mathbb{G}_{k-1}u_{k-1} - \mathbb{G}_{k-1}u_{k-1} - \mathbb{G}_k\rho\frac{I_{u,k-1}}{I_{y,k-1}}e_{k-1} - y_{k-1,n} + y_{k-1,n} - y_{n,k} \\
&= (y_d - y_{k-1}) - (\mathbb{G}_k - \mathbb{G}_{k-1})u_{k-1}\mathbb{G}_k\rho\frac{I_{u,k-1}}{I_{y,k-1}}e_{k-1} - \delta n_{y,k-1} \\
&= \left(1 - \mathbb{G}_k\rho\frac{I_{u,k-1}}{I_{y,k-1}}\right)e_{k-1} - \delta\mathbb{G}_k u_{k-1} - \delta n_{y,k-1} \\
&= \left(1 - \frac{\mathbb{G}_k\rho I_{u,k-1}}{\mathbb{G}_{k-1}I_{u,k-1} + \delta\mathbb{G}_{k-1}u_{k-2} + \delta n_{y,k-2}}\right)e_{k-1} - \delta\mathbb{G}_k u_{k-1} - \delta n_{y,k-1} \\
&= \left(1 - \frac{\rho}{\frac{\mathbb{G}_{k-1}}{\mathbb{G}_k} + \frac{\delta\mathbb{G}_{k-1}u_{k-2}+\delta n_{y,k-2}}{\mathbb{G}_k I_{u,k-1}}}\right)e_{k-1} - \delta\mathbb{G}_k u_{k-1} - \delta n_{y,k-1}
\end{aligned} \tag{5.11}$$

Thus, the formula (5.9) can be verified for $k = 2$ by rewriting the above Eq. (5.11) using the definitions of $\delta\mathbb{V}_{i,j}$, $\mathbb{Q}_{l,k}$, and then $\mathbb{C}_k$ and $\mathbb{D}_k$ (given by Eq. (5.10)) for $k = 2$.

Secondly, we assume that (5.10) holds at the kth iteration, then at the $(k+1)^{th}$ *iteration, by Eq. (5.8),*

$$\mathbb{G}_{k+1} I_{u,k} = \mathbb{G}_{k+1} \rho \frac{I_{u,k-1}}{I_{y,k-1}} e_{k-1} \tag{5.12}$$

As the recursive formula holds at the k^{th} *iteration,*

$$\begin{aligned} e_k &= \mathbb{C}_k e_{k-1} - \delta \mathbb{G}_k u_{k-1} - \delta n_{y,k-1} \\ &= \left(1 - \mathbb{G}_k \rho \tfrac{I_{u,k-1}}{I_{y,k-1}}\right) e_{k-1} - \delta \mathbb{G}_k u_{k-1} - \delta n_{y,k-1}, \end{aligned} \tag{5.13}$$

with $\mathbb{C}_k = 1 - \mathbb{D}_k$*, and* $\mathbb{C}_k$ *and* $\mathbb{D}_k$ *satisfying the formula of Eq. (5.10). Combining Eq. (5.12) with Eq. (5.13) yields*

$$\mathbb{G}_{k+1} I_{u,k} = \frac{\mathbb{G}_{k+1}}{\mathbb{G}_k}(1 - \mathbb{C}_k) e_{k-1} = \frac{\mathbb{G}_{k+1}}{\mathbb{G}_k} \mathbb{D}_k e_{k-1} \tag{5.14}$$

and then Eq. (5.11) (for the $(k+1)^{th}$ *step) can be rewritten via Eq. (5.14),*

$$\begin{aligned} e_{k+1} &= \left(1 - \frac{\rho}{\frac{\mathbb{G}_k}{\mathbb{G}_{k+1}} + \frac{\delta \mathbb{G}_k u_{k-1} + \delta n_{y,k-1}}{\frac{\mathbb{G}_{k+1}}{\mathbb{G}_k} \mathbb{D}_k e_{k-1}}}\right) e_k - \delta \mathbb{G}_{k+1} u_k - \delta n_{y,k} \\ &= \left(1 - \frac{\rho}{\frac{\mathbb{G}_k}{\mathbb{G}_{k+1}} + \frac{\mathbb{G}_k \mathbb{R}_{k-1}}{\mathbb{G}_{k+1} \mathbb{D}_k}}\right) e_k - \delta \mathbb{G}_{k+1} u_k - \delta n_{y,k} \\ &= \left(1 - \frac{\rho}{\delta \mathbb{V}_{k,k+1} + \frac{\delta \mathbb{V}_{k,k+1} \mathbb{R}_{k-1}}{\mathbb{D}_k}}\right) e_k - \delta \mathbb{G}_{k+1} u_k - \delta n_{y,k} \end{aligned} \tag{5.15}$$

where

$$
\begin{aligned}
\frac{\delta\mathbb{V}_{k,k+1}\mathbb{R}_{k-1}}{\mathbb{D}_k} &= \frac{\mathbb{G}_k\left[\delta\mathbb{V}_{k-1,k}+\mathbb{P}_k+\delta\mathbb{V}_{1,k}(j\omega)\rho^{-(k-2)}\mathbb{Q}_{k-1,k}\right]\mathbb{R}_{k-1}}{\mathbb{G}_{k+1}\rho} \\
&= \frac{\mathbb{G}_k\mathbb{R}_{k-1}\left[\frac{\mathbb{G}_{k-1}}{\mathbb{G}_k}+\sum_{i=1}^{k-2}\left(\delta\mathbb{V}_{k-i-1,k}\rho^{-i}\mathbb{Q}_{i,k}\right)+\frac{\mathbb{G}_1}{\mathbb{G}_k}\rho^{-(k-2)}\prod_{i=1}^{k-1}\mathbb{R}_{k-i-1}\right]}{\rho\mathbb{G}_{k+1}} \\
&= \rho^{-1}\mathbb{R}_{k-1}\frac{\mathbb{G}_{k-1}}{\mathbb{G}_{k+1}}+\rho^{-1}\mathbb{R}_{k-1}\frac{\mathbb{G}_k}{\mathbb{G}_{k+1}}\sum_{i=1}^{k-2}\frac{\mathbb{G}_{k-i-1}}{\mathbb{G}_k}\rho^{-i}\prod_{j=1}^{i}\mathbb{R}_{k-j-1} \\
&\quad+\frac{\mathbb{G}_1}{\mathbb{G}_{k+1}}\rho^{-(k-1)}\mathbb{R}_{k-1}\prod_{i=1}^{k-1}\mathbb{R}_{k-i-1} \\
&= \rho^{-1}\mathbb{R}_{k-1}\frac{\mathbb{G}_{k-1}}{\mathbb{G}_{k+1}}+\sum_{i=1}^{k-2}\left[\frac{\mathbb{G}_{k-i-1}}{\mathbb{G}_{k+1}}\rho^{-(i+1)}\mathbb{R}_{k-1}\prod_{j=1}^{i}\mathbb{R}_{k-j-1}\right]+\frac{\mathbb{G}_1}{\mathbb{G}_{k+1}}\rho^{-(k-1)}\mathbb{R}_{k-1}\prod_{i=1}^{k-1}\mathbb{R}_{k-i-1} \\
&= \rho^{-1}\mathbb{R}_{k-1}\frac{\mathbb{G}_{k-1}}{\mathbb{G}_{k+1}}+\sum_{i=1}^{k-2}\left(\frac{\mathbb{G}_{k-i-1}}{\mathbb{G}_{k+1}}\rho^{-(i+1)}\prod_{j=1}^{i+1}\mathbb{R}_{k-j}\right)+\frac{\mathbb{G}_1}{\mathbb{G}_{k+1}}\rho^{-(k-1)}\prod_{i=1}^{k}\mathbb{R}_{k-i} \\
&= \rho^{-1}\mathbb{R}_{k-1}\frac{\mathbb{G}_{k-1}}{\mathbb{G}_{k+1}}+\sum_{i=2}^{k-1}\left(\frac{\mathbb{G}_{k-i}}{\mathbb{G}_{k+1}}\rho^{-i}\prod_{j=1}^{i}\mathbb{R}_{k-j}\right)+\frac{\mathbb{G}_1}{G_{k+1}}\rho^{-(k-1)}\prod_{i=1}^{k}\mathbb{R}_{k-i} \\
&= \sum_{i=1}^{k-1}\left(\frac{\mathbb{G}_{k-i}}{\mathbb{G}_{k+1}}\rho^{-i}\prod_{j=1}^{i}\mathbb{R}_{k-j}\right)+\frac{\mathbb{G}_1}{\mathbb{G}_{k+1}}\rho^{-(k-1)}\prod_{i=1}^{k}\mathbb{R}_{k-i} \\
&= \sum_{i=1}^{k-1}\left(\delta\mathbb{V}_{k-i,k+1}\rho^{-i}\mathbb{Q}_{i,k+1}\right)+\rho^{-(k-1)}\delta\mathbb{V}_{1,k+1}\mathbb{Q}_{k,k+1} \\
&= \mathbb{P}_{k+1}+\rho^{-(k-1)}\delta\mathbb{V}_{1,k+1}\mathbb{Q}_{k,k+1} \\
&\textit{(by the definition of } \mathbb{P}_k \textit{ in Eq. (5.10))}
\end{aligned}
\tag{5.16}
$$

It can be verified by substituting the above Eq. (5.16) back into Eq. (5.15) that formula (5.9) holds at the $(k+1)^{th}$ *step, therefore by induction, holds for any* $k \geq 2$. ■

Corollary 1 *The tracking error at the* k^{th} *iteration is given by*

$$
\begin{aligned}
e_k(j\omega) &= \left(\prod_{i=2}^{k}\mathbb{C}_i(j\omega)\right)e_1(j\omega)+\Lambda_k(j\omega) \\
&\textit{where} \\
\Lambda_k &= \Upsilon_k-\Gamma_k \\
\Upsilon_k &\triangleq \sum_{i=1}^{k}\mathbb{A}_i(j\omega)y_{i,n}(j\omega), \quad \Gamma_k \triangleq \sum_{i=1}^{k-1}\mathbb{B}_i\delta\mathbb{G}_{i+1}u_i
\end{aligned}
\tag{5.17}
$$

with

$$\mathbb{A}_i = \begin{cases} \prod_{j=3}^{k} \mathbb{C}_j, & i = 1, \\ (1 - \mathbb{C}_{i+1}) \prod_{j=i+2}^{k} \mathbb{C}_j, & 2 \le i \le k-2, \\ 1 - \mathbb{C}_{i+1}, & i = k-1, \\ -1 & i = k, \end{cases} \tag{5.18}$$

and

$$\mathbb{B}_i = \begin{cases} \prod_{j=i+2}^{k} \mathbb{C}_j, & 1 \le i \le k-2 \\ -1, & i = k-1. \end{cases} \tag{5.19}$$

The Corollary can be shown by induction and is omitted due to the space limit.

Assumption 3 *In each iteration, at any given frequency ω at which the 1^{st}-order MFDIIC law is applied, we further assume*

$$|\mathbb{R}_k(j\omega)| \le \xi < \frac{\gamma_1^2 \cos\delta\theta}{\gamma_1 + \gamma_2}, 0 \le \angle\mathbb{R}_k < \pi/2, \tag{5.20}$$

Note that the existence of such a ξ in Assumpition 3 is guaranteed by the condition in Eq. (5.6) (see Appendix).

Theorem 1 *At any given frequency where Assumptions 1, 2 and 3 hold, there exists a positive ϵ satisfying*

$$\epsilon < \frac{\gamma_1 \cos\delta\theta(\gamma_2 + \xi - \gamma_1 \cos\delta\theta)}{\gamma_1^2 \cos\delta\theta - (\gamma_1 + \gamma_2)\xi} \tag{5.21}$$

and a positive ρ chosen from

$$\max(\mathbb{X}_1, \mathbb{X}_2) < \rho < \gamma_1 \cos\delta\theta \tag{5.22}$$

where

$$\begin{aligned} \mathbb{X}_1 &= \frac{(\gamma_1 + \gamma_2)\xi}{\gamma_1} \\ \mathbb{X}_2 &= \frac{\gamma_2 + \xi - \epsilon\gamma_1 + \sqrt{(\gamma_2 + \xi - \epsilon\gamma_1)^2 + 4(\gamma_1 + \gamma_2)\xi}}{2} \end{aligned} \tag{5.23}$$

such that

$$|\mathbb{C}_k| \le \epsilon < 1 \tag{5.24}$$

and the iterative law in Eq. (5.8) converges at frequency ω as $k \to \infty$, in the sense that

- *The expectation of the tracking error Λ_k is bounded as,*

$$\lim_{k\to\infty} \mathbf{E}(e_k) = \lim_{k\to\infty} \mathbf{E}(\Lambda_k) \leq \frac{2\sqrt{2/\pi}\sigma_0 + \eta}{1-\epsilon} \tag{5.25}$$

- *The standard deviation of the tracking error is bounded as*

$$\begin{aligned} &\lim_{k\to\infty} \sigma(e_k) = \lim_{k\to\infty} \sigma(\Lambda_k) \\ &\leq \sqrt{\frac{4(1+\epsilon)^2 + 2\pi}{\pi(1-\epsilon)}\sigma_0^2 + \frac{4\sqrt{2/\pi}\sigma_0\eta}{(1-\epsilon)^2} + \frac{\eta^2}{(1-\epsilon)^2}} \end{aligned} \tag{5.26}$$

where σ_0 is the variance of the system output disturbance in Assumption 2.

Proof 2 *We first show that under the given conditions, a positive ρ can be chosen as in Eq. (5.22) that guarantees the stability of the MFDIIC law, i.e., Eq. (5.24) holds. By Eq. 5.10,*

$$\begin{aligned} |\mathbb{C}_k| &= \left|1 - \frac{\rho}{\delta\mathbb{V}_{k-1,k} + \mathbb{P}_k + \delta\mathbb{V}_{1,k}\rho^{-(k-2)}\mathbb{Q}_{k-1,k}}\right| \\ &= \left|\frac{\delta\mathbb{V}_{k-1,k} + \mathbb{P}_k + \delta\mathbb{V}_{1,k}\rho^{-(k-2)}\mathbb{Q}_{k-1,k} - \rho}{\delta\mathbb{V}_{k-1,k} + \mathbb{P}_k + \delta\mathbb{V}_{1,k}\rho^{-(k-2)}\mathbb{Q}_{k-1,k}}\right| \\ &\triangleq \left|\frac{\delta\mathbb{V}_{k-1,k} + \mathbb{F}_k - \rho}{\delta\mathbb{V}_{k-1,k} + \mathbb{F}_k}\right|, \end{aligned} \tag{5.27}$$

where

$$\mathbb{F}_k \triangleq \mathbb{P}_k + \delta\mathbb{V}_{1,k}\rho^{-(k-2)}\mathbb{Q}_{k-1,k} \tag{5.28}$$

By choosing $\rho \in (0, \gamma_1 \cos\delta\theta)$, the numerator in Eq. 5.27 can be bounded as

$$\left|\delta\mathbb{V}_{k-1,k} + \mathbb{F}_k - \rho\right| \leq \left|\delta\mathbb{V}_{k-1,k} - \rho\right| + |\mathbb{F}_k| \leq \gamma_2 - \rho + |\mathbb{F}_k| \tag{5.29}$$

Next we bound $\mathbb{F}_k$. By Assumption 3, we have $\left|\mathbb{Q}_{l,k}\right| = \left|\prod_{i=1}^{l} \mathbb{R}_{k-i-1}\right| \leq \xi^l$. Hence, with $\rho > 0$,

$$\begin{aligned} |\mathbb{F}_k| &= \left|\mathbb{P}_k + \rho^{-(k-2)}\delta\mathbb{V}_{1,k}\mathbb{Q}_{k-1,k}\right| \\ &= \left|\sum_{i=1}^{k-2}\left(\delta\mathbb{V}_{k-i-1,k}\rho^{-i}\mathbb{Q}_{i,k}\right) + \rho^{-(k-2)}\delta\mathbb{V}_{1,k}\mathbb{Q}_{k-1,k}\right| \\ &\leq \left|\sum_{i=1}^{k-2}\left(\delta\mathbb{V}_{k-i-1,k}\rho^{-i}\mathbb{Q}_{i,k}\right)\right| + \left|\rho^{-(k-2)}\delta\mathbb{V}_{1,k}\mathbb{Q}_{k-1,k}\right| \\ &\leq \sum_{i=1}^{k-2}\left|\gamma_2\rho^{-i}\mathbb{Q}_{i,k}\right| + \rho^{-(k-2)}\left|\gamma_2\mathbb{Q}_{k-1,k}\right| \\ &\leq \gamma_2\sum_{i=1}^{k-2}(\rho^{-1}\xi)^i + \gamma_2\rho^{-(k-2)}\xi^{k-1} \\ &\leq \frac{\gamma_2\rho^{-1}\xi[1-(\rho^{-1}\xi)^{k-2}]}{1-\rho^{-1}\xi} + \gamma_2\rho^{-(k-2)}\xi^{k-1} \triangleq \mathbb{M}_k \end{aligned} \tag{5.30}$$

With the choice of ρ in Eq. (5.22) and ξ by Assumption 3, it can be verified that

$$\begin{aligned} \xi < \gamma_2, \quad \textit{and } 0 < \mathbb{M}_2 < \mathbb{M}_3 < \cdots < \mathbb{M}_k, \\ \textit{with } \ \mathbb{M}_\infty = \lim_{k\to\infty} \mathbb{M} = \tfrac{\gamma_2 \rho^{-1}\xi}{1-\rho^{-1}\xi} < \gamma_1. \end{aligned} \tag{5.31}$$

With

$$\left|\delta\mathbb{V}_{k-1,k} + \mathbb{F}_k\right| \geq \left|\left|\delta\mathbb{V}_{k-1,k}\right| - |\mathbb{F}_k|\right| = \left|\delta\mathbb{V}_{k-1,k}\right| - |\mathbb{F}_k| > 0, \tag{5.32}$$

combining Eqs. (5.29) and (5.32) turns Eq. (5.27) to

$$\begin{aligned} |\mathbb{C}_k| &= \left|\tfrac{\delta\mathbb{V}_{k-1,k}+\mathbb{F}_k-\rho}{\delta\mathbb{V}_{k-1,k}+\mathbb{F}_k}\right| \leq \tfrac{\left|\delta\mathbb{V}_{k-1,k}-\rho\right|+|\mathbb{F}_k|}{\left|\delta\mathbb{V}_{k-1,k}\right|-|\mathbb{F}_k|} \\ &\leq \tfrac{\gamma_2-\rho+\mathbb{M}_\infty}{\gamma_1-\mathbb{M}_\infty} = \tfrac{\gamma_2-\rho+\xi}{\gamma_1-(\gamma_1+\gamma_2)\rho^{-1}\xi} \end{aligned} \tag{5.33}$$

Thus, the convergence of the 1^{st}-order MFDIIC is guaranteed, when Eqs. (5.22) and (5.24) hold, which yields the condition for ρ as

$$\rho \geq \frac{\gamma_2 + \xi - \epsilon\gamma_1 + \sqrt{(\gamma_2 + \xi - \epsilon\gamma_1)^2 + 4(\gamma_1 + \gamma_2)\xi}}{2} \tag{5.34}$$

Combining the condition of Eq. (5.22) with the above Eq. (5.34) leads to the choice of ϵ in Eq. (5.21) that guarantees the right side of the above equation is less than $\gamma_1 \cos\delta\theta$, and then the bound of the factor ρ in Eq. (5.22). Thus, with ρ chosen from Eq. (5.21), Corollary 1 implies that

$$\lim_{k\to\infty} e_k(j\omega) = \lim_{k\to\infty} \left[\left(\left(\prod_{i=2}^{k} \mathbb{C}_i(j\omega)\right) e_1(j\omega) + \Lambda_k(j\omega)\right)\right] = \lim_{k\to\infty} \Lambda_k(j\omega) \tag{5.35}$$

Thus, by Eq. (5.17), the expectation of the tracking error is bounded as,

$$\begin{aligned} &\lim_{k\to\infty} \mathbf{E}(e_k) = \lim_{k\to\infty} \mathbf{E}(\Lambda_k) = \lim_{k\to\infty} \mathbf{E}(\Upsilon_k - \Gamma_k) \\ &\leq \lim_{k\to\infty} \mathbf{E}|(\Upsilon_k - \Gamma_k)| \\ &\leq \lim_{k\to\infty} \mathbf{E}|\Upsilon_k| + \lim_{k\to\infty} \mathbf{E}|\Gamma_k| \end{aligned} \tag{5.36}$$

By triangle inequality, we have

$$\lim_{k\to\infty} \mathbf{E}|\Upsilon_k| \leq \frac{2\sqrt{2/\pi}\sigma_0}{1-\epsilon} \tag{5.37}$$

and

$$\begin{aligned} \lim_{k\to\infty} \mathbf{E}|\Gamma_k| &= \lim_{k\to\infty} \mathbf{E}\left\{\sum_{i=1}^{k-2}\left(\prod_{j=i+2}^{k} \mathbb{C}_j\right)\delta\mathbb{G}_{i+1}u_i - \delta\mathbb{G}_k u_{k-1}\right\} \\ &\leq \lim_{k\to\infty} \mathbf{E}\left\{\sum_{i=1}^{k-2}\left|\prod_{j=i+2}^{k} \mathbb{C}_j\right|\left|\delta\mathbb{G}_{i+1}u_i\right| + \left|\delta\mathbb{G}_k u_{k-1}\right|\right\} \\ &= \lim_{k\to\infty} \eta \sum_{i=0}^{k-2} \epsilon^i = \tfrac{\eta}{1-\epsilon}. \end{aligned} \tag{5.38}$$

Addition of the above Eq. (5.38) and Eq. (5.37) leads to the bound given in Eq. (5.25). The variance can be bounded as

$$\begin{aligned}
&\lim_{k\to\infty} \sigma^2(\Lambda_k) = \lim_{k\to\infty} \left\{\mathbf{E}(\Lambda_k^2) - [\mathbf{E}(\Lambda_k)]^2\right\} \\
&\leq \lim_{k\to\infty} \left\{\mathbf{E}(\Lambda_k^2)\right\} \\
&= \lim_{k\to\infty} \mathbf{E}\left\{\Upsilon_k^2 - 2\Upsilon_k\Gamma_k + \Gamma_k^2\right\} \\
&\leq \lim_{k\to\infty} \mathbf{E}\left(\left|\Upsilon_k^2\right| + |2\Upsilon_k\Gamma_k| + \left|\Gamma_k^2\right|\right) \\
&\leq \tfrac{4(1+\epsilon)^2+2\pi}{\pi(1-\epsilon)}\sigma_0^2 + \tfrac{4\sqrt{2/\pi}\sigma_0\eta}{(1-\epsilon)^2} + \tfrac{\eta^2}{(1-\epsilon)^2}
\end{aligned} \tag{5.39}$$

which yields the standard deviation in Eq. (5.26). ■

When only linear dynamics is considered, i.e., when the hysteresis effect becomes negligible (e.g., when the displacement range becomes small [93]), the above convergence can be carried out similarly, and similar results can be obtained. Particularly, in the absence of hysteresis, the same recursive form given in Eqs. (5.9) and (5.10) can be obtained by setting $\delta\mathbb{V}_{i,j}(j\omega) = 1$, $\delta\mathbb{G}_k(j\omega) = 0$ and $\mathscr{H}[u(j\omega)] = u(j\omega)$. Then similar convergence argument can be applied in the presence of random disturbance/noise. The results are summarized below.

Theorem 2 *Let Assumptions1 and 3 hold at any given frequency ω at which the MFDIIC algorithm (5.8) is applied, and let the system input-output be described by the linear time invariant dynamics with an augmented random output disturbance. Then there exists a positive constant ϵ satisfying*

$$\frac{\zeta}{1-2\zeta} \leq \epsilon < 1 \tag{5.40}$$

and a positive iterative gain ρ chosen from

$$\max\left(2\zeta, \frac{1+\zeta-\epsilon+\sqrt{(1+\zeta-\epsilon)^2+8\epsilon\zeta}}{2}\right) \leq \rho < 1 \tag{5.41}$$

such that

$$|C_k| \leq \epsilon < 1, \tag{5.42}$$

and the iterative law in Eq. (5.8) converges at frequency ω as $k \to \infty$, in the sense that

- *The expectation of the tracking error e_k is bounded as,*

$$\lim_{k\to\infty} \mathbf{E}(e_k) \leq \frac{2\sqrt{2/\pi}}{1-\epsilon}\sigma_0 \tag{5.43}$$

- *The standard deviation of the tracking error is bounded as*

$$\lim_{k\to\infty}\sigma(e_k)=\lim_{k\to\infty}\sigma(\Delta_k)\leq\sqrt{\frac{4(1+\epsilon)^2+2\pi}{\pi(1-\epsilon)}}\sigma_0 \tag{5.44}$$

5.2.2 Analysis of the N^{th}-order MFDIIC algorithm for hysteresis-dynamics compensation

Lemma 2 *At the k^{th} ($k\geq 2$) iteration, the tracking error of the k^{th}-order MFDIIC algorithm satisfies the following recursive form,*

$$e_k(j\omega)=\mathbb{C}_k(j\omega)e_{k-1}(j\omega)-\delta n_{y,k-1}(j\omega), \tag{5.45}$$

where

$$\begin{aligned}\mathbb{C}_k(j\omega) &= \sum_{i=1}^{N}\frac{\beta_{k,k-i}}{S_\beta}\mathbb{D}_{k,k-i}(j\omega), N=1,2,3,...,k-1\\ \mathbb{D}_{k,i}(j\omega) &= 1-\mathbb{G}_k(j\omega)\rho\frac{I_{u,i}(j\omega)}{I_{y,i}(j\omega)},\ i=1,2,3,...,k-1\end{aligned} \tag{5.46}$$

and $I_{u,k}(j\omega)$, and $I_{y,k}(j\omega)$ are defined in Eqs. (5.1).

Proof 3

$$\begin{aligned}
&e_k=y_d-\mathbb{G}_k u_k-y_{n,k}\\
&=y_d-\mathbb{G}_k\left[u_{k-1}+\rho\left(\sum_{i=1}^{N}\frac{\beta_{k,i}}{\mathbf{S}_\beta}\frac{I_{u,k-i}}{I_{y,k-i}}\right)e_{k-1}\right]-y_{n,k}\\
&=y_d-\mathbb{G}_k u_{k-1}+\mathbb{G}_{k-1}u_{k-1}-\mathbb{G}_{k-1}u_{k-1}\\
&\quad-\mathbb{G}_k\rho\left(\sum_{i=1}^{N}\frac{\beta_{k,i}}{\mathbf{S}_\beta}\frac{I_{u,k-i}}{I_{y,k-i}}\right)e_{k-1}-y_{k-1,n}+y_{k-1,n}-y_{n,k}\\
&=\left[1-\left(\sum_{i=1}^{N}\frac{\beta_{k,i}}{\mathbf{S}_\beta}\mathbb{G}_k\rho\frac{I_{u,k-i}}{I_{y,k-i}}\right)\right]e_{k-1}-\delta\mathbb{G}_k u_{k-1}-\delta n_{y,k-1}\\
&=\mathbb{C}_k e_{k-1}-\delta\mathbb{G}_k u_{k-1}-\delta n_{y,k-1}
\end{aligned} \tag{5.47}$$

■

Corollary 2 *The tracking error at the k^{th} iteration is given by*

$$\begin{aligned} &e_k(j\omega) = \left(\prod_{i=2}^{k} \mathbb{C}_i(j\omega)\right) e_1(j\omega) + \Xi_k(j\omega), k \geq 2 \\ &\textit{where} \\ &\Xi_k = \Phi_k - \Omega_k \\ &\Phi_k \triangleq \sum_{i=1}^{k} \mathbb{A}_i(j\omega) y_{i,n}(j\omega), \quad \Omega_k \triangleq \sum_{i=1}^{k-1} \mathbb{B}_i \delta\mathbb{G}_{i+1} u_i \end{aligned} \tag{5.48}$$

with

$$\mathbb{A}_i(j\omega) = \begin{cases} \prod_{j=3}^{k} \mathbb{C}_j(j\omega), & i = 1, \\ (1 - \mathbb{C}_{i+1}(j\omega)) \prod_{j=i+2}^{k} \mathbb{C}_j(j\omega), & 2 \leq i \leq k-2, \\ 1 - \mathbb{C}_{i+1}(j\omega), & i = k-1, \\ -1 & i = k, \end{cases} \tag{5.49}$$

and

$$\mathbb{B}_i(j\omega) = \begin{cases} \prod_{j=i+2}^{k} \mathbb{C}_j(j\omega), & 1 \leq i \leq k-2 \\ -1, & i = k-1. \end{cases}$$

The induction-based proof is omitted due to the space limit.

Assumption 4 *In each iteration, at any given frequency ω at which the proposed MFDIIC law is applied, we further assume*

$$\frac{\mathbb{S}_1 - \mathbb{S}_2}{2} < |\mathbb{R}_k(j\omega)| \leq \xi < \frac{\mathbb{S}_1 + \mathbb{S}_2}{2}, \quad 0 \leq \angle\mathbb{R}_k < \pi/2. \tag{5.50}$$

where

$$\begin{aligned} &\mathbb{S}_1 = \gamma_1 + \gamma_2 + 1 \\ &\mathbb{S}_2 = \sqrt{(\gamma_1 + \gamma_2 + 1)^2 - 4(\gamma_1 - \gamma_2 + \gamma_1 \cos\delta\theta)} \end{aligned} \tag{5.51}$$

Note that the condition in Eq. (5.6) allows the existence of ξ in the above Eq. (5.50) (See Appendix).

Next we discuss the stability and convergence of the MFDIIC algorithm in the presence of random disturbance/noise — a zero-mean Gaussian process with the standard deviation as specified in Assumption 2. Note that the following development equally holds for general wide sense stationary process (WSS) as the WSS process can be converted to zero-mean Gaussian process [106].

Theorem 3 *Let Assumptions 1 and 4 hold at any given frequency ω at which the MFDIIC algorithm (5.1) is applied. Then there exists a positive ϵ satisfying*

$$\max\left(\frac{\gamma_2(1+\xi)-\gamma_1\cos\delta\theta}{\gamma_1(1-\xi)}, \frac{\mathbb{T}_1-\sqrt{\mathbb{T}_2}}{2\gamma_1}\right) < \epsilon < \min\left(1-\frac{\xi}{\gamma_1}, \frac{\mathbb{T}_1+\sqrt{\mathbb{T}_2}}{2\gamma_1}\right) \tag{5.52}$$

where

$$\begin{aligned}\mathbb{T}_1 &= \gamma_1+\gamma_2-\xi-\gamma_1\cos\delta\theta \\ \mathbb{T}_2 &= (\gamma_1+\gamma_2-\xi-\gamma_1\cos\delta\theta)^2-4\gamma_1(\xi+\gamma_2-\gamma_1\cos\delta\theta)\end{aligned} \tag{5.53}$$

Note that the existence of ϵ is guaranteed by the range of ξ in Assumption 4. Then a positive ρ can be chosen from

$$max(\mathbb{X}_1,\ \mathbb{X}_2) \le \rho \le \gamma_1\cos\delta\theta \tag{5.54}$$

where

$$\begin{aligned}\mathbb{X}_1 &= \gamma_2(1+\xi)-\epsilon\gamma_1(1-\xi) \\ \mathbb{X}_2 &= \gamma_2-\epsilon\gamma_1+\frac{1+\epsilon}{1-\epsilon}\xi\end{aligned} \tag{5.55}$$

such that

$$\left|\mathbb{D}_{k,i}\right| \le \epsilon < 1, \quad |\mathbb{C}_k| \le \epsilon < 1, \tag{5.56}$$

then the iterative law in Eq. (5.1) converges at frequency ω as $k \to \infty$, in the sense that

- *The expectation of the tracking error e_k is bounded as,*

$$\lim_{k\to\infty}\mathbf{E}(e_k) = \lim_{k\to\infty}\mathbf{E}(\Lambda_k) \le \frac{2\sigma_0\sqrt{2/\pi}+\eta}{1-\epsilon} \tag{5.57}$$

- *The standard deviation of the tracking error is bounded as*

$$\begin{aligned}\lim_{k\to\infty}\sigma(e_k) &= \lim_{k\to\infty}\sigma(\Lambda_k) \\ &\le \sqrt{\frac{4(1+\epsilon)^2+2\pi}{\pi(1-\epsilon)}\sigma_0^2+\frac{4\sqrt{2/\pi}\sigma_0\eta}{(1-\epsilon)^2}+\frac{\eta^2}{(1-\epsilon)^2}}\end{aligned} \tag{5.58}$$

where σ_0 is the variance of the system output disturbance in Assumption 2.

Proof 4 *We first show that under the given condition, a positive ρ can be chosen by Eq. (5.54) that guarantees the stability of the MFDIIC law, i.e., Eq. (5.56) holds. We begin with showing Eq. (5.56) holds by at $i = 1$. Note that*

$$\begin{aligned}
\mathbb{D}_{k,i} &= 1 - \mathbb{G}_k \rho \frac{I_{u,i}}{I_{y,i}} \\
&= 1 - \frac{\mathbb{G}_k \rho I_{u,i}}{\mathbb{G}_i u_i - \mathbb{G}_{i-1} u_{i-1} + y_{n,i} - y_{n,i-1}} \\
&= 1 - \frac{\mathbb{G}_k \rho I_{u,i}}{\mathbb{G}_i u_i - \mathbb{G}_i u_{i-1} + \mathbb{G}_i u_{i-1} - \mathbb{G}_{i-1} u_{i-1} + \delta n_{y,i-1}} \\
&= 1 - \frac{\mathbb{G}_k \rho I_{u,i}}{\mathbb{G}_i I_{u,i} + \delta \mathbb{G}_i u_{i-1} + \delta n_{y,i-1}} \\
&= 1 - \frac{\rho}{\frac{\mathbb{G}_i}{\mathbb{G}_k} + \frac{\delta \mathbb{G}_i u_{i-1} + \delta n_{y,i-1}}{\mathbb{G}_k I_{u,i}}}
\end{aligned} \tag{5.59}$$

Thus, at $i = 1$,

$$\begin{aligned}
\mathbb{D}_{k,1} &= 1 - \frac{\rho}{\frac{\mathbb{G}_1}{\mathbb{G}_k} + \frac{\delta \mathbb{G}_1 u_0 + \delta n_{y,0}}{\mathbb{G}_k I_{u,1}}} \\
&= 1 - \frac{\rho}{\frac{\mathbb{G}_1}{\mathbb{G}_k} + \frac{\mathbb{G}_1}{\mathbb{G}_k} \frac{\delta \mathbb{G}_1 u_0 + \delta n_{y,0}}{\mathbb{G}_1 I_{u,1}}} \\
&= 1 - \frac{\rho}{\delta \mathbb{V}_{1,k} (1 + \frac{\delta \mathbb{G}_1 u_0 + \delta n_{y,0}}{\mathbb{G}_1 I_{u,1}})} \\
&= 1 - \frac{\rho}{\delta \mathbb{V}_{1,k} (1 + \mathbb{R}_0)} \\
&= \frac{\delta \mathbb{V}_{1,k} - \rho + \delta \mathbb{V}_{1,k} \mathbb{R}_0}{\delta \mathbb{V}_{1,k} (1 + \mathbb{R}_0)}
\end{aligned} \tag{5.60}$$

Under the condition of $|\xi| < 1$ and $\rho \leq \gamma_1 \cos \delta\theta$, $|\mathbb{D}_{k,1}|$ can be bounded as

$$\left| \mathbb{D}_{k,1} \right| \leq \frac{\left| \delta \mathbb{V}_{1,k} - \rho \right| + \left| \delta \mathbb{V}_{1,k} \mathbb{R}_0 \right|}{\left| \delta \mathbb{V}_{1,k} \right| |1 - \mathbb{R}_0|} \leq \frac{\gamma_2 - \rho + \gamma_2 \xi}{\gamma_1 (1 - \xi)}. \tag{5.61}$$

$|\mathbb{D}_{k,1}| \leq \epsilon$ is guaranteed by choosing ρ as follows,

$$\rho \geq \gamma_2 (1 + \xi) - \epsilon \gamma_1 (1 - \xi), \tag{5.62}$$

and the choice of ϵ from

$$\epsilon > \frac{\gamma_2 (1 + \xi) - 1}{\gamma_1 (1 - \xi)} \tag{5.63}$$

guarantees the right side of the above Eq. (5.62) to be less than 1. Assumption 4 guarantees the existence of $\epsilon \in (0, 1)$. Hence, under the conditions in Eqs. (5.62) and (5.63), Eq. (5.56) holds at $i = 1$. Then we prove Eq. (5.56) holds by the second principle of mathematical induction.

For $l \geq 2$, assume

$$\left| \mathbb{D}_{k,i} \right| \leq \epsilon, \quad \forall \ 1 \leq i \leq l < k - 1, \tag{5.64}$$

then

$$\begin{aligned}\mathbb{D}_{k,l+1} &= 1 - \mathbb{G}_k\rho\frac{I_{u,l+1}}{I_{y,l+1}} \\ &= 1 - \frac{\rho}{\frac{\mathbb{G}_{l+1}}{\mathbb{G}_k} + \frac{\delta\mathbb{G}_{l+1}u_l + \delta n_{y,l}}{\mathbb{G}_l I_{u,l+1}}} \\ &= 1 - \frac{\rho}{\delta\mathbb{V}_{l+1,k} + \frac{\delta\mathbb{G}_{l+1}u_l + \delta n_{y,l}}{\mathbb{G}_l\rho\left(\sum_{i=1}^{N}\frac{\beta_{l,l-i}}{S_\beta}\frac{I_{u,l-i}}{I_{y,l-i}}\right)e_l}} \\ &= 1 - \frac{\rho}{\delta\mathbb{V}_{l+1,k} + \frac{\mathbb{R}_l}{\mathbb{G}_l\rho\left(\sum_{i=1}^{N}\frac{\beta_{l,l-i}}{S_\beta}\frac{I_{u,l-i}}{I_{y,l-i}}\right)}} \\ &= 1 - \frac{\rho}{\delta\mathbb{V}_{l+1,k} + \frac{\mathbb{R}_l}{\mathbb{F}_l}}, \\ &\textit{with } \mathbb{F}_l \triangleq \mathbb{G}_l\rho\left(\sum_{i=1}^{N}\frac{\beta_{l,l-i}}{S_\beta}\frac{I_{u,l-i}}{I_{y,l-i}}\right)\end{aligned} \tag{5.65}$$

Note that $\sum_{i=1}^{N}\frac{\beta_{l,l-i}}{S_\beta} = 1$. *Under the condition of* $\epsilon < 1$, *the upper bound of* $\mathbb{F}_l$ *is given by*

$$\begin{aligned}|\mathbb{F}_l| &= \left|\mathbb{G}_l\rho\left(\sum_{i=1}^{N}\frac{\beta_{l,l-i}}{S_\beta}\frac{I_{u,l-i}}{I_{y,l-i}}\right)\right| \\ &= \left|1 - \sum_{i=1}^{N}\frac{\beta_{l,l-i}}{S_\beta} + \mathbb{G}_l\rho\left(\sum_{i=1}^{N}\frac{\beta_{l,l-i}}{S_\beta}\frac{I_{u,l-i}}{I_{y,l-i}}\right)\right| \\ &= \left|1 - \sum_{i=1}^{N}\frac{\beta_{l,l-i}}{S_\beta}\left(1 - \mathbb{G}_l\rho\frac{I_{u,l-i}}{I_{y,l-i}}\right)\right| \\ &\leq 1 - \left|\sum_{i=1}^{N}\frac{\beta_{l,l-i}}{S_\beta}\left(1 - \mathbb{G}_k\rho\frac{I_{u,l-i}}{I_{y,l-i}}\right)\right| \\ &\leq 1 - \sum_{i=1}^{N}\frac{\beta_{k,l-i}}{S_\beta}\epsilon \\ &= 1 - \varepsilon,\end{aligned} \tag{5.66}$$

and thereby, $\left|\frac{\mathbb{R}_l}{\mathbb{F}_l}\right| \leq \frac{\xi}{1-\epsilon}$. *Hence, under the conditions that*

$$\rho \leq \gamma_1\cos\delta\theta, \quad \epsilon > 1 - \frac{\xi}{\gamma_1}, \tag{5.67}$$

$|\mathbb{D}_{k,l+1}|$ *can be bounded as*

$$\begin{aligned}\left|\mathbb{D}_{k,l+1}\right| &= \left|\frac{\delta\mathbb{V}_{l+1,k} + \frac{\mathbb{R}_l}{\mathbb{F}_l} - \rho}{\delta\mathbb{V}_{l+1,k} + \frac{\mathbb{R}_l}{\mathbb{F}_l}}\right| \leq \frac{|\delta\mathbb{V}_{l+1,k} - \rho| + \left|\frac{\mathbb{R}_l}{\mathbb{F}_l}\right|}{\left||\delta\mathbb{V}_{l+1,k}| - \left|\frac{\mathbb{R}_l}{\mathbb{F}_l}\right|\right|} \\ &\leq \frac{\gamma_2 - \rho + \frac{\xi}{1-\varepsilon}}{\gamma_1 - \frac{\xi}{1-\varepsilon}} = \frac{(\gamma_2 - \rho)(1-\varepsilon) + \xi}{\gamma_1(1-\varepsilon) - \xi}.\end{aligned} \tag{5.68}$$

$|\mathbb{D}_{k,l+1}| < \epsilon$ *is guaranteed by choosing* ρ *as follows,*

$$\rho \geq \gamma_2 - \epsilon\gamma_1 + \frac{1+\epsilon}{1-\epsilon}\xi, \tag{5.69}$$

and the choice of $\epsilon < 1$ *guarantees the right side of the above Eq. (5.69) to be less than 1. The combination of the Eqs. (5.63) with (5.67) yields the choice of* ϵ *in Eq. (5.52). The combination of Eqs. (5.62) and (5.67) with Eq. (5.69) yields the choice of* ρ *in Eq. (5.54). Therefore,*

$$\left|\mathbb{D}_{k,i}\right| \leq \epsilon, \quad \forall \ 1 \leq i \leq l+1 \leq k-1 \tag{5.70}$$

This completes the proof of Eq. (5.56), with the bound of $\mathbb{C}_k$ *following by using Eq. (5.46), i.e.*

$$|\mathbb{C}_k| = \left|\sum_{i=1}^{N} \frac{\beta_{k,k-i}}{S_\beta}\mathbb{D}_{k-i}\right| \leq \sum_{i=1}^{N} \frac{\beta_{k,k-i}}{S_\beta}|\mathbb{D}_{k-i}| \leq \sum_{i=1}^{N} \frac{\beta_{k,k-i}}{S_\beta}\epsilon = \epsilon \tag{5.71}$$

With the conditions in Eq. (5.56), Theorem 3 can be proved by following the same procedures in the proof of Theorem 1. ■

Similar iteration error and convergence analysis can be applied when only linear time invariant dynamics is considered. Specifically, the same recursive form of the iteration error as in Eq. (2) and (5.45) can be obtained by setting $\gamma_1 = \gamma_2 = 1$ and $\delta\theta = 0$ in Eq. (5.5). Then the similar convergence analysis follows. We summarize the results in the following Theorem.

Theorem 4 *Let Assumptions1 and 4 hold at any given frequency* ω *at which the MFDIIC algorithm (5.8) is applied, and let the system input-output be described by the linear time invariant dynamics with an augmented random output disturbance. Then there exists a positive constant* ϵ *satisfying*

$$\frac{1-\zeta+\sqrt{(1-\zeta)^2-4\zeta}}{2} < \epsilon < 1-\zeta \tag{5.72}$$

and a positive ρ *chosen from*

$$max\left(\frac{(1-\epsilon)(1-\epsilon-\zeta)}{1-\epsilon-2\zeta}, \ 1+\zeta+\epsilon\zeta-\epsilon\right) \leq \rho < 1 \tag{5.73}$$

such that

$$|\mathbb{D}_k| \leq \epsilon < 1, \quad |\mathbb{C}_k| \leq \epsilon < 1 \tag{5.74}$$

and the iterative law in Eq. (5.1) converges at frequency ω *as* $k \to \infty$*, in the sense that*

- *The expectation of the tracking error e_k is bounded as,*

$$\lim_{k\to\infty} \mathbf{E}(e_k) = \frac{2\sqrt{2/\pi}}{1-\epsilon}\sigma_0 \tag{5.75}$$

- *The standard deviation of the tracking error is bounded as*

$$\lim_{k\to\infty} \sigma(e_k) = \lim_{k\to\infty} \sigma(\Psi_k) \leq \sqrt{\frac{4(1+\epsilon)^2 + 2\pi}{\pi(1-\epsilon)}}\sigma_0 \tag{5.76}$$

Proof 5 *It could be proved by setting $\delta V = 1$, and $\delta G = 0$ in the proof of Thm.3.* ■

5.3 Experimental Results and Discussion

In this section, we will present the implementations of the MFDIIC method in output tracking with two different smart actuators: piezoelectric actuator and magnetostrictive actuator, which have symmetric and asymmetric hysteresis behaviors, respectively.

5.3.1 MFDIIC compensation for dynamics effect of LTI systems

System description

The MFDIIC method was implemented to track the motion of the piezoactuator on an AFM system (Dimension Icon, Bruker) as a linear time invariant system. The operation and trajectory tracking issues could be found in [13]. The nominal frequency response (with small excitation voltage amplitude to avoid the hysteresis effect) and hysteresis behavior of the piezoactuator are shown in Fig. 5.2, where the hysteresis loop is measured at the largest stroke (80 μm) of the piezoactuator without any external force exerting on it. A resonance peak is observed around 750 Hz, and the measured peak-to-peak system noise was at the level of 14 mV.

Quantification of the iteration gain coefficient ρ

In order to quantify the iteration gain coefficient ρ, first the parameter ξ needed to be chosen as in Assumption 4, which was chosen to be $\xi = 0.17$ in experiments. Such a choice consequently determined the range of ϵ as in Eq. (5.72), and the value of ϵ was selected to be $\epsilon = 0.7$. With the choices of ξ and ϵ, the coefficient ρ was picked as 0.6 according to Eq. (5.73).

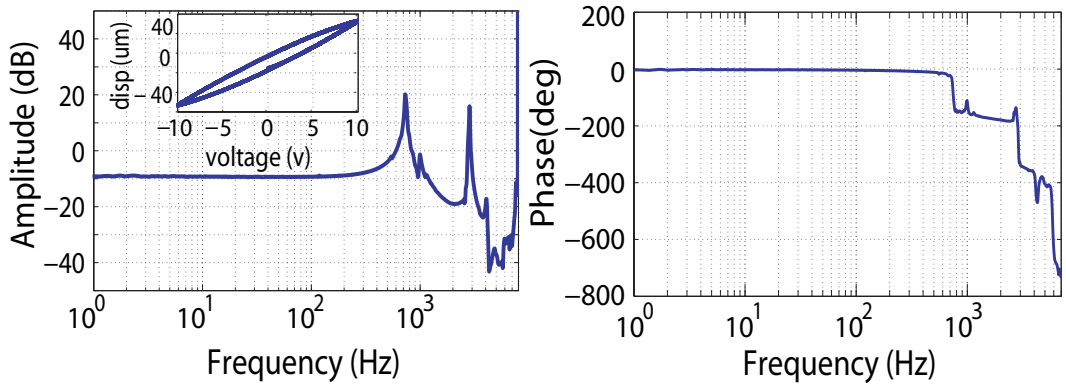

Figure 5.2: The frequency response and the hysteresis behavior of the piezoactuator on the Dimension Icon AFM system.

Trajectory tracking results and discussion

The quantified iteration gain coefficient ρ was used in the 5^{th}-order MFDIIC method to track a band-limited white noise trajectory with cutoff frequency of 1.5 kHz and peak-to-peak amplitude of 10 μm. With such a small peak-to-peak amplitude (1/8 of the full range), the piezoactuation system could be considered as a linear time invariant system as the hysteresis effect of the piezoactuator is negligible. The factors $\beta_{k,k-i}$ in the normalized forgetting factors $\hat{\beta}_{k,i}$ in Eq. 5.1 were chosen to be a power sequence as $\beta_{k,k-i} = r^{k-i-1}$ with $r = 0.2$. Such a selection of the forgetting factors ensured larger weighting on the information in the more recent iterations. Fig. 5.3 (a) shows the tracking results obtained within 18 iterations. The converged tracking of the desired trajectory achieved a relative tracking error of 1.61%. The tracking accuracy is further demonstrated in Fig. 5.3 (b). The tracking error was only at peak-to-peak value around 120 nm (corresponding to 18 mv in voltage), which is close to the measured system noise at 90 nm (corresponding to 14 mv in voltage). Such a precision tracking clearly demonstrated the efficacy of the proposed MFDIIC method in compensating for the dynamics effect of an LTI system such as the piezoactuator on the AFM system.

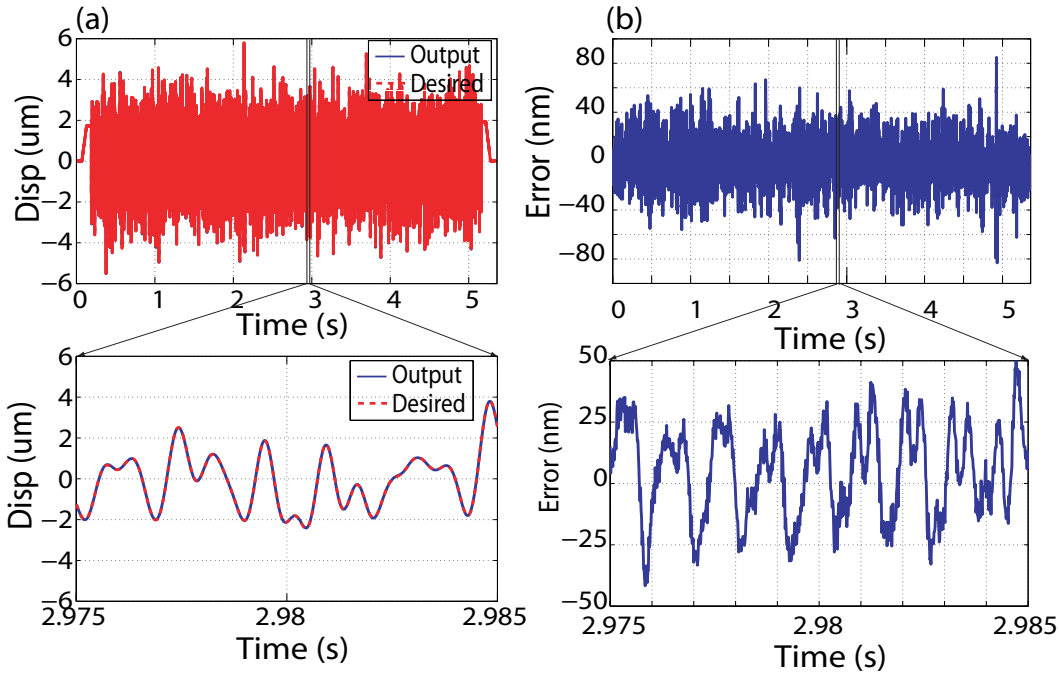

Figure 5.3: Tracking results of white noise with bandwidth of 1.5 kHz and peak-to-peak amplitude of 10 μm: (a) tracking output comparison; (b) tracking error with the piezoactuator on a Bruker Dimension Icon AFM system.

5.3.2 MFDIIC compensation for LTI system dynamics and symmetric hysteresis effect

System description

The same AFM system in the above Sec. 5.3.1 was utilized to verify the capability of the MFDIIC method in compensating for a both nonlinear hysteresis and dynamics of hysteresis-like hammerstein system. From the hysteresis loop in Fig. 5.2, it could be observed that the hysteresis is symmetric, and the hysteresis effect is maximized when the motion range reaches 80 μm, causing the displacement uncertainty (20 μm) accounting for around 25% of the motion range.

Quantification of the iteration gain coefficient ρ

To quantify the coefficient ρ, the variations of the frequency response between any two iterations, $\delta\mathbb{V}_{i,j}(j\omega)$ need to be measured as described in Assumption 1. While the I/O frequency response $\mathbb{G}_k(u, j\omega)$ during the iteration could not be measured beforehand, we could approximate

it by measuring the frequency response corresponding to inputs with various amplitudes, only ten of which are shown in Fig. 5.4. From the measured I/O frequency responses, the boundaries of the magnitude and phase of $\delta\mathbb{V}_{i,j}(j\omega)$ are found to be $\gamma_1 = 0.951$ and $\gamma_2 = 1.073$, $max(\theta) = 6.4°$, and consequently ξ is selected to be $\xi = 0.1$. With the selected boundary parameters, the ranges of ϵ and ρ are subsequently determined as $0.17 < \epsilon < 0.89$ and $0.83 < \rho < 0.97$.

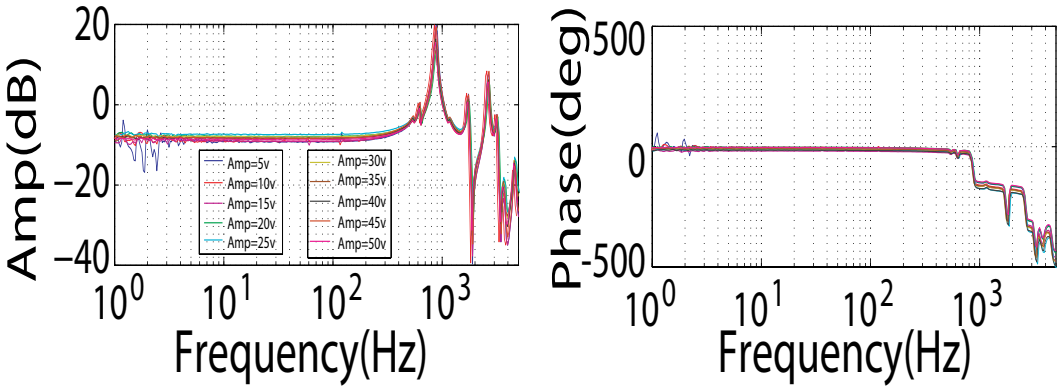

Figure 5.4: I/O frequency response variation of the AFM system.

Trajectory tracking results and discussion

The MFDIIC method was first implemented to track a triangle waveform with frequency of 500 Hz and peak-to-peak amplitude of 80 μm on the same piezoactuation system in the above Section 5.3.1. The tracking result was compared with those obtained by the DC-gain method, IIC method [13] and MIIC [91] method. The tracking results were plotted in Fig. 5.5, and the tracking errors and iteration numbers are listed in Table 5.1, respectively, for comparison. The proposed MFDIIC method attained a relative tracking error of 2.12 %, which is about 6 times less than those obtained by the IIC and MIIC methods (13.64 % and 12.13 %, respectively), and over 70 times less than that by DC-gain method.

Table 5.1: Tracking results by MFDIIC, MIIC, IIC and DC-gain methods

Axis	MFDIIC	MIIC	IIC	DC-gain
Relative RMS Error(%)	2.12	12.13	13.62	152
Iteration Number	18	7	15	1

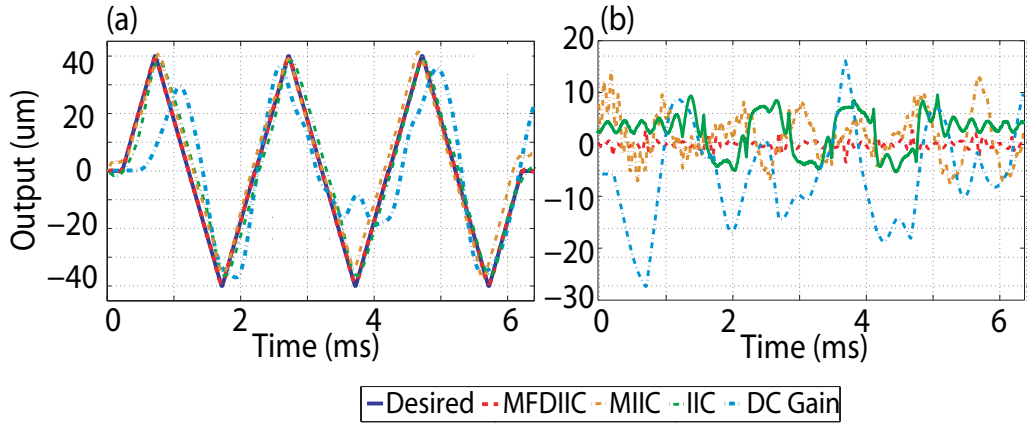

Figure 5.5: Comparison of the triangle waveform (frequency: 500 Hz, peak-to-peak amplitude: 80 μm) tracking results obtained by MFDIIC, MIIC, IIC, and DC-Gain methods on a Bruker Dimension Icon AFM system.

The proposed MFDIIC was also used to track a band-limited white noise trajectory with cutoff frequency of 1.5 kHz and peak-to-peak amplitude of 80 μm. Similarly, the tracking results are plotted in Fig. 5.6, and the tracking errors and iteration numbers are listed in Table 5.2. Note that the tracking by the IIC method couldn't converge, thus is not described in Fig. 5.6 or Table 5.2. Although the iteration number is much larger than the other two methods, the relative RMS error is about 5 times less than that by MIIC method, and over 13 times less than that by the DC-gain method. This further proves the efficacy of the proposed MFDIIC method in compensating both the dynamics effect and symmetric nonlinear hysteresis effect for a hammerstein-like system such as the piezoactuator in an AFM system.

Table 5.2: Tracking results by MFDIIC, MIIC, and DC-gain methods

Axis	MFDIIC	MIIC	DC-gain
Relative RMS Error(%)	3.21	15.89	44.02
Iteration Number	40	12	1

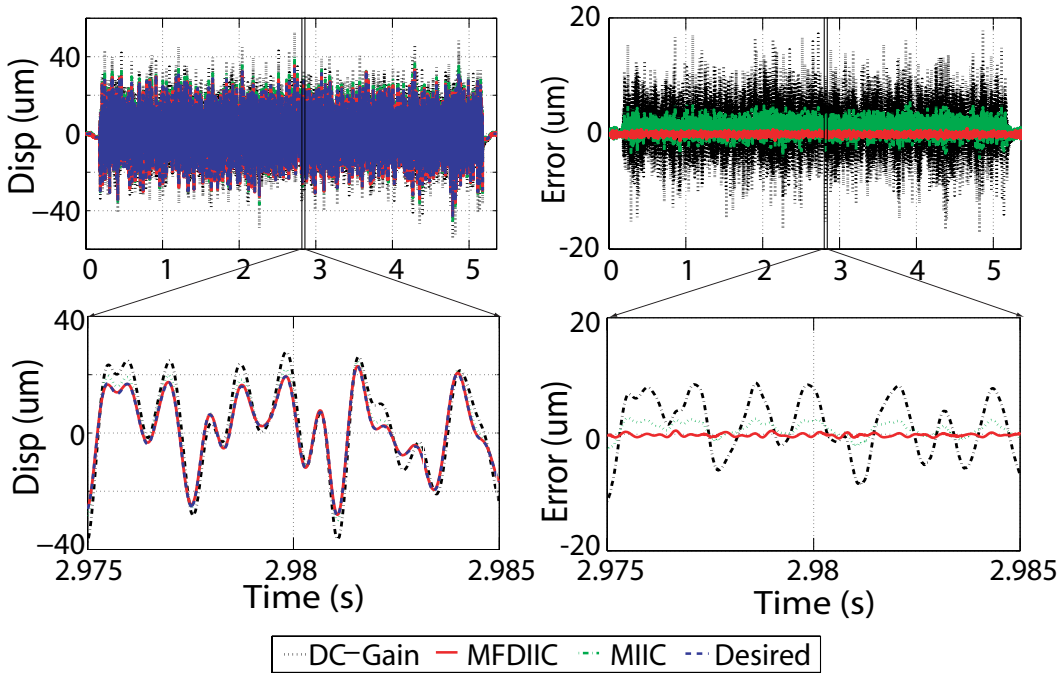

Figure 5.6: Tracking results of the white noise signal with cutoff frequency of 1.5 kHz and peak-to-peak amplitude of 80 μm.

5.3.3 MFDIIC compensation for LTI system dynamics and asymmetric hysteresis effect

System description

In this section, we will implement the proposed MFDIIC method in the trajectory tracking on a magnetostrictive actuator based microforming system [65]. The I/O frequency response and the asymmetric behavior of the hysteresis of the actuation system are shown in Fig. 5.7(a) and (b), respectively. From the frequency response, a very limited bandwidth (7 Hz) is observed, and this would impose huge challenges on conventional PID control methods. Meanwhile note that the overlapping of the hysteresis loops at the origin is caused by the heating effect of the coil in the magnetostrictive actuator.

Quantification of the iteration gain coefficient ρ

Similar to the quantification process in the above Sec. 5.3.2, through preliminary experiment results of the I/O frequency response variation as shown in Fig. 5.8, the boundaries of the magnitude and phase of $\delta\mathbb{V}_{i,j}(j\omega)$ are found to be $\gamma_1 = 0.865$ and $\gamma_2 = 1.279$, $max(\theta) = 35.5°$,

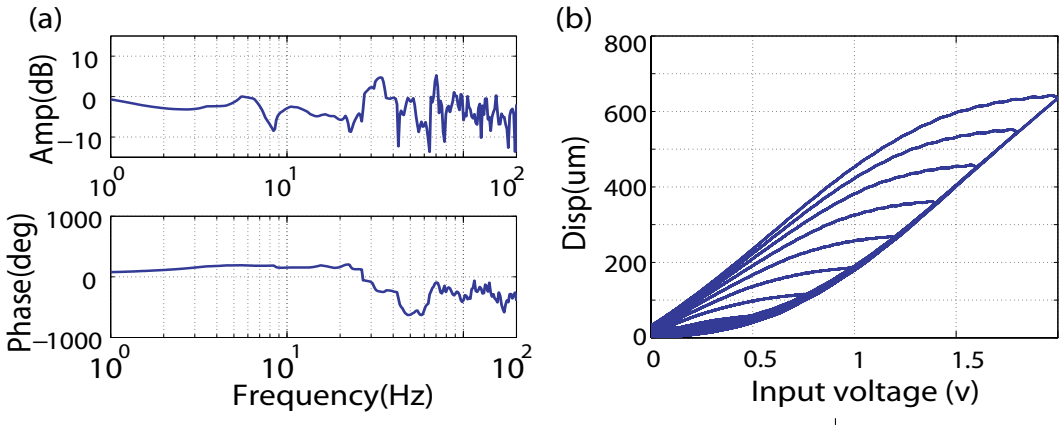

Figure 5.7: Frequency response and the hysteresis effect of the magnetostrictive actuator.

and consequently ξ is selected to be $\xi = 0.01$. With the selected boundary parameters, the ranges of ϵ and ρ are subsequently determined as $0.68 < \epsilon < 0.98$ and $0.67 < \rho < 0.71$. Note that only the frequency response ranging between $1 \sim 40$ Hz was utilized in the quantification of the parameters, as the large oscillations at the high frequency range made the MDFIIC method inapplicable, i.e., ρ doesn't exist for convergence of the MDFIIC method.

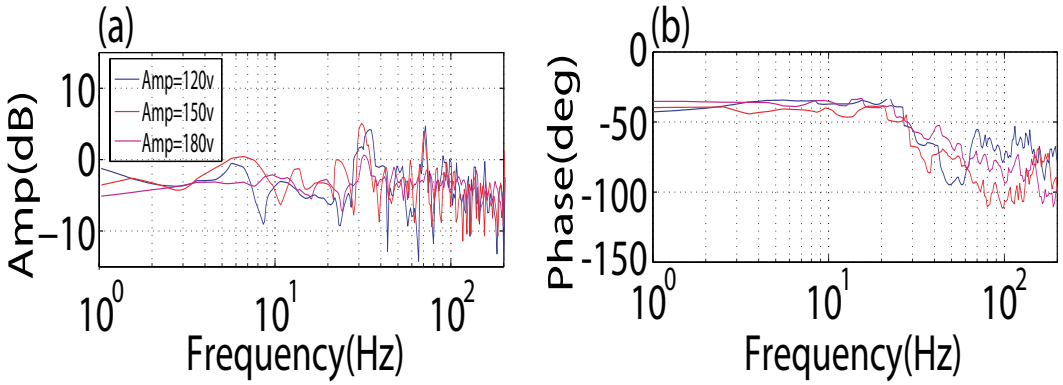

Figure 5.8: I/O frequency response variation of the magnetostrictive actuator.

Trajectory tracking results and discussion

The MFDIIC was first implemented to track a triangle waveform with frequency of 10 Hz and amplitude of 500 μm on the magnetostrictive actuator. The results were compared with that obtained by using the MIIC method in Fig. 5.9. Although iteration number by MFDIIC (11 iterations) is larger than that by MIIC method (5 iterations), significant tracking precision improvement can be observed where the relative RMS tracking error was decreased by over 3

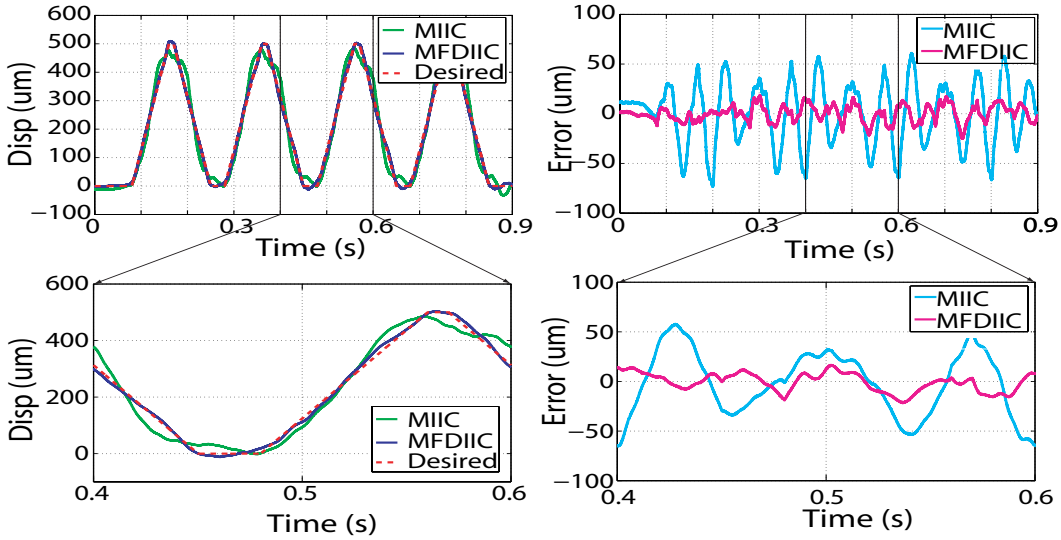

Figure 5.9: Comparison of the tracking results of triangle waveform (frequency: 10 Hz, amplitude: 500 μm) obtained by MFDIIC and MIIC methods obtained with the magnetostrictive actuator.

times (from 11.55% by MIIC to 3.07% by MDFIIC). Similar improvement was also achieved in the tracking of a band-limited white noise trajectory with cutoff frequency of 10 Hz and amplitude of 500 μm, shown in Fig. 5.10. The relative RMS tracking error was also over 3 times smaller than that by the MIIC method (from 17.24% to 5.38%). This demonstrated the capability of the MFDIIC method in compensating for both the dynamics and asymmetric hysteresis effect.

Comparison with other control techniques

To further demonstrate the efficacy of the proposed MFDIIC method, the tracking results of a triangle trajectory on AFM piezoactuators are also compared with other control methods in literature in Fig. 5.11. The control methods are listed in Table 5.3. The x-axis in Fig. 5.11 is the ratio between the triangle trajectory frequency and the resonant frequency of the piezo-actuator used by each method, so the bigger abscissa means the higher capability of the method in compensating for the dynamics effect of the piezo-actuator. The y-axis denotes the ratio between the trajectory amplitude and the full range of the piezo-actuator, and the bigger ordinate means higher capability of the method in compensating for the hysteresis effect of the piezo-actuator. The purpose of the control methods is to achieve the furthest location in the upper right corner in

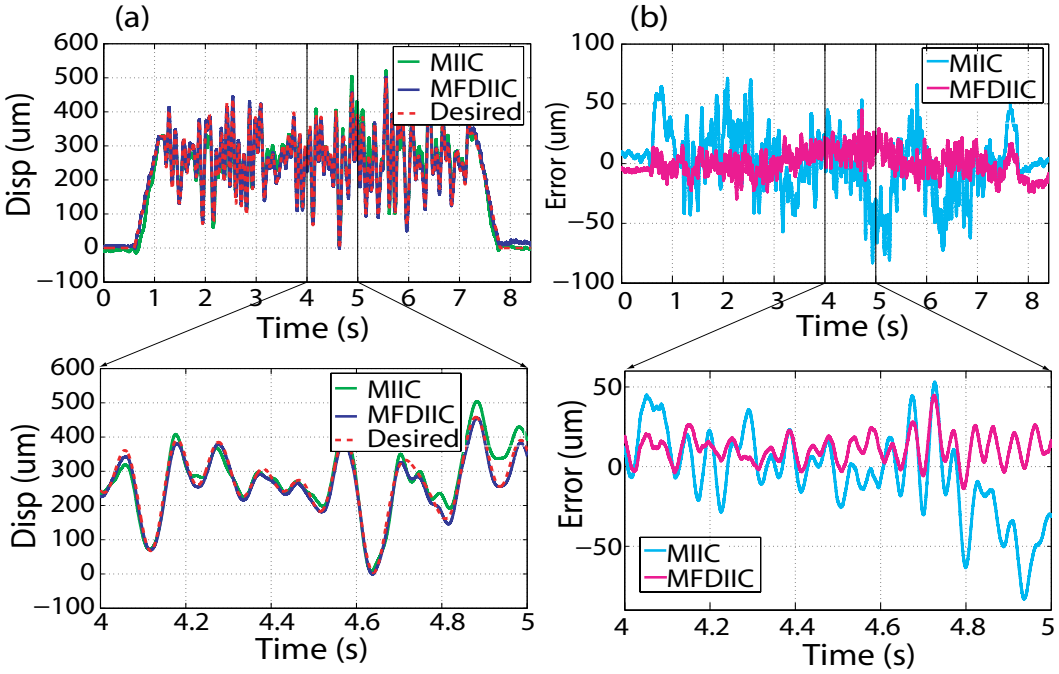

Figure 5.10: Comparison of the tracking results of white noise signal (cutoff frequency: 10 Hz, amplitude: 500 μm) obtained by MFDIIC and MIIC methods obtained on the magnetostrictive actuator.

the figure. Obviously, the proposed MFDIIC not only achieved the largest amplitude/full range ratio, but also realized the highest frequency resonance ratio. This demonstrates the strength of the proposed MFDIIC method in compensating for both the dynamics and hysteresis effect in the smart actuator such as the piezoelectric actuators.

Table 5.3: Control methods compared with the proposed MFDIIC method

$MFDIIC$	Modeling-free Differential-Inversion-Based Iterative Control, proposed	$A_p + FF + FB$	Adaptive Feedforward Feedback [107]
$RobCon$	Robust Control [108]	SMC	Sliding Mode Control [109]
$PI + RC + H^{-1}$	$PIFeedback+RobustControl+H^{-1}$ [110]	$ApCn$	Adaptive Control [111]
$ST + FB$	Signal Transformation Feedback [112]	$InvFB$	Inversion + Feedback [113]

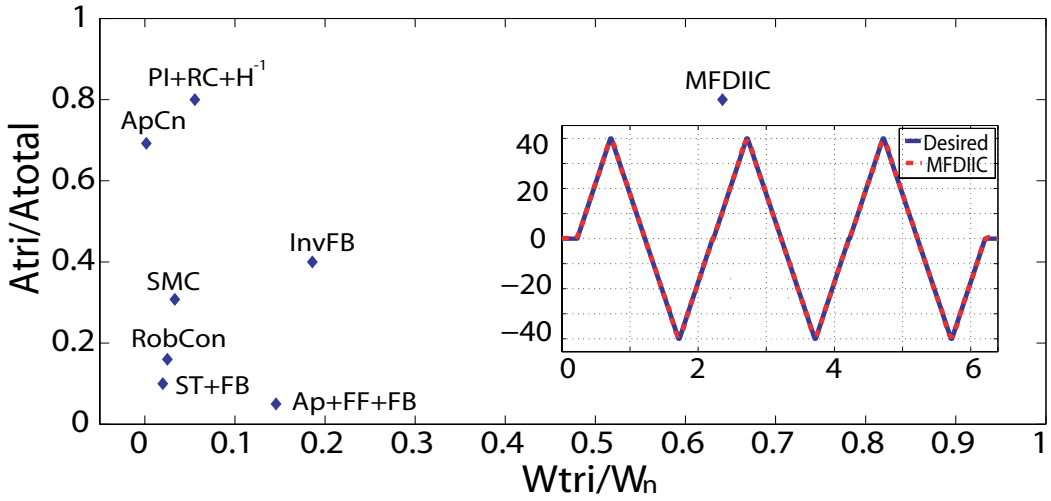

Figure 5.11: Triangle trajectory tracking results compared between the proposed MFDIIC and other control techniques.

5.4 Conclusion

A data-driven modeling-free inversion-base iterative control technique is presented in this chapter. The algorithm is theoretically analyzed for the control of hysteresis-like hammerstein systems by compensating for the system dynamics and hysteresis effect simultaneously. The algorithm could converge with the presence of random output disturbance/noise, and the output tracking error comes close to the noise level in the statistical sense. Finally the proposed control technique was demonstrated in the high-speed large-range output tracking of the piezoactuator in an AFM system and a magnetostrictive actuator in a microforming system.

5.5 Appendix: Existence of $|\mathbb{R}_k|$ in Assumptions 3 and 4

Assumption 5 *We assume the lipschitz continuity is satisfied for the actuator hysteresis, i.e.,*

$$\alpha_1|u_i - u_j| < |y_i - y_j| < \alpha_2|u_i - u_j|, \tag{5.77}$$

Theorem 5 *With the above Assumption 5, there exists a ξ such that*

$$|\mathbb{R}_k| = \left|\frac{\delta\mathbb{G}_{k+1}u_k + \delta n_{y,k}}{e_k}\right| < \xi \tag{5.78}$$

Proof 6

$$
\begin{aligned}
|\mathbb{R}_k| &= \left|\frac{\delta\mathbb{G}_{k+1}u_k+\delta n_{y,k}}{e_k}\right| \\
&= \left|\frac{-\delta\mathbb{G}_{k+1}(u_d-u_k)+\delta\mathbb{G}_{k+1}u_d+\delta n_{y,k}}{e_k}\right| \\
&\leq \frac{|\delta\mathbb{G}_{k+1}|}{\alpha_2} + \left|\frac{\delta\mathbb{G}_{k+1}u_d}{e_k}\right| + \left|\frac{\delta n_{y,k}}{e_k}\right| \\
&= \frac{|\delta\mathbb{G}_{k+1}|}{\alpha_2} + \left|\frac{\delta\mathbb{G}_{k+1}y_d}{\mathbb{G}_d e_k}\right| + \left|\frac{\delta n_{y,k}}{e_k}\right| \\
&= \frac{|\delta\mathbb{G}_{k+1}|}{\alpha_2} + \left|\frac{\delta\mathbb{G}_{k+1}}{\mathbb{G}_d}\right|\left|\frac{y_d}{e_k}\right| + \left|\frac{\delta n_{y,k}}{e_k}\right|
\end{aligned}
\tag{5.79}
$$

The first term in the above Eq. (5.79) depends on the hysteresis property of the controlled actuator, while the third term is determined by the noise level and the tracking error. So as long as the system uncertainty induced by the hysteresis $\delta\mathbb{G}$ is small, and the tracking error is relaxed, these terms are bounded by a small number. Though the second term imposes a condition on the desired tracking trajectory, the value of the entire term could be tuned by the $\delta\mathbb{G}$ and tracking error again. Thus both the property of the hysteresis and desired tracking error imposes the convergence and tracking accuracy of the proposed method. ■

Chapter 6

Conclusion

In this dissertation, the control issues and challenges in advanced manufacturing in micro- and nano-scale are studied, including the complicated system dynamics excited especially at high speeds of the manufacutring system, hysteresis and creep effect of the actuator, and the system variation/uncertainty with environmental disturbances. To address these issues, inversion-based iterative control methods are developed and utilized within a feedforward-feedback control framework to achieve high precision micro- and nano-scale manufacturing. Additionally, ultrasonic vibration is introduced during the manufacturing process to improve the manufacturing quality. The control challenges induced by the integration of the ultrasonic vibration are also solved by the proposed control framework. The main contributions of this dissertation include:

1. A mechatronic system was developed to control the magnetostrictive actuation system for the ultrasonic-vibration-assisted microfroming process. The system dynamics effect of the magnetostrictive actuator was compensated for by the modeling-free inversion-based iteration control algorithm such that a constant ultrasonic vibration amplitude was achieved across a large frequency range. The Fibonacci search method was utilized to achieve rapid identification of the workpiece resonant frequency during the microforming process. This constructs a platform for the research in understanding the fundamental mechanism of ultrasonic vibration effect on microforming process, as well as the development of process control for microforming system. Based on this platform, a dual-stage microforming system was constructed. A control framework for the entire microforming process was designed and implemented to achieve high-speed and high-quality microforming. The modeling-free differential-inversion iterative control method is integrated with the transition trajectory design to achieve rapid engagement of the workpieces without inducing post-engagement oscillations. The Kalman filtering was

employed to detect the phase transition of the workpieces being welded. With the identified phase transition conditions, the optimal transition trajectory was designed based on the optimal output tracking of non-periodic tracking-transition switching. The obtained optimal transition trajectory was then tracked through a feedforward-feedback controller without post-transition oscillations. The experimental control results and welded ABS workpieces demonstrate the efficacy of the proposed approach in achieving optimal high-speed microforming and a substantial improvement of the welding quality.

2. The data-driven, differential-inversion iterative control (MFDIIC) method was integrated with probe ultrasonic vibration to achieve high-speed, large-range nanolithography on hard material via mechanical plowing using an atomic force microscope (AFM). The adverse hardware effects including the hysteresis, the vibrational dynamics and the cross-axis dynamics coupling effects, were compensated for by the proposed MFDIIC method. Normal ultrasonic vibration was introduced to enable direct pattern and improve the pattern quality on hard materials. High-speed lithography and high-quality features were obtained through experiments on tungsten.

3. The data-driven, differential-inversion iterative control (MFDIIC) was proposed to simultaneously compensate for both nonlinear hysteresis and dynamics of hysteresis-like hammerstein systems with good robustness against hysteresis/dynamics changes, while avoiding the arduous hysteresis and vibrational dynamics modeling. The MFDIIC improved over the modeling-free inversion-based iterative control (MFIIC) algorithm by exploring the input-output (tracking) data of not only the last iteration, but also the past iterations to update/correct the control input for the current iteration. Furthermore, the convergence of the MFDIIC in compensating for the hysteresis effect was analyzed by considering the system a hammerstein system in the frequency domain. The output tracking error was quantified in a statistical sense by the properties of the random output disturbance/noise considered in the analysis. The theoretical analysis was also validated through experimental results with two different system setups to demonstrate the competence of the proposed MFDIIC method in compensating for both the system dynamics and hysteresis effect simultaneously.

References

[1] M. Geiger, M. Keliner, R. Eckstein, N. Tiesler, and U. Engel. Microforming. *CIRP Annals - Manufacturing Technology*, 50(2):445–462, 2001.

[2] U. Engel and R. Eckstein. Microforming–from basic research to its realization. *CIRP Annals - Manufacturing Technology*, 125(9):35–44, September 2002.

[3] K.I. Johnson. Microjoining developments for the electronics industry. *CIRP Annals - Manufacturing Technology*, 1(2):5–11, 1983.

[4] Yixu Song, Jianfa Wang, Kaiming Yang, Wensheng Yin, and Yu Zhu. A dual-stage control system for high-speed, ultra-precise linear motion. *The International Journal of Advanced Manufacturing Technology*, 48(5-8):633–643, 2010.

[5] R.B. Evans, J. S. Griesbach, and W.C. Messner. Piezoelectric microactuator for dual stage control. *Magnetics, IEEE Transactions on*, 35(2):977–982, Mar 1999.

[6] Seok-Jun Moon, Chae-Wook Lim, Byung-Hyun Kim, and Youngjin Park. Structural vibration control using linear magnetostrictive actuators. *Journal of Sound and Vibration*, 302(45):875 – 891, 2007.

[7] K. Krishnamoorthy, Chi-Ying Lin, and Tsu-Chin Tsao. Design and control of a dual stage fast tool servo for precision machining. In *Control Applications, 2004. Proceedings of the 2004 IEEE International Conference on*, volume 1, pages 742–747 Vol.1, Sept 2004.

[8] D. Tong, S.C. Veldhuis, and M.A. Elbestawi. Control of a dual stage magnetostrictive actuator and linear motor feed drive system. *The International Journal of Advanced Manufacturing Technology*, 33(3-4):379–388, 2007.

[9] J. Tang W. Dong and Y. ElDeeb. Design of a linear-motion dual-stage actuation system for precision control. *Smart Mater. Struct.*, 18(9), 2009.

[10] I. Lum et al. Effects of superimposed ultrasound on deformation of gold. *Journal of Applied Physics*, 105,024905(2), January 2009.

[11] B Langenecker. Effects of ultrasound on deformation characteristics of metals. *IEEE Transactions on Sonics and Ultrasonics*, 13(1):1–3, March 1966.

[12] O. V. Abramov. *Ultrasound in liquid and solid metals*. CRC Press, Boca Raton, FL, 1994.

[13] Ying Wu and Qingze Zou. Iterative control approach to compensate for both the hysteresis and the dynamics effects of piezo actuators. *Control Systems Technology, IEEE Transactions on*, 15(5):936 –944, sept. 2007.

[14] Erich P. Stoll. Correction of geometrical distortions in scanning tunneling and atomic force microscopes caused by piezo hysteresis and nonlinear feedback. *Review of Scientific Instruments*, 65(9):2864–2869, 1994.

[15] S. Tien, Qingze Zou, and S. Devasia. Iterative control of dynamics-coupling-caused errors in piezoscanners during high-speed afm operation. *Control Systems Technology, IEEE Transactions on*, 13(6):921 – 931, nov. 2005.

[16] Yan Yan, Qingze Zou, and Zhiqun Lin. A control approach to high-speed probe-based nanofabrication. *Nanotechnology*, 20, Apr 2009.

[17] Zhihua Wang, Jun Tan, Qingze Zou, and Wei Jiang. Mechanical-plowing-based high-speed patterning on hard material via advanced-control and ultrasonic probe vibration. *Review of Scientific Instruments*, 84(11):–, 2013.

[18] Erdal Bekiroglu. Ultrasonic motors: Their models, drives, controls and applications. *Journal of Electroceramics*, 20(3):277–286, August 2008.

[19] F.Claeyssen, N.Lhermet, R. Letty, and P.Bouchilloux. Actuators, transducers and motors based on giant magnetostrictive materials. *Journal of Alloys and Compounds*, 258:61–73, August 1997.

[20] Ali Sadighi and Won jong Kim. Adaptive-nuero-fuzzy-based sensorless control of a smart-material actuator. *IEEE/ASME TRANSACTIONS ON MECHATRONICS*, pages 1–9, March 2010.

[21] Won jong Kim and Ali Sadighi. A novel low-power linear magnetostrictive actuator with local three-phase excitation. *IEEE/ASME TRANSACTIONS ON MECHATRONICS*, 15(2):299–307, April 2010.

[22] Zhaohui Ren and Lyndon S Stephens. Closed-loop performance of a six degree-of-freedom precision magnetic actuator. *IEEE/ASME Transactions on Mechatronics*, 10(6):666–674, December 2005.

[23] Laurent Petit et al. A four-discrete-position electromagnetic actuator modeling and experimentation. *IEEE/ASME TRANSACTIONS ON MECHATRONICS*, 15(1):88–96, February 2010.

[24] Si-Lu Chen, Kok Kiong Tan, Sunan Huang, and Chek Sing Teo. Modeling and compensation of ripples and friction in permanent-magnet linear motor using a hysteretic relay. *IEEE/ASME TRANSACTIONS ON MECHATRONICS*, 15(4):586–594, August 2010.

[25] Kyong-Soo Kim and Qingze Zou. A modeling-free inversion-based iterative feedforward control for precision output tracking of linear time-invariant systems. *Mechatronics, IEEE/ASME Transactions on*, 18(6):1767–1777, Dec 2013.

[26] David E. Ferguson. Fibonaccian searching. *Communications of the ACM*, 3:1172–1176, December 1960.

[27] Haiming Wang, Qingze Zou, and Hongbing Xu. Inversion-based optimal output trackingtransition switching with preview for nonminimum-phase linear systems. *Automatica*, 48(7):1364 – 1371, 2012.

[28] Qingze Zou. Optimal preview-based stable-inversion for output tracking of nonminimum-phase linear systems. *Automatica*, 45(1):230 – 237, 2009.

[29] Hector Perez and Santosh Devasia. Optimal output-transitions for linear systems. *Automatica*, 39(2):181 – 192, 2003.

[30] Li Zhang and Jingyan Dong. High-rate tunable ultrasonic force regulated nanomachining lithography with an atomic force microscope. *Nanotechnology*, 23:1–9, Mar 2012.

[31] K. I. Johnson and S. T. Riches. Current and future trends in microjoining. *Welding and Metal Fabrication*, 59:245–250, 1991.

[32] B. Y. Joo, S. I. Oh, and B. H. Jeon. Development of micro punching system. *Microelectronics International*, 50(1):191–194, 2001.

[33] Adam Witthauer, Gap-Yong Kim, LeAnn Faidley, Qingze Zou, and Julie Slaughter. Effect of ultrasonic vibration on micro-extrusion process. *International Conference on MicroManufacturing*, April 2010.

[34] S.J. Liu and et al. Hot embossing precise structure onto plastic plates by ultrasonic vibration. *Polymer Engineering and Science*, 45(7):915–925, May 2005.

[35] H. Storck, W. Littmann, J. Wallaschek, and M. Mracek. The effect of friction reduction in presence of ultrasonic vibrations and its relevance to travelling wave ultrasonic motors. *Ultrasonics*, 40(1-8):379–383, May 2002.

[36] Thomas T. Hansen and Todd Allan Reinders. High power ultrasonic transducer, September 2003.

[37] Etrema Products, Inc. *ULTRASONIC TRANSDUCER CU18A*, 2009.

[38] Alberto Cavallo, Ciro Natale, and Ciro. Visone. Limit cycles in control systems employing smart actuators with hysteresis. *IEEE/ASME TRANSACTIONS ON MECHATRONICS*, 10(2):172–180, April 2005.

[39] Hartmut Janocha, Denis Pesotski, and Klaus Kuhnen. Fpga-based compensator of hysteresis actuator nonlinearities for highly dynamic applications. *IEEE/ASME TRANSACTIONS ON MECHATRONICS*, 13(1):112–116, February 2008.

[40] Dewey J. S., Leang K. K., and Devasia S. Experimental and theoretical results in output-trajectory redesign for flexible structures. *ASME Journal of Dynamic Systems, Measurement and Control*, 120:456–461, December 1998.

[41] Q. Zou and S. Devasia. Preview-based optimal inversion for output tracking: Application to scanning tunneling microscopy. *IEEE Trans. on Control Systems Technology*, 12(15):375–386, May 2004.

[42] Kazuo Kato and Takashi Sase. Robust resonant frequency tracking control for ultrasonic-motor drive. *Electronics and Communications in Japan, Part 2*, 80(3):31–39, January 1997.

[43] S. Furuya, T. Maruhashi, Y. Izuno, and M. Nakaoka. Load adaptive frequency tracking control implementation of two-phase resonant inverter for ultrasonic motor. *IEEE Transactions on Power Electronics*, 7(3):542–550, 1992.

[44] Martin Gutknecht and etc. *Lectures on Numerical Mathematics*. Boston : Birkhauser, Boston, MA, 1990.

[45] Huixia Liu, Zongbao Shen, Xiao Wang, Hejun Wang, and Maoke Tao. Micromould based laser shock embossing of thin metal sheets for {MEMS} applications. *Applied Surface Science*, 256(14):4687 – 4691, 2010.

[46] Desmaris V., Meledin D., Pavolotsky A., Monje R., and Belitsky V. All-metal micromachining for the fabrication of sub-millimetre and thz waveguide components and circuits. *Journal of Micromechanics and Microengineering*, 18(9), Sep 2008.

[47] M. Arentoft, S. Bruschi, A. Ghiotti, N.A. Paldan, and J.V. Holstein. Microforming of lightweight metals in warm conditions. *International Journal of Material Forming*, 1(1):435–438, 2008.

[48] Alexander Rigort, Felix J.B. Buerlein, Andrew Leis, Manuela Gruska, Christian Hoffmann, Tim Laugks, Ulrike Bhm, Matthias Eibauer, Helmut Gnaegi, Wolfgang Baumeister, and Jrgen M. Plitzko. Micromachining tools and correlative approaches for cellular cryo-electron tomography. *Journal of Structural Biology*, 172(2):169 – 179, 2010. Focal Issue on Hybrid Imaging.

[49] P. Piljek, Z. Keran, and M. Math. Micromachiningreview of literature from 1980 to 2010. *Interdisciplinary Description of Complex Systems*, 12(1):1 – 27, 2014.

[50] Yi Qin, A. Brockett, Y. Ma, A. Razali, J. Zhao, C. Harrison, W. Pan, X. Dai, and D. Loziak. Micro-manufacturing: research, technology outcomes and development issues. *The International Journal of Advanced Manufacturing Technology*, 47(9-12):821–837, 2010.

[51] Jun Yanagimoto, Sumio Sugiyama, Akira Yanagida, Nobuhiro Iwamura, and Motoi Ishizuka. Control of ultrafine microstructure by single-pass heavy deformation and cold forging of metal. *Journal of Materials Processing Technology*, 209(2):679 – 685, 2009.

[52] M. Bassu, S. Surdo, L. M. Strambini, and G. Barillaro. Electrochemical micromachining as an enabling technology for advanced silicon microstructuring. *Adv. Funct. Mater.*, 22(6):12221228, Mar 2012.

[53] C.L. Zhang, D.Q. Mei, and Z.C. Chen. Active vibration isolation of a micro-manufacturing platform based on a neural network. *Journal of Materials Processing Technology*, 129(13):634 – 639, 2002. The 10th International Manufacturing Conference in China (IMCC 2002).

[54] X. Chen and W. Li. A monolithic self-sensing precision stage: Design, modeling, calibration, and hysteresis compensation. *Mechatronics, IEEE/ASME Transactions on*, PP(99):1–12, 2014.

[55] A. Sadighi and Won jong Kim. Adaptive-neuro-fuzzy-based sensorless control of a smart-material actuator. *Mechatronics, IEEE/ASME Transactions on*, 16(2):371–379, April 2011.

[56] Toshiyuki Ueno, Hidemitsu Miura, and Sotoshi Yamada. Evaluation of a miniature magnetostrictive actuator using galfenol under tensile stress. *Journal of Physics D: Applied Physics*, 44(6), April 2011.

[57] Xiaobo Tan and John S. Baras. Modeling and control of hysteresis in magnetostrictive actuators. *Automatica*, 40(9):1469 – 1480, 2004.

[58] J. Kongthon and S. Devasia. Iterative control of piezoactuator for evaluating biomimetic, cilia-based micromixing. *Mechatronics, IEEE/ASME Transactions on*, 18(3):944–953, Jun 2013.

[59] L. Gaudiller and F. Matichard. A nonlinear method for improving the active control efficiency of smart structures subjected to rigid body motions. *Mechatronics, IEEE/ASME Transactions on*, 12(5):542–548, Oct 2007.

[60] M. Al Janaideh, S. Rakheja, and Chun-Yi Su. An analytical generalized prandtlishlinskii model inversion for hysteresis compensation in micropositioning control. *Mechatronics, IEEE/ASME Transactions on*, 16(4):734–744, Aug 2011.

[61] A. Cavallo, C. Natale, S. Pirozzi, and C. Visone. Limit cycles in control systems employing smart actuators with hysteresis. *Mechatronics, IEEE/ASME Transactions on*, 10(2):172–180, Apr 2005.

[62] C. Brecher, M. Esser, and S. Witt. Interaction of manufacturing process and machine tool. {*CIRP*} *Annals - Manufacturing Technology*, 58(2):588 – 607, 2009.

[63] H. S. Yoon. *Dynamics of the micro-machining process*. PhD thesis, Northwestern University, Evansto, IL, Jun 2010.

[64] Alejandro Cosimo, Alberto Cardona, and Sergio Idelsohn. Improving the k-compressibility of hyper reduced order models with moving sources: Applications to welding and phase change problems. *Computer Methods in Applied Mechanics and Engineering*, 274(0):237 – 263, 2014.

[65] Adam Witthauer, Gap-Yong Kim, LeAnn Faidley, Qingze Zou, and Zhihua Wang. Design and characterization of a flextensional stage based on terfenol-d actuator. *International Journal of Precision Engineering and Manufacturing*, 15(1):135–141, 2014.

[66] Zhehe Yao, Gap-Yong Kim, Zhihua Wang, LeAnn Faidley, Qingze Zou, Deqing Mei, and Zichen Chen. Acoustic softening and residual hardening in aluminum: Modeling and experiments. *International Journal of Plasticity*, 39(0):75 – 87, 2012.

[67] Zhihua Wang, Qingze Zou, Leann Faidley, and Gap-Yong Kim. Dynamics compensation and rapid resonance identification in ultrasonic-vibration-assisted microforming system using magnetostrictive actuator. *Mechatronics, IEEE/ASME Transactions on*, 16:489–497, Jun 2011.

[68] Zhihua Wang and Qingze Zou. Iterative-control-based high-speed direct mask fabrication via ultrasonic-vibration-assisted mechanical plowing. In *Proc. of ASME Dynamic Systems and Control Conference*, pages 1784–1791, Palo Alto, CA, USA, December 21–23, 2013.

[69] Zhihua Qu and Jian-Xin Xu. Model-based learning controls and their comparisons using lyapunov direct method. *Asian Journal of Control*, 4(1):99–110, 2002.

[70] Jay H. Lee, Kwang S. Lee, and Won C. Kim. Model-based iterative learning control with a quadratic criterion for time-varying linear systems. *Automatica*, 36(5):641 – 657, 2000.

[71] F.L. Lewis and D. Vrabie, editors. *Optimal Control*. John Wiley and Sons, New York, 1995.

[72] William Singhose, Lisa Porter, Michael Kenison, and Eric Kriikku. Effects of hoisting on the input shaping control of gantry cranes. *Control Engineering Practice*, 8(10):1159 – 1165, 2000.

[73] G. A. Terejanu. Discrete kalman filter tutorial. Technical report, University at Buffalo, Buffalo, NY 14260.

[74] A. Isidori, editor. *Nonlinear control systems (3rd ed.)*. Springer-Verlag, London, 1995.

[75] Santosh Devasia. Nonlinear minimum-time control with pre- and post-actuation. *Automatica*, 47(7):1379 – 1387, 2011.

[76] Adam Witthauer, Gap-Yong Kim, LeAnn Faidley, Qingze Zou, and Zhihua Wang. Optimal preview-based stable-inversion for output tracking of nonminimum-phase linear systems. *Polymer Engineering and Science*. Under review.

[77] G. Binnig, M. Despont, U. Drechsler, W. Haberle, M. Lutwyche, P. Vettiger, H.J. Mamin, B.W. Chui, and T.W. Kenny. Ultrahigh-density atomic force microscopy data storage with erase capability. *Applied Physics Letters*, 74(9):1329–1331, 1999.

[78] Richard D. Piner, Jin Zhu, Feng Xu, Seunghun Hong, and Chad A. Mirkin. "Dip-Pen" nanolithography. *Science*, 283(5402):661–663, 1999.

[79] Yu-Ju Chen, Ju-Hung Hsu, and Heh-Nan Lin. Fabrication of metal nanowires by atomic force microscopy nanoscratching and lift-off process. *Nanotechnology, IEEE Transactions on*, 1:39–55, Mar 2002.

[80] K. Yano and T. Ikeda. Stable bit formation in polyimide langmuirblodgett film using an atomic force microscope. *Applied Physics Letters*, 80(6):1067–1069, 2002.

[81] R. Held, T. Heinzel, P. Studerus, K. Ensslin, and M. Holland. Semiconductor quantum point contact fabricated by lithography with an atomic force microscope. *Applied Physics Letters*, 71(18):2689–2691, 1997.

[82] Nele Vandamme, Johan Snauwaert, Ewald Janssens, Erno Vandeweert, Peter Lievens, and Chris Van Haesendonck. Visualization of gold clusters deposited on a dithiol self-assembled monolayer by tapping mode atomic force microscopy. *Surface Science*, 558(13):57 – 64, 2004.

[83] A.J. Fleminga and K.K. Leang. Charge drives for scanning probe microscope positioning stages. *Ultramicroscopy*, 108:15511557, Nov 2008.

[84] Toshio Ando, Noriyuki Kodera, Takayuki Uchihashi, and etc. High-speed atomic force microscopy for capturing dynamic behavior of protein molecules at work. *e-Journal of Surface Science and Nanotechnology*, 3:384–392, Dec 2005.

[85] Andrew J. Fleming. Techniques and considerations for driving piezoelectric actuators at high-speed. In *Modeling, Signal Processing, and Control for Smart Structures*, 2008.

[86] A Notargiacomo, V Foglietti, E Cianci, G Capellini, M Adami, P Faraci, F Evangelisti, and C Nicolini. Atomic force microscopy lithography as a nanodevice development technique. *Nanotechnology*, 10:458–463, Dec 1999.

[87] Muller M., Fiedler T., Groger R., Koch T., Walheim S., Obermair C., and Schimmel T. Controlled structuring of mica surfaces with the tip of an atomic force microscope by mechanically induced local etching. *Surf. Interface Anal.*, 36:189–192, 2004.

[88] Robert Szoszkiewicz, Takashi Okada, Simon C. Jones, Tai-De Li, William P. King, Seth R. Marder, , and Elisa Riedo. High-speed, sub-15 nm feature size thermochemical nanolithography. *NANO LETTERS*, 7(4):1064–1069, 2007.

[89] C. Vieu, F. Carcenac, A. Ppin, Y. Chen, M. Mejias, A. Lebib, L. Manin-Ferlazzo, L. Couraud, and H. Launois. Electron beam lithography: resolution limits and applications. *Applied Surface Science*, 164(14):111 – 117, 2000.

[90] Li Yang and Bechhoefer John. Model-free iterative control of repetitive dynamics for high-speed scanning in atomic force microscopy. *Review of Scientific Instruments*, 80(1):013702–1–013702–5, 2009.

[91] K-.S. Kim and Q. Zou. A modeling-free inversion-based iterative feedforward control for precision output tracking of linear time-invariant systems. *Mechatronics, IEEE/ASME Transactions on*, PP(99):1–11.

[92] Zhonghua Xu, Kyongsoo Kim, Qingze Zou, and Pranav Shrotriya. Broadband measurement of rate-dependent viscoelasticity at nanoscale using scanning probe microscope: Poly(dimethylsiloxane) example. *Applied Physics Letters*, 93(13):133103–133103–3, 2008.

[93] S. Devasia, E. Eleftheriou, and S. O R Moheimani. A survey of control issues in nanopositioning. *Control Systems Technology, IEEE Transactions on*, 15(5):802–823, Sept 2007.

[94] Qingsong Xu and Yangmin Li. Model predictive discrete-time sliding mode control of a nanopositioning piezostage without modeling hysteresis. *Control Systems Technology, IEEE Transactions on*, 20(4):983–994, July 2012.

[95] M. Ruderman, F. Hoffmann, and T. Bertram. Modeling and identification of elastic robot joints with hysteresis and backlash. *Industrial Electronics, IEEE Transactions on*, 56(10):3840–3847, Oct 2009.

[96] Weilin Huang and Walter J. Weber. A distributed reactivity model for sorption by soils and sediments. 10. relationships between desorption, hysteresis, and the chemical characteristics of organic domains. *Environmental Science and Technology*, 31(9):2562–2569, 1997.

[97] Faa-Jeng Lin, Hsin-Jang Shieh, and Po-Kai Huang. Adaptive wavelet neural network control with hysteresis estimation for piezo-positioning mechanism. *Neural Networks, IEEE Transactions on*, 17(2):432–444, March 2006.

[98] Hsin-Jang Shieh, Faa-Jeng Lin, Po-Kai Huang, and Li-Tao Teng. Adaptive displacement control with hysteresis modeling for piezoactuated positioning mechanism. *Industrial Electronics, IEEE Transactions on*, 53(3):905–914, June 2006.

[99] S. Mittal and C.-H. Menq. Hysteresis compensation in electromagnetic actuators through preisach model inversion. *Mechatronics, IEEE/ASME Transactions on*, 5(4):394–409, Dec 2000.

[100] M. Rakotondrabe. Bouc-wen modeling and inverse multiplicative structure to compensate hysteresis nonlinearity in piezoelectric actuators. *Automation Science and Engineering, IEEE Transactions on*, 8(2):428–431, April 2011.

[101] Xiaobo Tan and J.S. Baras. Adaptive identification and control of hysteresis in smart materials. *Automatic Control, IEEE Transactions on*, 50(6):827–839, June 2005.

[102] Kam K. Leang and Santosh Devasia. Design of hysteresis-compensating iterative learning control for piezo-positioners: Application to atomic force microscopes. *Mechatronics*, 16(34):141 – 158, 2006.

[103] Lei Liu, Kok-Kiong Tan, AS. Putra, and Tong-Heng Lee. Compensation of hysteresis in piezoelectric actuator with iterative learning control. In *Advanced Intelligent Mechatronics, 2009. AIM 2009. IEEE/ASME International Conference on*, pages 1300–1305, July 2009.

[104] Qingqing Wang and Chun-Yi Su. Robust adaptive control of a class of nonlinear systems including actuator hysteresis with prandtlishlinskii presentations. *Automatica*, 42(5):859 – 867, 2006.

[105] Po-Jen Ko, Yen-Po Wang, and Szu-Chi Tien. Inverse-feedforward and robust-feedback control for high-speed operation on piezo-stages. *International Journal of Control*, 86(2):197–209, 2013.

[106] Athanasios Papoulis and Unnikrishna Pillai. *Probability, random variables, and stochastic processes*. Tata McGraw-Hill Education, 2002.

[107] J. A. Butterworth, L. Y. Pao, and D. Y. Abramovitch. A discrete-time single-parameter combined feedforward/feedback adaptive-delay algorithm with applications to piezo-based raster tracking. *Control Systems Technology, IEEE Transactions on*, 20(2):416–423, 2012.

[108] X. Chen, T. Hisayama, and C.-Y. Su. Adaptive control for uncertain continuous-time systems using implicit inversion of prandtl-ishlinskii hysteresis representation. *Automatic Control, IEEE Transactions on*, 55(10):2357–2363, 2010.

[109] M. Edardar, X. Tan, and H. K. Khalil. Sliding-mode tracking control of piezo-actuated nanopositioners. In *American Control Conference*, pages 3825–3830, 2012.

[110] T.-Y. Doh, J.-H.Moon, K. Jin, and M. Chung. Robust iterative learning control with current feedback for uncertain linear systems. *Int. J. Syst. Sci.*, 30(1):39–47, 1999.

[111] Y. Li and Q. Xu. Adaptive sliding mode control with perturbation estimation and pid sliding surface for motion tracking of a piezo-driven micromanipulator. *Control Systems Technology, IEEE Transactions on*, 18(4):798–810, 2010.

[112] A. Bazaei, Y. K. Yong, S. R. Moheimani, and A. Sebastian. Tracking of triangular references using signal transformation for control of a novel afm scanner stage. *Control Systems Technology, IEEE Transactions on*, 20(2):453–464, 2012.

[113] W. Ying and Q. Zou. Robust inversion-based 2-dof control design for output tracking: Piezoelectric-actuator example. *Control Systems Technology, IEEE Transactions on*, 17:1069–1082, 2009.